UNIVERSITÉ DE STRASBOURG

ÉCOLE DOCTORALE de Physique et Chimie-Physique (ED 182)

Institut de Physique et de Chimie des Matériaux de Strasbourg

THÈSE présentée par :

MAKARCHUK Stanislaw

soutenue le : 09 décembre 2016

pour obtenir le grade de : **Docteur de l'université de Strasbourg**

Discipline/ Spécialité : Physique

Measurement of cell adhesion forces by holographic microscopy

---

THÈSE dirigée par :

M. Hébraud Pascal   DR, CNRS, Université de Strasbourg

RAPPORTEURS :

M. RIEU Jean Paul   PR, Institut Lumière matière, Lyon

M. FREYSSINGEAS Eric   MCF, Laboratoire de Physique de l'ENS de Lyon

---

AUTRES MEMBRES DU JURY :

M. GAIDDON Christian   DR, CNRS, Université de Strasbourg

M. HEBRAUD Pascal   DR, CNRS, Université de Strasbourg

Table of contents

Résumé

Introduction

La cellule est l'unité élémentaire des organismes vivants avancés. Le but de cette thèse est de développer une technique expérimentale permettant la mesure des forces mécaniques exercées par une cellule sur son environnement. Nous disposons en effet de plus en plus d'observations tendant à montrer qu'il existe une forte interaction entre les processus biologiques de la cellule et l'ensemble des forces qu'elle exerce ou auxquelles elle est soumise. La mesure quantitative des forces exercées par la cellule est ainsi une première étape vers une compréhension de ces interactions.

L'adhésion cellulaire joue un role important dans une assemblée de cellules, formant un tissu. C'est un processus plus complexe que la simple interaction entre deux surfaces. On sait ainsi qu'il existe des points en lesquels la cellule exerce une force importante sur son environnement, qui peuvent être organisés en un réseau organisé.

Il existe plusieurs techniques expérimentales permettant la mesure des forces d'interaction entre une cellule et son substrat, ou l'application de forces à une cellule, afin d'en mesurer les fonctions de réponse mécaniques.

- L'aspiration par micropipette, qui peut être vue comme une façon de modéliser le mouvement d'une cellule dans un vaisseau capillaire [43]. La pression de succion maintient la cellule à l'extrêmité d'une pipette. Puis, la cellule est approchée d'un substrat sur lequel elle adhère, et on mesure la force nécessaire à la détacher.
- l'AFM. Les mesures de forces par AFM permettent de mesurer les propriétés viscoélastiques du cytosquelette [45], et permettent aussi de détacher les cellules de leur substrat. On mesure ainsi des forces adhésives.
- Les techniques d'écoulement : elles consistent à appliquer un écoulement à la surface d'une cellule adhérée, et d'observer sa déformation voire son détachement.

Les techniques ci-dessus permettent de mesurer des forces à l'échelle de la cellule dans son ensemble. La microscopie de force de traction (TFM) permet de mesurer des forces avec une résolution plus petite que la taille de la cellule.

La microscopie de force de traction (TFM)

TFM standard

Le principe de la microscopie de force de traction est la mesure du champ de force exercé par une cellule lors de son adhésion. On dérive ce champ de force de la mesure de la déformation du substrat sur lequel la cellule adhère. Le substrat est en général un gel élastique dans lequel sont dispersées des particules fluorescentes. La mesure du changement de position de ces billes sous l'effet des forces cellulaires permet de déduire le champ de déformation du substrat. On soustrait donc la position des billes dans le substrat en présence d'une cellule de la position en son absence, ce qui constitue l'état de référence mécanique. Connaissant ensuite le module d'Young et le facteur de Poisson du substrat, on peut alors remonter au champ de force cellulaire.Une large gamme de forces est accessible à la microscopie de force de traction, en jouant sur l'élasticité du substrat. De plus, la microscopie de force de traction permet de mesurer les forces exercées par les cellules sur un substrat non plan, par exemple dans le cas de cellules cultivées à l'intérieur du gel. Une mesure de microscopie de traction de force peut être décomposée en quatre étapes [60] :

– la fabrication d'un substrat élastique contenant des particules fluorescentes, et dont la surface libre est recouverte de protéines nécessaires à l'adhésion cellulaire,
– l'obtention de l'image de référence des positions des billes fluorescentes en l'éabsence de force exercée sur le substrat,
– la mesure des positions des billes en présence de la cellule,
– le calcul du champ de forces exercées à la surface du substrat.

Le champ de force obtenu est d'autant plus précis et résolu que la mesure du champ de déformation du substrat est précise et dense.

Cependant, cette technique souffre de deux difficultés. En premier lieu, la résolution de la position de billes fluorescentes selon l'axe z est moins grande que selon les axes x et y. Ensuite, une difficulté est souvent associée à l'utilisation de fluorophores : les expériences longues sont rendues difficiles par le blanchiment des sondes.

Le but de cette thèse est de développer une technique de microscopie de force de traction qui ne soit pas basée sur la microscopie de fluorescence.

La microscopie holographique comme outil de mesure des forces cellulaires

Il est possible de mesurer la position de billes dispersées dans le gel par la mesure du champ de diffracté par une bille lorsqu'elle est éclairée par une onde cohérente (figure 3.1a) : c'est la microscopie holographique. Le champ diffracté a la forme d'une succession de cercles concentriques. Ici, on ne cherche pas à obtenir une image de la bille. Cette technique a été développée par Croquette et Gosse [83] pour la détection de la position de particules dans des expériences de manipulation de molécules uniques. La position de la bille dans le plan xy est obtenue par une technique de corrélation spatiale des images des champs diffractés. Le rayon d'un des maxima d'intensité du champ diffracté dépend de la distance du plan d'observation à celui de la bille : cela permet la détermination de sa position le long de l'axe optique. On utilise pour ce faire une mesure de l'intensité de diffractée par chaque bille à différents plans de côte z diférente(figure 3.1c), que l'on appelel Look-up Table (LUT). La profondeur en z de la LUT dépend des indices optiques de la bille et de la matrice, de la longueur de cohérence de la source, de sa longueur d'onde, de la distance au substrat. Nous mesurons des franges de diffraction à une distance comprise entre 6 et 10 μm sous chaque bille. Le profil radial de l'intensité diffractée par une bille est alors comparé au profil radial de la LUT : cela permet la détermination de la position en z de la bille.

Description du montage

Un schéma du montage expérimental est présenté figure 3.3. L'enceinte (1) permet un contrôle de la température de l'expérience. Par ailleurs, une seconde enceinte, plus petite est posée sur la table du microscope et permet le contrôle du taux de CO_2.

La source (2) est un source spatialement cohérente, mais dont la longueur de cohérence ($l_c \approx 5$ μm) est choisie de telle sorte que les anneaux de diffraction n'excèdent pas quelques micromètres sous chacune des billes. L'échantillon est observé en microscopie par transmission. Les cellules sont cultivées dans une boîte de Petri (3)munie d'une lamelle d'observation microscopique et fixée sur un porte échantillon (4) dont le mouvement est libre sur la table du microscope. (5) Un objectif *ZEISS N-Archoplan* est monté sur un moteur piézoélectrique *PI P-721*, qui bouge parallèlement à la direction de l'axe optique. Ce moteur nous permet d'acquérir une succession d'images à différentes positions en z de chacune des billes. La lumière diffractée est réfléchie par un miroir dichroïque (7) puis collectée par une caméra CCD *BASLER acA1540-25gm*. Un filtre dichroïque permet par
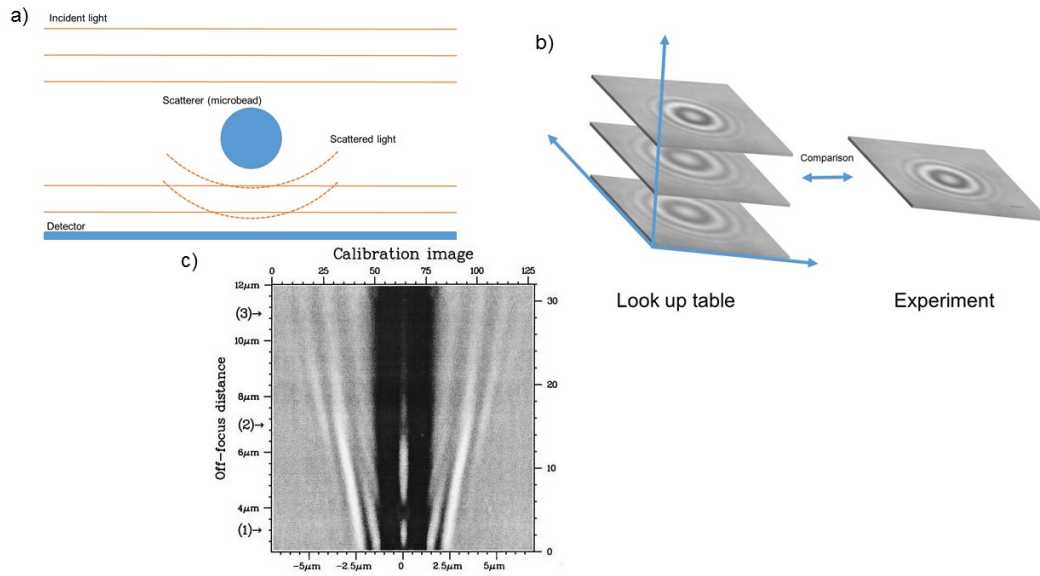
FIGURE 1: **(a)** Schéma de principe de la microscopie holographique. Une onde plane incidente illumine l'échantillon et l'intensité diffractée par les billes est détectée. **(b)** Principe de la mesure de la côte z des billes : une table de correspondance (LUT) est mesurée pour chaque bille et chaque nouvelle figure de diffraction est comparée à cette table afin de déterminer la côte de la bille. **(c)** Exemple de table de correspondance (LUT)
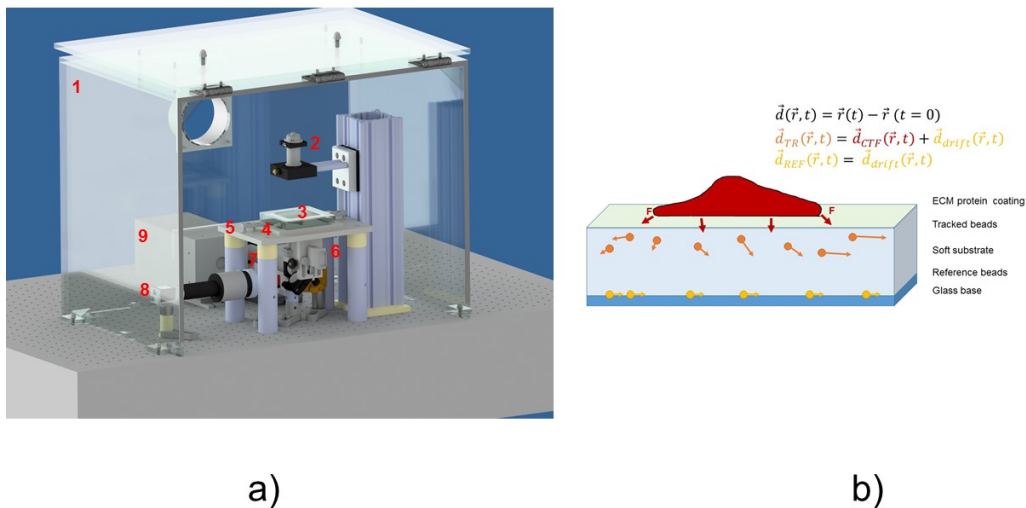
FIGURE 2: Schéma du montage. Les lettres renvoient au corps du texte.

ailleurs d'effectuer de la microscopie de fluorescence des cellules sur leur substrat, dont la source est un LASER solide à 488 nm. Le faisceau LASER est réfléchi sur le miroir (2) puis (1) avant d'entrer collimaté dans l'ouverture arrière de l'objectif de microscope. Ce système permet donc d'obtenir deux types d'images :

- des images en microscopie de transmission, à la fois des anneaux de diffraction des billes sondes dans la matrice gel et des cellules à la surface du gel. Cependant, les structures les moins contrastées des cellules ne peuvent pas être détectées.
- des images d'épifluorescence, utilisées pour imager la cellule. La connaissance précise des frontières des cellules permet de contraindre le calcul du champ de force à partir de la mesure du champ de déformation du gel, et donc permettent une mesure plus précise de ce champ de forces.

Caractérisation du montage

Nous avons déterminé la stabilité et la résolution de notre montage en nous servant de billes de 1 μm de diamètre. Le bruit de la mesure de la position en $x$ et y des billes est 3 nm, alors que selon la direction z, il est égal à 13 nm. Ces valeurs montrent que notre montage permet d'atteindre une résolution supérieure à celles obtenues par microscopie confocale de fluorescence (par exemple 60 [77] ou 120 [1] nm).

Sur des temps longs, (supérieurs à 1 heure, les fluctuations thermiques induisent une dérive du montage. Pour corriger cet effet, nous utilisons des billes de référence, que nous fixons sur la lamelle inférieure du microscope (figure 3.3b). En l'absence de correction, la dérive est de l'ordre de 100 nm en dix heures dans les directions x et y, et de plusieurs microns selon z. Après correction, elle est réduite à 10 nm en x et y et 32 nm selon z.

Enfin, afin de diminuer l'incertitude sur le champ de forces, nous devons déterminer le champ de déplacement avec la densité spatiale la plus grande. Mais la densité de billes utilisable est limitée par l'intersection entre les volumes occupés par les figures de diffraction de chacune des billes. Nous avons ainsi déterminé que la fraction volumique maximale de billes utilisable est 0.1%.

Résultats et perspectives

La détermination du champ de forces appliqué à la surface du gel à partir de la mesure en volume du champ de déformation de ce gel est un problème mathématiquement mal posé : l'erreur sur la valeur obtenue de la force appliquée ne tend pas vers 0 quand l'erreur sur la mesure tend vers 0. Nous utilisons une methode de régularisation, dite de
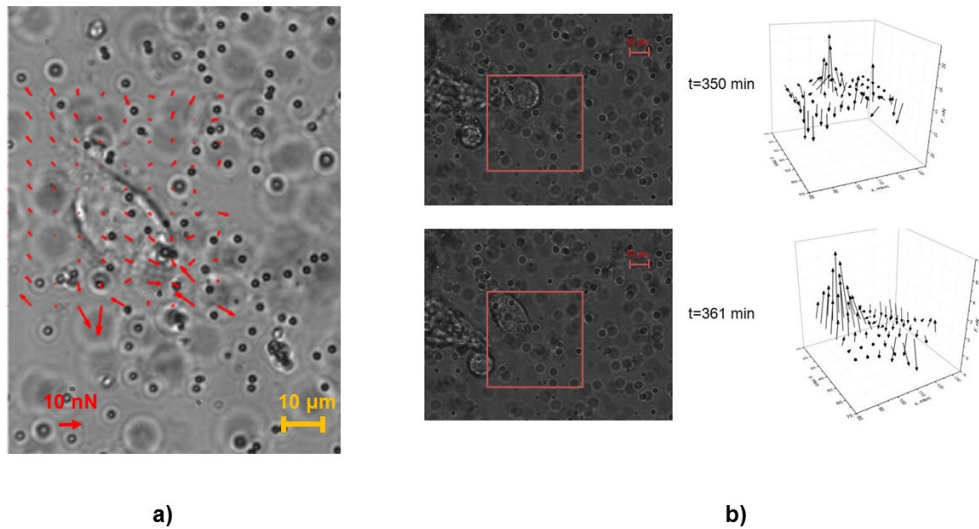
FIGURE 3: **(a)** Image de cellules à la surface d'un gel contenant des particules. **(b)** Champs de force exercés par une cellule sur le gel.

Tikhonov, dans laquelle nous imposons au champ de force calculé une pénalité s'il est trop important [73]. *In fine*, la résolution de notre équipement est 6 μm pour une force minimale égale à 4 nN.

Nous avons étudié l'adhésion de cellules cancéreuses colorectales, SW480, sur un gel de polyamide greffé de collagène. Quelques champs de force sont donnés fig. 3. La figure 3a montre que la cellule adhère sur le substrat à l'aide de deux filopodes, créant un champ de force d'allure dipôlaire. Les forces maximales exercées par la cellule sur le substrat sont égales à 60 nN.

Ce travail ouvre les perspectives suivantes :

– Optimisation de la densité de billes par l'utilisation d'un plan de billes. Afin de limiter le volume interdit aux billes, dû à l'intersection entre les volumes des zones de diffraction, il serait souhaitable de placer toutes les billes dans un même plan. Nous avons commencé à réaliser un tel protocole, en plaçant les billes à la surface du gel.

– Traitement des images de fluorescence. Nous avons monté la microscopie de fluorescence sur notre expérience, mais nous ne nous servons pas des informations sur la localisation précise de la cellule dans le calcul du champ de force à partir du champ de déplacement. Cela permettrait de contraindre la résolution du problème inverse et d'ne améliorer la résolution.

– Optimisation de la méthode de régularisation. Nous avons choisi une méthode de

résularisation dans laquelle nous imposons une pénalité aux champs de force dont la valeur moyenne du module est trop importante. D'autres pénalités (par exemple le gradient de champ) devraient être étudiées afin de déterminer la méthode optimale. Il est aussi possible de réaliser la régularisation dans l'espace de Fourier.

Chapter 1

Introduction

1.1 Generalities

Cells are the basic units of life. They are dynamic, living structures and have mechanical properties, which can be tightly tuned depending on the environment. Many pathological diseases can be directly caused by or catalyzed by irregular cellular or tissue mechanics : (i) mechanical changes in hair bundles (the mechanosensory device of the sensory hair cell) might lead to deafness [1] (ii) a change in cell stiffness mat alter key aspects of metastasis such as invasion [2] and (iii) a sudden rise in high pressure might lead to glaucoma [3]. Therefore, understanding the mechanical properties of the cell can bring insight on relevant cellular processes.

In order to respond to changes in their environment, cells must be able to receive and create signals. Cells can receive different signals simultaneously, and this information will determine cell behaviour afterwards. Cells also send out messages to other cells. At cell - cell junctions, tension from actin and myosin in one cell can be transmitted to a neighboring cell [4]. These interactions determine cell-to-cell adhesion and lead to an exchange of different types of information (e.g. chemical, mechanical and electrical).

Most cell signals are chemical in nature. Both prokaryotic and eukaryotic cells sense chemical gradients through a large number of trans-membrane receptors and are able to move towards (or away form) specific substances. While bacteria need to constantly move to evaluate chemical signals, eukaryotic are larger organisms that can directly feel chemical gradients. In multicellular organisms, growth factors, hormones, neurotransmitters, and extracellular matrix components are some of the many types of chemical signals cells use [5]. These substances can exert their effects locally, or they might travel over long distances. For instance, neurotransmitters are a class of short-range signaling molecules
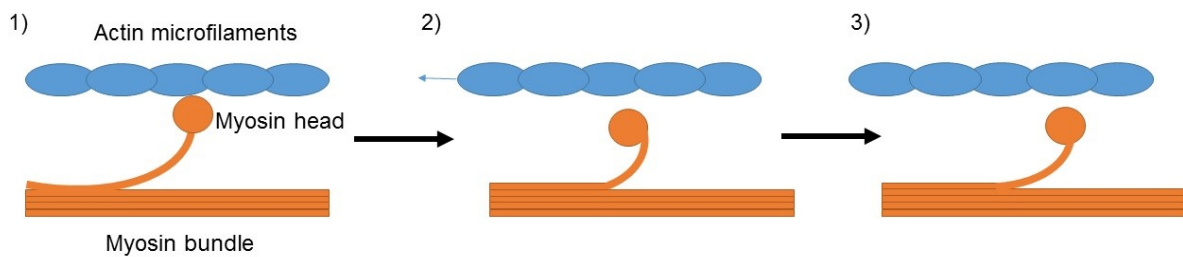
FIGURE 1.1: Force generating structures in muscle cells. 1) Myosin cross bridge attaches to the actin micro-filaments. 2) The myosin head bends and pull actin filaments. 3) Myosin head detaches, and returns in initial position.

that travel across the tiny spaces between adjacent neurons or between neurons and muscle cells. Muscle cells are also good example for a mechanical response of the cell to chemical signal. Thereby, myosin is a molecular motor (which converts chemical energy from ATP hydrolysis into mechanical energy) that moves along actin and causes parallel sliding F-actin components (fig. 1.1).

Some types of cell respond to external mechanical stimuli : skin cells respond to the pressure touch, ear cells react to the movement of sound waves. In addition, specialized cells in the human vascular system detect changes in blood pressure - information that the body uses to maintain a consistent cardiac load [5].

1.2 Cell mechanics

1.2.1 Mechanical properties of the cell

Eukariotyc cells are far more complex than bacteria. We just discuss here the main components of the cell, relevant for cell mechanics (fig. 1.2, right). In a simple picture, cells are composed of three main parts : the cytoplasm, the membrane and the nucleus. The cytoplasm (a gel-like substance) is separated from the outside environment by a membrane, which plays many important roles : transport of ions and organic molecules, cell signaling and cell adhesion. The cell membrane has approximately a thickness of about 10 nm and has a bending stiffness of $10^{-19} - 10^{-20}$ N×m [7]. Note finally that plant cells (like bacteria and fungi) have a rigid cell wall.

Ch. 1. Introduction

Cytoskeleton

The cytoskeleton is found in eukaryotic cells, and consists of a network of filamentous proteins : microtubules, actin filaments and intermediate filaments. Microtubules are polymers with heterodimer subunits and an external radius of about 25 nm [8]. Intermediate filaments are composed of tetramer subunits - protofilaments. They provide strength and integrity organization of the cell. Actin filaments (also called microfilaments, with typical diameters of about 7 to 9 nm) are major stuctural components of the cytoskeleton. Note that actin is present either in a Globular form (G-actin) or in a Filamentous structure (F-actin) and that the concentrations of both forms are tightly regulated. Actin performs a large number of cellular functions : it participates to the generation of cellular forces, contributes to cell adhesion and determines cell shapes [9].

In the cytosol, the mechanical properties of cross-linked actin networks strongly depend on the type of cross-linkers. As these cross-linkers have finite dissociation constants for actin, the equilibrium is dynamic [10]. Still, one usually uses rigid, nondynamic cross-linkers to model the mechanical response of the network. Let us consider here two different types of cross-linkers : (i) filamin A , a dynamic and soft rod-shape polymer, with typical length about 150 nm and (ii) scruin, an actin-binding protein, that is rigid and binds irreversibly to actin. F-actin-scruin (SCR) networks have a well defined elastic plateau, where the elastic modulus is a few orders of magnitude larger than the viscous modulus. In contrast, F-actin networks cross-linked with filamin A (FLNa) have a viscous modulus that is slightly smaller than their elastic modulus (fig. 1.2, left). In contrast to SCR networks (where the elastic modulus can be tuned over several orders of magnitude by varying the concentration of SCR), the linear elastic modulus for FLNa networks is only weakly modified with FLNa concentration (and ranges from 0.1 to 1 kPa). Note finally that the FLNa density has a great influence on the rupture stress of the filament network, this is in contrast with SCR networks for which network breakage is consistent with softer filament rupture.

The main characteristics of the microtubule network is its high bending. In such networks, bending usually occurs on short wavelengths of $\sim$3 μm. In contrast, isolated microtubules exhibit larger wavelengths that are approximately equal to the length of the microtubule. The bending rigidity depends on both the differentiated shear moduli K and linear moduli G : $\lambda \approx (K/G)^{1/4}$. The observed properties (difference in wavelengths) are best explained by an example where a plastic rod is embedded either in a viscous liquid or in soft gelatin. Another important parameter is the critical buckling force for bending : $f \approx \kappa/\lambda^2$, where κ is a bending constant. Thus, microtubules with shorter
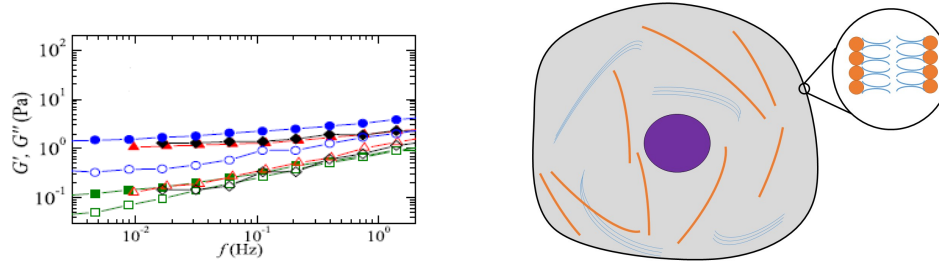
FIGURE 1.2: Left figure : the frequency dependence of storage and loss modulus networks cross-linked with FLNa (adapted from *Gardel et al.* [31]). Right figure : cell structure scheme. Thin blue curves : actin microfilaments , thick : less flexible microtubules. Nucleus (purple) usually situate approximately in the center of the cell. Membrane consists of bilayer of molecules with hydrophilic heads and hydrophobic tails.

bending wavelengths resist to larger compressive forces in the cell.

Intermediate filaments (IF) consists of a large number of different proteins (keratins, vimentin, desmin etc). All IF proteins are organized in filaments with a thickness of approximately 10 nm. The mechanical properties of IF have been less studied than that of actin. Experiments have reported values in the order of 1 μm for the persistence lengths vimentin. This value is one order (three orders) of magnitude smaller than that of F-actin (microtubules [32]). The bending modulus of vimentin is 300 MPa and its Young's modulus 900 MPa [33]. Note finally that measurements on keratin, desmin and neurofilaments are more complicated asthe filaments can be stretched just few times before breaking.

Membrane

The primary role of the cell membrane consists in the cell protection and the control of the diffusion of ions and organic molecules in and out of the cell. The cell membrane is a lipid bilayer with some embedded proteins. This bilayer (or plasma membrane) consists of phospholipids, that are large molecules with hydrophobic and hydrophilic parts. In the plasma cell, phospholipids arrange such that (i) all hydrophilic parts are situated on the two outer surfaces of the bilayer, and (ii) all hydrophobic parts lie inside the plasma. The molecular arrangement of the bilayer is a result of the attraction of the phospholipid head groups (hydrophilic parts) to water and the repulsion of the tail groups (hydrophobic parts). Each phospholipid can freely move inside bilayer, but feels a large resistance when moving in the direction perpendicular to the plasma. Therefore, the plasma membrane behaves as a 2D liquid (as proposed by in 1970 by Singer and Nicolson [34]). This model is called "The fluid mosaic model". In this model, the proteins are sets of molecules arranged in an amphipathic structure (i.e. with hydrophobic and hydrophilic parts). Proteins are

embedded in a matrix of phospholipids, which are modelized as a discontinuous fluid bilayer. Thus a small part of lipids could interact with proteins (or proteins can be trapped in some microdomains inside bilayer). Occasionally, the proteins may obtain energy from thermal fluctuations and pass through the barrier, or escape from the microdomain.

Nucleus

All eukariotyc cells have a nucleus. The main function of the cell nucleus is to maintain the integrity of genes and to control their expression. Still it also plays a role in the mechanical properties of the cell. The nuclear envelope, which is permeable to small molecules, separates the nuclear content from the cytoplasm. It is composed of a double membrane and an underlying nuclear lamina [11]. Experiments have shown that the nucleus is significantly stiffer (1 - 10 kPa [13]) than the surrounding cytoskeleton. *In vivo*, the nucleus of non-adhered cell is spherical or ellipsoidal with a diameter of 5 to 20 μm (a non-spherical geometrical shape of the nucleus could be related to some human diseases [12]). Due to an additional pressure, the shape of the nucleus of adherent cells takes a form like a flat pancake. This pressure arises from the osmotic pressure, the difference between the inner nuclear and cytoplasm pressures and the pressure applied by actin stress fiber and microtubules (mainly from the side, opposite to the surface of adhesion [14]).

Mechanical models for the cells

The cytoskeleton and membrane mainly contribute for the observed mechanical properties. There are about tens popular mechanical models, which are used to describe cell mechanics. All models could be separated in two groups : the nanostructural and the continuous approaches. The continuous approach assumes that cell forms a "continuous" structure. In contrast, the nanostructural approach assumes that the cell is filled with some sub-units (hundreds of nanometers in size) and that these sub-units define its mechanical properties. Here, we will discuss only a few basic models : the Newtonian liquid drop model, the linear viscoelastic model (both are using the continuous approach) and the tensegrity model (nanostructural approach).

Some cells (e.g. leukocytes) behave like a liquid droplet. This behavior is observed experimentally where cells can deform continuously ("flow") inside a micropipette. The Newtonian liquid drop model assumes that the cell interior behaves as a homogeneous Newtonian liquid and that cell membrane consists of an anisotropic viscous fluid (having a constant surface tension and no resistance to bending [40] (see fig. 1.3a). This model qualitatively reports the experimental observations. Both the viscosity of the cell interior
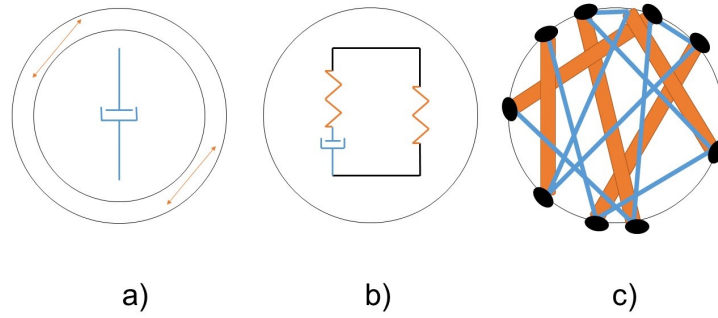
FIGURE 1.3: Models for the cells. a) The Newtonian liquid drop model. The cytoplasm is modeled as a Newtonian liquid (dashpot) and the membrane is modeled as a fluid layer with a constant tension. b) Linear viscoelastic model. The whole cell is represented as a homogeneous linear viscoelastic material. c) Tensegrity model. The architecture results from the interplay between compressive microtubules (orange) and tensile actin (blue) filaments.

$(100-300\,\text{Pa}\times\text{s})$ and the tension of the cell cortex $(0.024-0.03510^{-3}\text{N/m}$ for different cell types) are in agreement with experimental studies [41]. Note, however, that the Newtonian liquid drop model has also significant drawbacks. In particular, this model fails to (i) describe the rapid, initial cell entry into the pipette and (ii) the fact the cell recovers its spherical shape after the pipette is removed (which is a typical signature of the viscoelastic behavior of the cell).

The linear viscoelastic solid model was first proposed in [42] to study the deformations of human leukocytes (pipette aspiration technique). The whole cell is modeled as a homogeneous viscoelastic body, which usually is represented by a dashpot and two springs (fig. 1.3b). From the standart theory of elasticty, the constitutive equation for this system reads :

$$\sigma_{ij} + \frac{\mu}{k_2}\dot{\sigma_{ij}} = k_1\gamma_{ij} + \mu(1 + \frac{k_1}{k_2})\dot{\gamma_{ij}} \tag{1.1}$$

where σ_{ij} and γ_{ij} are components of stress and strain tensors, respectively ; k_1, k_2 are spring elastic constants and μ is the viscous constant (note that the reported experimental values greatly vary depending on the cell types [41]). Today, the linear viscoelastic model is one of the most popular model that can reproduce experimental trends observed in micropipette aspiration, AFM indentation and fluid shear flow (see section "Experimental techniques").

Cells are able to tune their stiffness by changing their shape. The more the cell contracts, the stiffer it becomes ; and the cytoskeleton (bundles of microfilaments and microtubules) plays a main role in cellular contraction. Based on this observations, it has

been proposed [16] that cells use a specific form of architecture known as "tensegrity" : a structure composed of an interconnected network of tensed cables and compressive tubes. Microfilaments would play the role of cables, and microtubules that of the tubes (fig. 1.3c) . This model predicts that contractile cables distribute tensile forces throughout the cytoplasm and nucleus, while compressive forces locate through focal adhesions [17].

These cables are always under tension (even without external forces applied to them, pre-stress). As the stiffness of cytoskeleton element bundles mostly determines the cell stiffness, one can conclude that an higher pre-stress in the cell will cause higher values of the cell stiffness. The tensegrity model is also able to explain another mechanical property of living cells (and some flexible biopolymer networks), which is named stiffening and that occurs when a cell is indented by a sharp object (e.g. AFM tip). Stiffening arises from two mechanisms : (i) the alignment of the stress fibers in the direction of indentation (that raise fibers tension with increasing indentation) and (ii) and increase of cable tension that leads to an increase in stiffness (see above).

Thus, the tensegrity model reports on two important mechanical characteristics of the cells : (i) the increase in cell stiffness with pre-stress of the cytoskeleton bundles and (i) the stiffening of the cell with increasing indentation. Recent AFM measurements (measuring stress fiber stiffness in living cells as a function of strain and pre-stress) are in agreement with the prediction that stiffness increases with pre-stress, and have shown that the stiffening response appears more evident at low pre-stress.

1.2.2   Mechanical stimuli to cells

Many cell types are very sensitive to physical forces. The ability of cells to respond to an external mechanical stimulus is very important for many biological functions such as cell growth, migration, differentiation.

Biomolecular aspects

Cells attach to the Extra Cellular Matrix (ECM) using a large number of different receptors. Under some special conditions, these (matrix) receptor bundle into aggregates, called focal adhesions, and transfer mechanical forces to the cytoskeleton (see section "Cell adhesion"). Integrin (on of the major class of receptors) and cadherin are transmembrane proteins and are therefore good candidates to transmit extracellular forces across the plasma membrane.

In fibrous connective tissues, fibroblasts develop a network of adherens junctions (AJ) between cells. These cadherin-mediated AJs are important for both wound contraction

and intracellular mechano-transduction. The formation and maturation of AJs in response to a mechanical stimulus are yet poorly described.

It has been shown [37] that modifications in the physical properties of the cell membrane (due to external forces) could regulate the conductivity of ion channels. Some experiments also have shown that changes in membrane tensions can enhance the membrane permeability to calcium. In addition, a model proposes that cells regulate ion channel conductivity by force transmission through adhesions to the cytoskeleton (note however, that other processes are also involved). In this model, a force is applied to the cell membrane, which changes membrane tension. This modification results in a change in the ion channel conductance and, potentially, in the expression of certain genes. Some experiments have shown that the trans-membrane calcium ion flux can rapidly vary in response to membrane stretching membrane and support this model [38].

Fluid flow

The body is filled with different types of fluid (e.g. blood, aqueous humour, cerebrospinal fluid). Due to the pressure gradient inside different places of the human body, a flow fluid arises. Usually, endothelial and epithelial cells are under the influence of a constant blood flux. The resulting stress is quite small. Shear stress caused by blood flux in vessels reaches a maximum value of 1 Pa and the Young's modulus of an endothelial cells varies approximately in the range : 100 to 10000 Pa. Therefore, a shear stress of 1 Pa will strain a cell (with an elastic constant of 1000 Pa) only by 0.1%. This results in a cytoskeleton movement of about 100 nm, less than thermal fluctuations. Therefore, most models are based on the observations that the cell surface is not smooth, and that the local stress can be greatly increased by peculiar structures of the cell membrane.

For epithelial and some of endothelial cells, some studies have proposed that primary cilia could act as fluid shear stress mechano-sensors. Primary cilia are cellular protrusions and consist of a ring of parallel oriented microtubules covered by a membrane. The motility of cilia remains unknown : some models consider them as motile structures, while other models propose that they are non-motile protusions. It has been proposed that the mechanism by which cilia sense shear stress is analog to that of actin-based stereocilia (the mechano-sensing organelles of hair cells that can detect sound) [39].

There are at least a few mechanisms by which a cell can amplify forces and so allow it to respond to very small stress. One mechanism relies on the fact that cilia are long structures and that the corresponding lever arm increases the force at the base (fig. 1.4). In blood vessels, long protusions are also able to feel large forces (assuming a laminar flow).
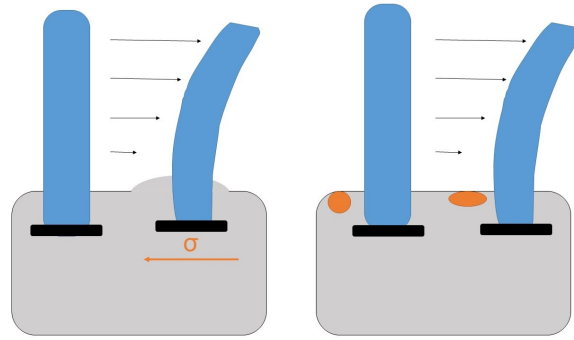
FIGURE 1.4: Schematic diagram of primary cilium and mechanisms by which it may respond to shear stress. Left image represents mechanism with idea that bending of the cilium could amplify force, transmitted to its base. Second mechanism (right image) suggests that an ion channel is stretched due to additional stress on the cilium base.

In turn, the stress created at the ciliary base might be enough to unfold polypeptides and or release specific domain-domain interactions. A second mechanism supposes the existence of ion channels, close to the base of the cilium and located to the side opposite to the flow. When protusions bend, the surface of the cell membrane "behind" the cilia is stretched, and the ion channel then opens (fig. 1.4). In addition, there are other models, which assume a non-motile behavior of the primary cilium.

Cell respond to flow shear stress by several known ways. For Endothelial cells, a flow will affect (i) the cellular morphology (ii) the electrical resistance (a stress around 1 N/m^2 increases the electrical resistance up to 3 kOm [24]) and (iii) gene expression [25]. Note finally that a fluid flow can also regulate organisms during their development (e.g. a fluid flow during the embryonic period regulates left-right asymmetry [8]).

Other examples of mechanotransduction process

To apply twisting forces on cells, the Magnetic Twisting Cytometry (MTC) method has been used [19]. It has been shown that the mechanical stiffness of different types of cells increases linearly with applied shear stress (contractile moment) [26]. Moreover, studies have shown that cell stiffness also varies with the cytoskeletal pre-stress. A change in cell stiffness implies a complete reorganization of the cytoskeleton : microfilaments, microtubules and intermediate filaments.

The development of multicellular organisms would be just impossible without *differentiation*. During cellular differentiation, cells are able to change from one type to an other type. Some cells can differentiate to a define number of cell types (pluripotent or multipotent cells) while some have the potential to differentiate to any cell types (toti-
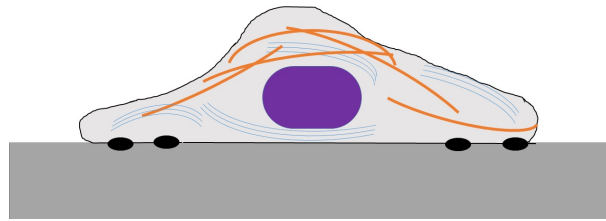
FIGURE 1.5: Cell adhesion onto a soft substrate. Schematic representation of cell adhesion onto a substrate. Cell adhere to a substrate through specific points, focal adhesions (black circles), that are mostly found in cell lamellipodias. The different components of the cytoskeleton and the osmotic pressure create an additional pressure on the core, that leads to a change in shape from spherical to pancake-like [14].

potent cells). External mechanical stimuli also play a key role in cell differentiation. For instance, cells that differentiated in ligament tissues are often under mechanical stress (due to ligament stretching and/or twisting). To model this process *in vitro*, one can use bioreactors, which consist in small capsules in which cells can grow into 3D cell colonies [27]. A mechanical stimulation of bone marrow-derived cells (seeded into collagen gels) induces an elongation of the cells and an alignment of the cells in the direction of the loading. In addition, a stretch of the gel during 21 days of culture causes an increase of the cross-sectional cell density.

1.3 Cell adhesion

Cell adhesion plays an important role in cell assembly into soft tissues of animals. Cell adhesion is a complicated process, which does not just consists in "sticking" the surface of a cell onto a substrate (fig. 1.5). There are special "stick" points organized in highly distinctive patterns. The functional units of cell adhesion are multiprotein complexes, which are composed of three classes of proteins : ECM proteins, cell adhesion molecules receptors and cytoplasmic membrane proteins. Extracellular adhesive complexes are ECM proteins, that are large glycoproteins : collagens, fibronectins, laminins etc. Intracellular complexes are cytoplasmic plaques, which are situated on the inner part of the membrane and are connected to keratin cytoskeletal filaments. Both extracellular and intracellular components create link between the extracellular adhesion system and the cytoskeleton.

Integrin molecules play a key role in cell adhesion. They are dimers, which consist of α and β sub-units (each of which can be present in different isoforms). Integrins have

two main functions : cell attachment and signal transduction from the ECM to the cell (and *vice versa*). As such, integrins give the cell critical informations on its surrounding. In mammals, there are eighteen α and eight β subunits, in Drosophila five α and two β subunits. The different isoforms of dimers allow the extracellular components of integrin molecules to bind to different ECM components (such as collagen or fibronectin). Integrins are tightly bounded to the cell membrane and possess an intracellular part, that is indirectly coupled to the cytoskeleton (through one or few intermediate molecules).

Cahderin molecules are responsible for cell-cell junctions. The cadherin family contains about 20 members (such as E-cadherin N-cadherin etc.), that have a common domain organization. This domain is divided into five repetitive domains, and each subdomain contains calcium-binding sequences. Calcium interactions define the formation of the extracellular binding domain.

The adherens junctions (AJ) are cell-cell junctions, which connect the plasma membranes of two cells. Typically, the space between two cell membranes is around 10-20 nm and filled with rod-shape molecules (cadherins), bridging the membranes. Cadherins associate with cytoplasmic proteins, called catenins, which - in turn - bind cytoskeletal components, such as actin filaments and microtubules [18]. The main functions of AJs are force and signal transductions between neighboring cells through calcium association.

Focal adhesions

Integrins can create discrete adhesive complexes called "focal adhesions". Focal adhesions (FA) are large macromolecular structures, that form a link between the intracellular actin components and multiple extracellular substrates. The main component of FA consits in integrin molecules, but FA can contain over 100 different proteins, which suggests a wide functional diversity. FA are constantly binding their substrate and dissociating from their substrate. This process acts as a signal, which is transmitted to other parts of the cell and triggers different responses (e.g. cell adhesion, cell motion). Integrins, that integrate through FA into the extracellular matrix, may function as mechanoreceptors that provide a preferred path for the transfer of a mechanical force across the cell surface [19].

In cells permanently attached to a substrate, FA are quite stable. In contrast, FA are constantly assembling and disassembling in moving cells as the cell creates new adhesion points at the leading edge and breaks old contacts at the tailing edge.

During cell migration, both the composition and the morphology of the FA change. Small focal adhesions (25 μm^2) are formed at the leading edge of the cell in lamellipodia.
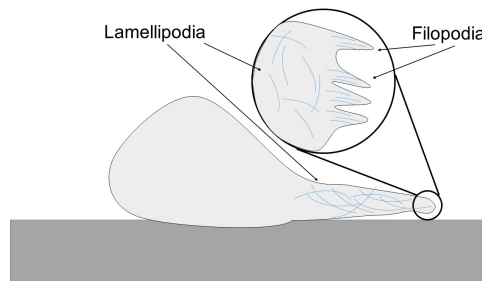
FIGURE 1.6: Filopodia and lamellipodia. Filopodia are tiny protrusions on the lamellipodia. Actin fibers are found in filopodia organized parallel to each other. Tis contrasts the random microfilaments distribution found in lamellipodia.

These structures consist of integrin and some adapter proteins, such as talin, paxillin and tensin. Many of these FA disassemble when the lamellipodia retracts. However, some FA mature into larger and stable focal adhesions, and recruit many more proteins. When FA remain stationary with respect to the extracellular matrix, the cell uses this as an anchor point on which it can push or pull itself over the ECM. During cell motion the focal adhesion at the tailing edge of the cell must be destroyed. This mechanism, and the regulation of the number of FA, are still poorly understood.

Filopodia and lamellipodia

Filopodia is a thin actin plasma protrusion that serves as "antenna" for cells to discover environment. There are two protrusive structures at the leading edge : filopodia and lamellipodia (figure 1.6). Lamellipodia is a thin protrusion, filled with branched actin networks. In contrast, filopodia is a thin, finger-like structure, that is filled with parallel bundles of F-actin. It is often found embedded in the lamellipodial actin network [35]. Filopodia are highly dynamic structures. Inititation, elongation and retraction of filopodia depend on both the actin polymerization and the etrograde flow of the actin filament bundles. This coordinated polymerization of actin components has also implications for other processes : cell migration, morphogenesis, cytosis and phagocytosis. Recent studies show that filopodia could act also as a cellular tentacle : after binding to some objects, filopodia could retract and pull this object.

1.4 Experimental techniques

There are a large number of experimental techniques, which allow to measure (i) rupture forces (ii) the viscoelastic properties of the cells and (iii) the response cells to a

mechanical stimulus. In this section, we highlight some of them.

Micropipette aspiration

In a typical micropipette aspiration experiment, a suction pressure is applied with a micropipette (fig. 1.7a) . This allows to study the movement of cells into small vessels or determine adhesion forces between a cell and its substrate. This technique can successfully measure the viscous properties of both soft and stiff cells (e.g. endothelial cells, chondrocytes) and can detect forces in the range of 10^{-2} to 10^4 nN (corresponding to pressure values from 0.1 pN/μm^2 to almost atmospheric pressure) [43]. Continuous models (liquid drop, Newtonian liquid drop, Maxwell liquid drop linear viscoelastic) are usually used for the interpretation of micropipette aspiration experiments. Note finally that this technique has some drawbacks : a slow drift in the estimation of the null (zero) pressure (usually due to evaporation) limits the detectable pressure.

AFM

In biology, two operation modes of Atomic Force Microscopy (AFM) are preferred (fig. 1.7b). Contact mode is a standard operation mode of AFM in which the tip of the cantilever is dragged across the surface. This allows to rapidly study the cell surface morphology. To prevent scratches on the surface, a positive feedback loop is used which maintains a constant deflection of the cantilever (constant loading force). Still, the tip might stretch the surface or remove some poorly attached cell components. In cell mechanics, a special mode of AFM - the so-called "Force mode" - is also used. Here, the cantilever remains at a fixed (lateral) position above the cell surface. Force-distance curves are then recorded (the tip is approached towards the sample, contacts the cell surface and then is retracted). Such traces provide information on the visco-elastic properties of the cell as well as the adhesion forces between the tip and the cell surface. Note that this mode of operation requires extremely clean tips to prevent non-specific interactions. In addition, a large amount of data have to be recorded as the cell surface is typically non-homogeneous. Notice that standard AFM tips are usually too sharp for a cell as they can easily penetrate the cell surface [1]. Hence, large dull tips are preferred (for instance by attaching a silica micro-bead to the cantilever). Finally, AFM cantilevers can be also used to detach individual cells (by applying a tangential force, which can be precisely adjusted).

Like all other techniques, AFM has some drawbacks : (i) because of the non-zero

---

1. Some experiments require the use of sharp tips , which allow to penetrate inside the cell (a force in the order of a few nanonewtons allows penetration depth up to 500 nm [44].
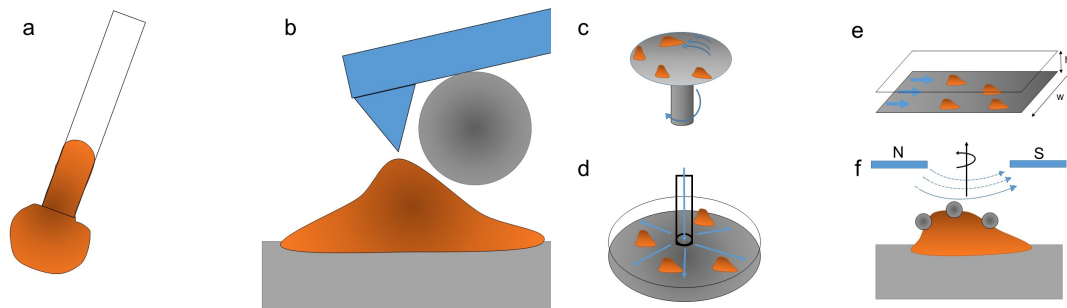
FIGURE 1.7: Schematic representation of experimental techniques to measure the mechanical properties of the cell. (a) Micropipette aspiration. (b) AFM technique allows to apply forces to cell plasma without breaking the membrane (using a microbead instead of pyramide shape tip). (c) Spinning disk method : the shear stress increases linearly with the radial position of the cell on the disk. (d) Radial flow chamber : the shear stress decreases with increasing the radial distance. (e) Parallel plate flow chamber. (f) Magnetic twisting cytometry : magnetic beads functionalized with ligands are attached to a cell through specific receptors at the cell membrane. The displacement of the bead deforms a portion of the cell and a rotation of the magnetic field twists the cell.

vertical speed of the cantilever, there is an error in the determination of the static Young's modulus, (ii) simple models consider that the interaction takes place between a probe and a flat surface (which is not the case for a cell) and (iii) large adhesion forces may influence the motion of the cantilever. Still, AFM remains one of the most sensitive and precise tools to detect forces and estimate viscoelastic properties.

Flow methods

The adhesion of cells on substrates can be studied using shear flow assays.

In the spinning disk method, cells are deposited on specific substrates, which are then fixed onto a disk that is rotated at high speed (500 to 300 RPM) (fig. 1.7c). Depending on their radial position, cells experience different shear stress (values up to 200 Pa can be reached [46] so that it is possible to detach cells which bind strongly to their substrate).

In a Radial flow cell, a flow impinges on the center of the cell (composed of two parallel disks) and exits radially outwards (fig. 1.7d). The cells are seeded on a disk and therefore remain stationary (in contrast, the motion of the spinning disk could bias the measurements). In this method, typical Reynolds number are about 2000 and the maximum shear stress that can be generated is less than 20 Pa. Therefore, the method is best suited for cells that are weakly bound to their substrate.

Parallel plate flow chambers use rectangular plates instead of disks. For $h \ll w$ (fig. 1.7e), the shear stress is constant along the length and highly uniform across the width

of the chamber. For a channel of 100 μm in height, the Reynolds number is about 2300, yielding a shear stress less than 30 Pa. Lu et al. [48] successfully reached higher values (640 Pa) using channel of 25 μm in height.

Magnetic twisting cytometry

Magnetic twisting cytometry (MTC) uses ferromagnetic microbeads (1 to 10 μm in diameter) to apply twisting forces to the cell membrane. Ferromagnetic beads are decorated with specific ligands that can bind specific receptors on the cell membrane (fig. 1.7f) . The beads are magnetized along certain directions using a brief a magnetic pulse (e.g. 100 mT for 1 ms). This technique can be used to obtain viscoelastic properties of the cell and has successfully demonstrated, that forces, applied to different receptors, may produce different types of responses. In addition, MTC can probe trans-membrane mechanical coupling to the cytoskeleton.

1.5   Cell mechanics of cancer cells

Understanding the transition from non-cancerous to metastatic cell lines and determining the difference between them remain a major challenge in cancer research. In this section, we focus on a series of experiments (published in [48]) performed on the non-tumorigenic MCF-10A and metastatic MDA-MB-231 breast epithelial cell lines. Experiments were performed in different laboratories using different bio-physical techniques.

Cell migration at 1-, 2- and 3-dimensions

One of the hallmarks of cancer cells is their high motility in multiple microenvironments and their capability to penetrate through vascular walls. Cell motion was observed in 1D, 2D and 3D environments (fig. 1.8a). In a 1D environment, cells have been constrained in narrow channels (13 μm width), where they can move only forward or backward. MCF-10A cells traveled more than three times faster than metastatic ones. However, MDA-MB-231 cells traveled farther than non-cancerous cells along 1D channel.

2D cell motion was investigated using glass surfaces coated with collagen. MCF-10A cells moved in a circular pattern, so that the leading edge swung while the lagging edge remained almost at the same location. In contrast, MDA-MB-231 cells moved more linearly and slowly. Also, the maximal invasion distance was found to be smaller for MDA-MB-231 cells .

In a 3D collagen matrix, MCF-10A cells also moved in a circular way, but MDA-MB-231 traveled farther. The speed of motions was roughly identical for cell lines.

These results show that the cell motility strongly depends on the dimensionality of the environment. In summary, non-tumorigenic cells move faster than metastatic cells, but remained within a limited circular area (whereas the mobility of MDA-MB-231 cells is linear and are those cells are able to move farther away).

Adhesive properties

The role of two ECM components in cell adhesion process was studied. These components were : laminin (a primary ECM component of the basement membrane in breast tissue) and hyaluronic acid (HA, an anionic non-sulfated glycosaminoglycan spatially distributed in the ECM). Traction force microscopy (see below) was used to measure the forces exerted by a single cell adhered on a substrate. These experiments were performed at different laminin concentrations : 0.1, 10 and 50 μg/ml. It was found that cancer cell lines generated higher adhesion forces (as compared to MCF-10A cells) (fig. 1.8b).

Micropatterning (see below) was used to compare adhesion on substrates coated with HA (fig. 1.8c). Micropatterns were covalently linked with HA, and lower surface was coated by flaminin. Experimental results showed that non-tumorigenic MCF-10A cells, in contrast to MDA-MB-231 cells, adheres preferentially to HA.

Viscoelastic properties

The ability of a cell to move through small pores relies on its deformability. The mechanical deformability of both MCF-10A and MDA-MB-231 cells was measured by AFM (fig. 1.8d). In particular, the stiffness of the cytoplasm, nucleus and nucleoi were measured. For small indentation depths, the two cell lines had similar elastic moduli (around 200 Pa). For cancer cells, the stiffness of the cytoplasm and the nucleus did not depend on the indentation depth (whereas the stiffness of the nucleoi slightly increased with larger indentation). In contrast, for MCF-10A cells, the Young's modulus was found to increase with the indentation depth for the cytoplasm, the nucleus and the nucleoi. These findings suggest that the mechanical loads are transduced differently through the cytoskeleton (or the cytoplasm), the nucleus and the nucleoi in the two cell lines. The decreased elastic modulus and increased deformability of MDA-MB-231 cells is consistent with their ability to traverse through narrow channels (see above).

To measure the cytoplasmic viscosity, ballistic injection naorheology (BIN) experiments were performed. Fluorescent nanoparticles were injected in the cytoplasm and their
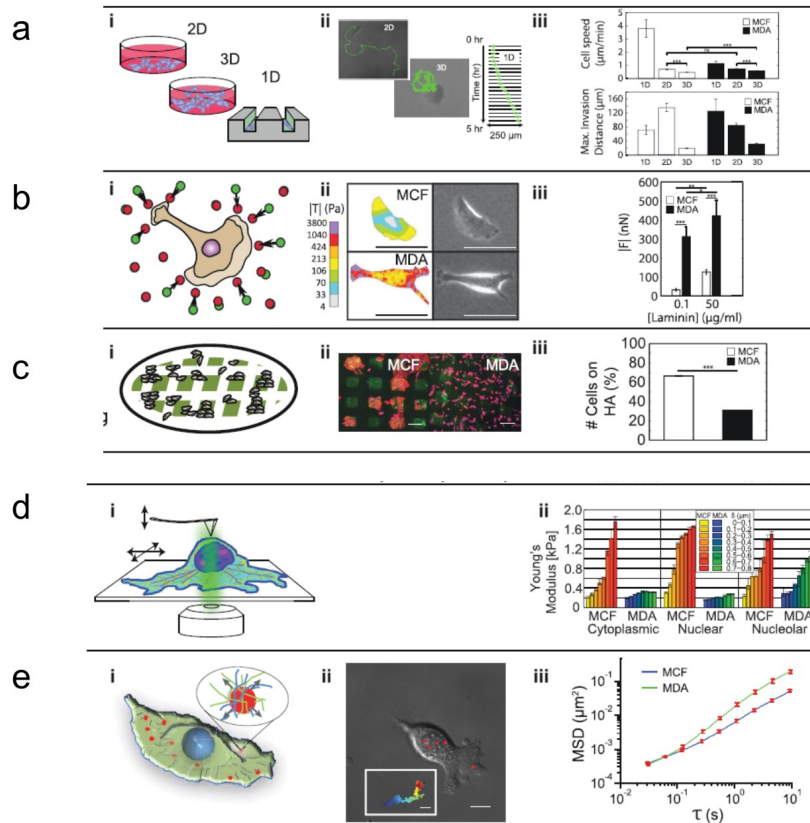
FIGURE 1.8: (a) Three substrates were used to monitor cell motility : 2D collagen-coated glass substrate, 3D collagen matrix, and 1D fibronectin-coated microchannels. (i) Schematic representation. (ii) Tracking data. (iii) Speed (mm/min) and maximum invasion distance. (b) TFM quantified traction stresses exerted by cells on 5 kPa 2D polyacrylamide substrates (that mimic the stiffness of mammary tumors). TFM consists in measuring the displacement of embedded fluorescent polystyrene beads. Shown are bead displacement magnitudes and the distributions of traction stresses. (i) Schematic representation. (ii) Tension maps (Left) ; phase images (Right) ; MCF-10A cells (Top) ; MDA-MB-231 cells (Bottom). Scale bars : 50 mm. (iii) Force magnitudes exerted by cells at different laminin concentrations. (c) Micropatterning. Microprinted arrays linked covalently with hyaluronic acid (HA). (i) Schematic representation. (ii) CD44 expressing MCF-10A and MDA-MB-231 cells (red) attached to FL-HA micro-patterned substrates (green) after 24h culture. Scale bars : 50 mm. (iii) Cells attached to HA (squares). (d) AFM measurements on the cytoplasm, nuclei, and nucleoli. Force-indentation curves were used to calculate the elastic moduli. (i) Schematic representation. (ii) Depth-dependent elastic moduli. (e) Fluorescent nanoparticles injected into cells and trajectory monitored over time. (i) Schematic representation. (ii) Cell monitored in real time. Inset : nanoparticle trajectory. Scale bars : 10 mm (main) ; 0.2 mm (inset). (iii) MSD values over total time. All figures are adapted from [47]

random movements were tracked after an overnight incubation (fig. 1.8e). From these measurements, mean squared displacement (MSD) values were obtained. The averaged MSD of microspheres in MDA-MB-231 cells was greater than that of MCF-10A cells, indicating that the MDA-MB-231 cytoskeleton is softer than the one of MCF-10A cells (in agreement with AFM data).

1.6 The role of the environment in cell fate

In many areas of biology (e.g. tissue engineering or gene therapy), it is critical to know or predict the future of cells. The possible *cell fate* decisions are : growth, differentiation or death. Cell fate depends on some external signals. These can be soluble factors (growth factors, cytokines, chemicals), insoluble factors (extracellular matrix molecules and immobilised adhesion ligands), an external mechanical stimulus or environmental factors. In this section we focus on the later factor.

Substrate stiffness

In the human body, the stiffness of tissues varies from 200 Pa (lung tissue) to few GPa (bones). Cell adhesion strongly depends on the stiffness of the substrate. To study cell adhesion, polyacrylamide gels, coated with collagen, are usually used. The elasticity of the gel depends on both the concentration of acrylamide monomers and bis-acrylamide crosslinkers. After they are seeded on the gel surface, cells start to adhere and spread on the gel surface. This process usually takes 10 to 12 hours. Experiments have shown the mean spread area of cells is higher for stiff gels [22] (fig. 1.9) and that a power law correctly describes the observed trends ($A = bE^n$, where A - is the cell surface area, E - Young's modulus, b and n). Interestingly, n was founded quite similar for different type of cells : 0.29 to 0.37 for smooth muscle cells [22] and 0.27 to 0.31 for human cell lines SW480 (derived from metastatic site with colorectal adenocarcinoma) [23]. In summary, cell respond to external stress (here the rigidity of the substrate) and this results in a modification of the shape and surface area.

Embryonic stem (ES) cells are pluripotent, so they can differentiate into any of the three germ layers : endoderm, mesoderm or ectoderm. The local environment crucial role in their fates. Substrate stiffness affects cell spreading, growth rate, gene expression and osteogenic differentiation of ES cells [28]. In particular, differentiation of ES cells is enhanced on stiff substrates : when mouse ES cells are cultured on a soft substrate (stiffness of 1 kPa), they still generate undifferentiated colonies after 5 days [49]. Moreover,
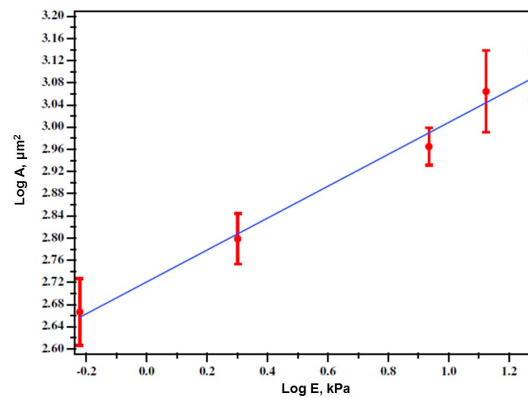
FIGURE 1.9: Log - log plot of the mean spread cell area as a function of the stiffness of the substrate. Adapted from [23]

it was recently shown that an external stress was sufficient to drive mouse ES cells to differentiate [29].

Cell invasion in a blood vessel

Cell invasion is one of the first steps of the metastatic process. Cells can invade the tissues around the primary tumor site either by a collective cell movement, or as single cells [30]. The endothelial tissue is the main barrier between the cell and the blood and should protect blood vessels from an invasion. Still, some cells may penetrate this barrier (this process is known as intravasation). When moving collectively, cells have to remodel the extra cellular matrix and promote focal adhesions (fig. 1.10a). Single cells undergo phenotypic changes such as the epithelial to mesenchymal transition, the collective to amoeboid transition and the mesenchymal to amoeboid transition (fig 1.10b and 1.10c).

Topographic changes

Microcontact printing (soft litography) is a technique, which allows to create 3D patterns on a soft substrate (e.g. PDMS). This technique is widely used to study the adhesion of the cells [19]. For instance, ECM molecules can be printed on non-adhesive glass slides and form islands. Such experiments have shown that the size of the islands (squares of 5 to 40 μm side lengths) determine both the spreading and the shape of the cells (as long as the area of the island is smaller that the maximum area of the cell during spreading). Microcontact printing has also demonstrated that the size of the islands influence cell differentiation : cells can proliferate on large islands (2500 μm^2), cells spread moderately and do not grow nor differentiate on smaller islands (1000 - 2000 μm^2) and cells die when
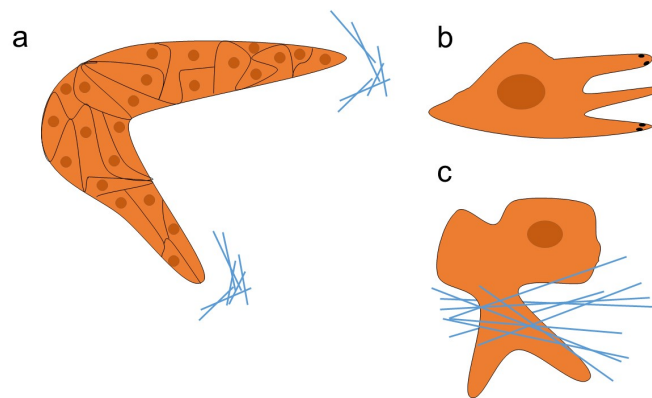
FIGURE 1.10: Plasticity of invading cancer cells. (a) In collectively invading cell strands, the tumor cell at the invasive front is designated as tip cell and executes the driving force by promoting focal adhesions and ECM rearrangement. (b) The mesenchymal-like cell is able to move freely by forming focal adhesions and rearranging the ECM by pseudopodia. The cells sustain a rearfront cell polarity. (c) The fastest way of cell invasion is the amoeboid cell movement, which leads to a total loss of cell polarity and fixed cell shape : the cell readily "seeps" through ECM.

grown on tiny islands (less than 500 μm^2).

Electron beam litography alows to fabricate nanoscale topographic structures that mimic the ECM network. Dalby *et al.* [50] have fabricated nanopits on PMMA. This substrate was embossed with 120-nm-diameter and 100-nm-diameter nanopits that were arranged in different geometries : a square pattern with 300 nm mesh size ; a disordered square array with dots displaced randomly by up to 20 nm on both axes (from their position in a true square) ; the same quasi-random distribution with a maximum of 50 nm disorder amplitude ; and pits placed completely randomly. When seeded on these nanopits, different expression levels of steocalcin and osteopontin (used as markers of osteoblastic differentiation) were found depending on the pit geometry.

1.7   NAMI-A as an anti-cancer agent

Platinum compounds are good anticancer drugs, which are actively used against wide range of cancer types. However, they shows side effects and development of tumor resistance to the drugs. So, scientists were searching for new metal-based anti-cancer drugs without drawbacks of platinum compounds. Ruthenium compounds could be good candidates for this role due to some specific properties :

1. ruthenium complexes collects mostly in tumor masses [104]

2. ruthenium could be found in the inert state - Ru(III) and reactive state - Ru(II). The energy barrier between two states is comparatively small, so they could circulate in the blood in the inert state, causing minimum damage for blood cells ; and then reduce to the more reactive when inside the cell. Moreover, in tumor tissue re-oxidation of Ru(II) to Ru(III) is less probable [103].

3. slow ligand exchanges rate in water solutions [105]. This rate is in order of cell lifetime, so it means that ruthenium ion, that is bound to the cell, more probably will remain bounded until cell die.

The first turhenium derived anti-cancer drug, that enter to the clinical trials is NAMI-A (Novel Anti-tumor Metastasis Inhibitor A). Molecular formula of NAMI-A is $C_8H_{15}C_{14}N_4ORu$ (see figure 1.11a).

NAMI-A is very stable in solid state, in solution it degrades with pH. Anti-cancer properties of this drug was proven on the metastasizing mouse adenocarcinoma cells [101]. Sava et al shows that the cells treated *in vitro* with NAMI-A for 1 hour have lower invasive and migration properties through the matrigel barrier. Cells were treated with concentration 0.1 mM of NAMI-A, that authors found non-toxic for the mouse adenocarcinoma cell line. Nevertheless, *in vivo* the ruthenium compound reduce primary tumor growth at quite large concentration - 137 mg/kg (the toxic dose for the mouse starts from the concentration 193 mg/kg).

After pre-clinical phase of clinical research, NAMI-A was tested on 31 patients of different types of tumor types (but mostly with adenocarcinoma - 19) [103]. Anti tumor activity of the drug was observed in 56 % of patients and stable disease for 6-8 weeks in 37 % of patients. NAMI-A was experienced by patients as a very intense treatment with the toxicity profile close to the drugs, based on the platinum compounds. Mainly it cause neutropenia (low concentration of neutrophils in the blood) and anemia (low concentration of red blood cells). At the moment, NAMI-A did not pass I phase of clinical trials, and additional trials are needed to make definitve conclusions.

Moreover, NAMI-A have a big influence on cell detachment. Brescacin et al. studied the human breast cancer cell line MDA-MB-231, treated with 100 μM of NAMI-A for 1 hour [108]. They observed the number of deadhered treated cells was twice higher than for non-adhered. Decrease of the adhesion properties of the cells could be caused by changes in the forces, produced by the cell. Measuring the cellular force field changes, caused by the anti-cancer drug could be the next step on the way of quantitave drug analyze.
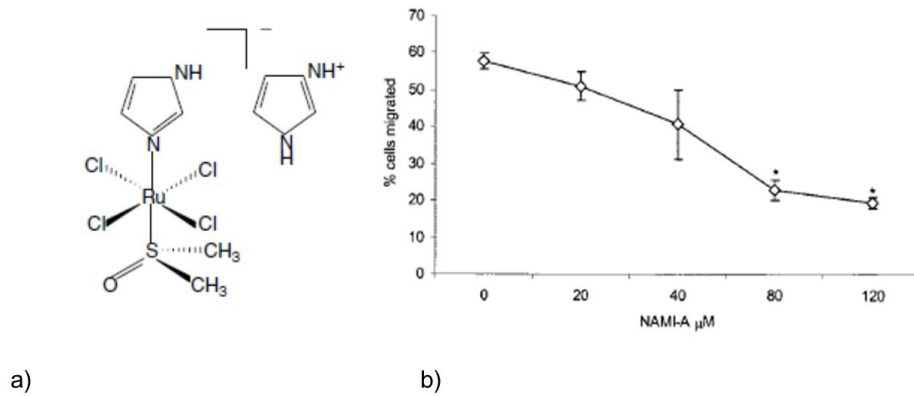
FIGURE 1.11: Figure a : molecular structure of NAMI-A. Adapted from [106]. Figure b : Effect of NAMI-A on invasion of metastasizing mouse adenocarcinoma cells through Matrigel-coated polycarbonate filters. Adapted from [101]

Outline

The main goal of our project is to perform experiments with the cellular force field measurements. As we didn't have any tool to perform such measurements, we define the key points of the research (and, respectively, manuscript) as :

1. Building setup to perform measurements of the force fields, caused by a cell.

2. Mathematical model, that allow us to calculate the force field from measured experimental data.

3. Force fields measurements of cancer cell line *SW 480*.

4. Preliminary results with anti-cancer drug NAMI-A.

Chapter 2

Traction Force Microscopy

2.1 Introduction

Many important physiological processes such as cell adhesion, differentiation, proliferation and cancer metastasis may be significantly influenced by cellular forces. Here, we present some important techniques that can measure the forces exerted by a cell.

Harris et al. [51] first proposed a method to visualize forces exerted by the cell onto a substrate. They used thin polymeric silicone substrates and observed wrinkles, caused by the traction of adherent cells (fig. 2.1a). Because there are no simple ways to convert wrinkles patterns into a traction forces map, this method remains qualitative and is not used nowadays.

Micropillar substrates can provide insight on cellular traction forces (CTF). Microposts are fabricated from a soft material (usually silicone) and their top surface is coated (e.g. with collagen) so that cells can specifically adhere (fig. 2.1c). To determine CTFs, one need to track the deflections of the microposts. Then, the force can be easily calculated using Hooke's law : $F = k\delta$, where δ is the horizontal deflection of the post, and k - is a constant, that depends on the Young's modulus and dimensions of the post [53] (see fig. 2.1b). The stiffness of the substrate is defined by the elasticity of the microposts and their height (short pillars are stiffer substrates). This technique is quite versatile and allow to determine CTF easily. Nevertheless it also has significant drawbacks : the non-physiological shape of these substrates might affect cellular responses. Moreover, cellular shapes are strongly affected are by the dimensions of the micropillars and the mesh size [54].

In contrast to micropillar arrays, Traction Force Microscopy (TFM) uses flat substrates. TFM consists in measuring the displacement of micron-sized (fluorescent beads)
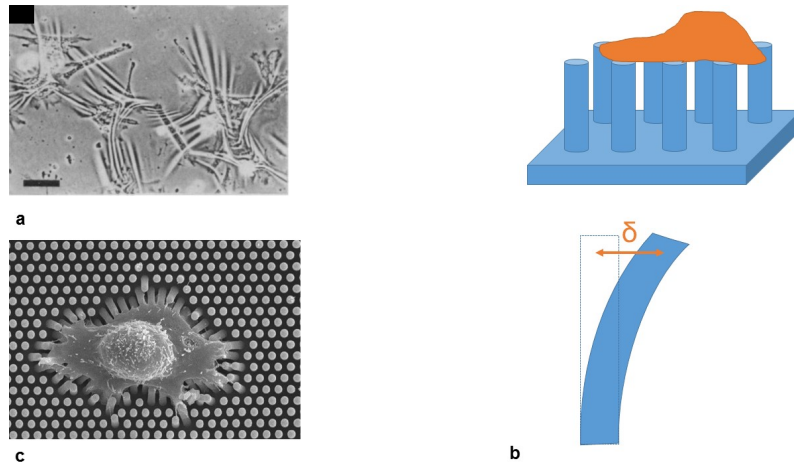
FIGURE 2.1: (a) Chick heart fibroblasts that had been spreading on a thin silicone rubber film and forming wrinkles on it (adapted from [51]). Scale bar : 100 μm. (b) Pinciple of the micropillar technique. Cells are seeded on top of the micropillars, which are coated with ECM protein. Forces are calculated from the pillar deflections . (c) A rat embryonic fibroblast (REF52 cell line) spreading on a bed of micropillars (adapted from [55])

embedded in a polyacrylamide 3D gel when cells are seeded on a collagen surface (2D TFM) or when they move in a 3D extracellular matrix environment (3D TFM). From the displacement of beads (usually measured by confocal microscopy when using fluorescent beads), vector maps of traction forces (forces applied by the cell on the gel) can be determined. To do so, the position of the beads in a "stress-free" state (before cell seeding) is required. In addition, the elastic properties of substrate (Young's modulus, Poisson's ratio) have to be known. Notice that a wide range of forces can be determined as the substrate stiffness can be easily tuned (e.g. by varying the concentrations of monomers and cross-linkers in a poly-acrylamide gel).

A typical TFM experiment comprises several steps :

1. fabricating a soft substrate with fluorescent beads, and coating the substrate surface,

2. obtaining a pair of fluorescent beads images ("stress-loaded" and "zero-stress" images),

3. using the two types of images to determine the substrate displacement field and

4. calculating the CTF field from the substrate displacement field.

2.2   Displacement field measurements

In this section, we discuss the experimental part of TFM that consists in measuring the deformation field within the elastic substrate.

$$\vec{d}(\vec{r}, t) = \vec{r}(t) - \vec{r}\,(t = 0)$$
$$\vec{d}_{TR}(\vec{r}, t) = \vec{d}_{CTF}(\vec{r}, t) + \vec{d}_{drift}(\vec{r}, t)$$
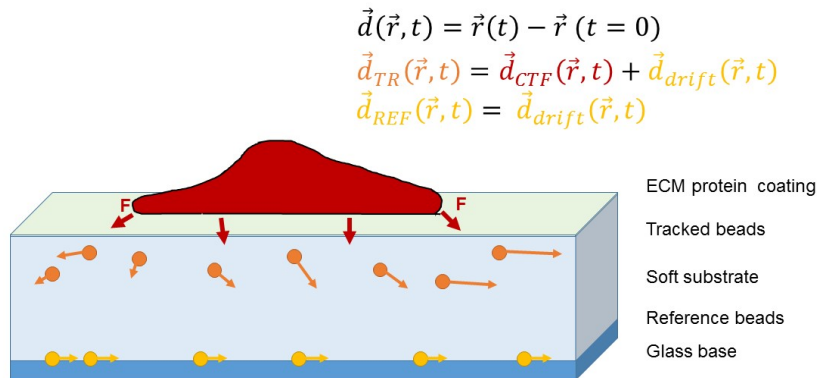$$\vec{d}_{REF}(\vec{r}, t) = \vec{d}_{drift}(\vec{r}, t)$$

FIGURE 2.2: Schematic diagram of a TFM substrate. A soft substrate (light blue) is bonded to a rigid base (blue). Fluorescent beads are embedded at the substrate base (yellow), and near its surface (orange). Cellular forces F are applied to a substrate displacing it by a distance d, that is depends on time and coordinates. Note that the displacement of all beads are affected also by drift.

2.2.1 Typical protocol for displacement field measurements in TFM

The substrate material should be soft enough (to accurately measure its deformation) and sufficiently stiff (to have small deformations and not exceed a linear-response regime). Typical substrates are : polyacrilamide (PAA) gels, polydimethylsiloxane silicone (PDMS) gels and elastomers. PAA gels are typically softer (stifness is in range : 100 Pa - 100 kPa) than PDMS gels (from 2 kPa to 2 MPa). The Young's modulus of these gels can be tuned by varying the concentration of monomers [55] and its value can be accurately determined (using a a cone-plate rheometer or by measuring the indentation of a mm-sized steel ball [56]).

Usually the gel is fabricated in a petri dish and the fluorescent beads are added to the gel before it polymerizes. The gel has to be thick enough so that it can be considered as a semi-infinite medium (the forces at the bottom of the gel should be then zero). Still the thickness has to be compatible with the working distance of the objective. In practice, the gel is between 50 and 100 μm thick. Because the experiment is subjective to mechanical drift, reference beads are melted to the glass surface (fig 2.2).

The surface of the substrate is coated with ECM proteins, such as collagen, gelatin or laminin. These proteins are covalently attached to the gel using cross-linkers (e.g.

Sulfo-Sanpah). The concentration of proteins is chosen to allow a proper spreading of the cells[1].

Cells are then seeded on the surface of the gel. The acquisition starts after the cells have adhered to the gel (after about 6 hours). A field of view is chosen and a phase contrast image (or a fluorescent image) of the cells is taken. Thereafter, fluorescent images of the micron-sized beads are acquired (force-loaded images). Due to the finite depth of field, the microscope objective is placed on a piezo-electric device : this allows to acquire bead images at different planes. To increase optical resolution and contrast, confocal fluorescence images are acquired. Confocal (fluorescence) microscopy is a classical optical technique, which allows to decrease significantly out-of-focus light (a pinhole is placed in front of the detector in a plane conjugated with the image plane, fig 2.3, left figure). Confocal microscopy enables the reconstruction of 3D images of the sample : by moving the specimen, sets of 2D images are acquired at different focal planes (optical sectioning, fig 2.3, right figure). These 2D images (slices) can then be interpolated to calculate a 3D image [65].

Fluorescent images have a typical shape that resembles an Airy pattern (the point spread function (PSF) convoluted with the bead shape). The Airy disk is an important parameter as it enables to calculate the resolution of the microscope. Assuming two point sources, the lateral resolution reads :

$$r_{xy} = \frac{1.22\lambda}{2NA} \approx 0.6\frac{\lambda}{NA} \tag{2.1}$$

where λ is the wavelength of the emitted light and NA is numerical aperture. r_{xy} is simply the minimum distance between two points where they can be distinguished as separate. In optical microscopy (and for typical Signal to Noise ratio), r_{xy} is a few hundred nanometers. Note that resolution is not localization : the maximum of the PSF can be determined with an accuracy that is much better than r_{xy} and that scales as $FWHM/\sqrt{N}$, where FWHM is the Full Width at Half Maximum of the PSF and N is the number of photons. Having a sufficient number of photons (photo-electrons on the detector), the location of an object can be estimated down to 1/100 of a pixel[2] [66].

As seen in Fig. 2.3 (left panel), the point spread function of the pinhole is an ellipsoid, several times as long as it is wide (fig 2.3, left figure). Therefore, the axial resolution is

---

1. Note that there might be an optimal protein concentration, which depends on the gel stiffness [64]).
2. Assuming the noise level to be constant on each image, averaging subsequent images allows to reach sub-nanometer resolutions.
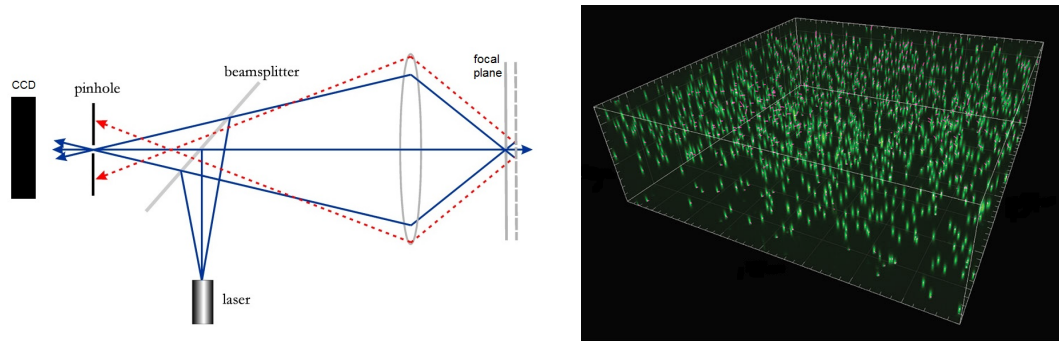

FIGURE 2.3: Left : a typical confocal microscope. Light, emitted from all planes out of focal plane, are filtered by a pinhole in front of a CCD camera. Right : a 3D image of a sample with fluorescent beads, reconstructed by 3D confocal microscopy. Adapted from [67]

not as good as the lateral resolution and reads :

$$r_z = \frac{1.4n\lambda}{NA^2} \tag{2.2}$$

where n is the refractive index between the sample and the lens.

In TFM, the spatial resolution of the displacement field depends on the density of beads as well as the accuracy in the displacement measurement. Smaller beads allows to achieve higher densities at the expense of an increase in tracking noise. Finally, one should consider that fluorescent beads might show a decrease in fluorescence intensity (especially for long-term experiments) and that this might affect the resolution.

At the end of the experiment (typically after 10 to 15 hours), trypsin is injected in the flow cell. This removes adherent cells from the gel surface and allows to calculate a "null-force" field.

2.2.2   2D displacement field for 2D cell motion

Instead of embedding fluorescent reporter beads in the gel (which might give rise to a high background noise), Marinkovic et al. [58] proposed to use gel-surface-bound fluorescent beads. The beads are then arranged on a 2D lattice on the surface without impacting the cellular contractile function. To accurately determine the area on which forces are exerted, it is important to image the cells during the course of the experiment. To this aim, total internal refractive fluorescence (TIRF) can be used as this allows to obtain high-contrast images of fluorophores near the plasma membrane [59]. For such experiments, the refractive index of the substrate (gel) has to be larger than the cell

medium (say 1.33). As PAA does not fulfill this requirement, some silicon materials (which have to be transparent) could be used. As shown by Y. Iwadate *et al.* [59], such techniques allow to simultaneously track fluorescence beads and cells (expressing GFP - ABD120k, which reflects the distribution of filamentous actin) while keeping the noise level to a minimum.

As stated above, the spatial resolution of TFM is determined by the spatial sampling of the displacement field, which is limited by the density of micro-beads and the optical resolution of the microscope. The density of beads is limited by the necessity to resolve individual beads. To overcome this limitation, Plotnikov *et al.* have used two different types of beads (with different excitation wavelengths) and have successfully analyzed traction forces at the sub-micrometer scale.

2.2.3   3D displacement field for 2D cell motion

In this section, we discuss some techniques that can estimate the x, y and z positions of the bead reporters.

3D images of the substrate (gel) can be acquired using fluorescent microscopy. In confocal fluorescence microscopy, stacks of fluorescent images at different focal planes positions can be measured (see above). Some techniques (e.g. Digital Volume Correlation, DVC [61]) allow to calculate the displacement field : two 3D fluorescent images are measured (with and without a mechanical loading) and are then subdivided into a set of sub-volumes. Using each pair of sub-volume images, the respective local displacement vectors can be obtained from a 3D volume correlation method. This method works as follows : consider two signals $f(\vec{r})$ and $g(\vec{r})$, which represent a pair of corresponding sub-volumes V with and without mechanical loading (fig 2.4a). The cross-correlation function depends on the displacement vector $\vec{d}$: $c(\vec{d}) = \int f(\vec{r})g(\vec{r}-\vec{d})dV$ and the value of the displacement vector $\vec{d}$ corresponds to the maximum of the cross-correlation function.

A similar method was used by del Alamo *et al.* [63]. They have shown that the size of the sub-volume affects the accuracy of the displacement field. Thus, a smaller sub-volume size (high spatial resolution of the displacement field) introduces a large error in the sub-volume displacement measurement. Note that the size of the sub-volume is smaller along the z direction and so the accuracy is better in z direction (see table 2.1).

The 3D displacement field could be obtained with a higher spatial resolution if one tracks the xyz positions of single fluorescent microbeads. In this case, the so-called "three-dimensional defocused particle tracking" method can be used [62]. As written above, the bead is convoluted (folded) by the PSF and so its image shows a central bright spot and
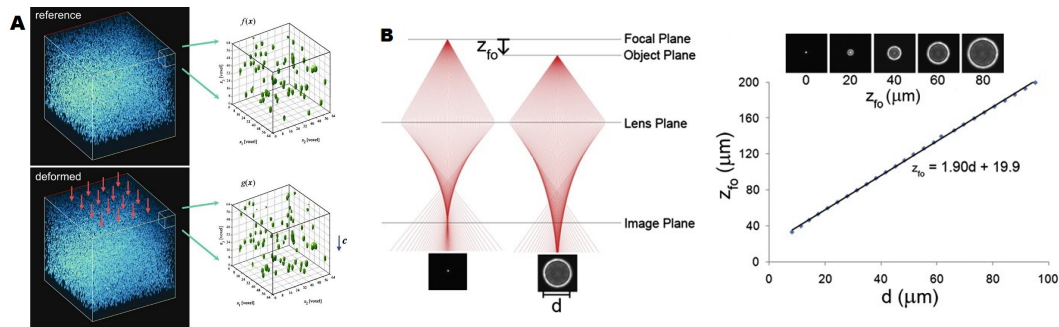
FIGURE 2.4: (a) Schematic illustration of the digital volume correlation. Sub-olumes of substrates are correlated in a stress-free (reference) state and in a deformed state. Adapted from [61] (b) Three-dimensional defocused particle-tracking method. Left : A ray-tracing diagram of light traveling through a lens. The source of light in the focal plane converges to a point at the image plane. If the point source is displaced by a distance z_{f_0}, rays do not converge and they produce a defocused ring on the image plane (diameter d). Representative images of a point source under each condition are also shown (bottom). Right : Experimentally derived calibration curve of fluorescent beads. Adapted from [62]

additional rings. For out-of-focus images, the ring radii vary and so a calibration curve (z position *versus* the radius of the ring) can be obtained (fig 2.4b, right panel).

2.2.4   3D displacement field for 3D cell motion

As cells are able to move within tissues, 3D TFM has received much attention recently. *In vivo*, cells undergo migration in dense connective tissues, in loose connective tissues or in a tightly packed basement membrane organized as a thin, dense acellular layer. The movement is expected to be different in 3D (as compared to 2D) as the area of the cell that senses the local environment is typically larger.

TABLE 2.1: Comparison of different types 3D TFM techniques

	Spatial resolution - xy(z), μm		accuracy of the displacement field measurements - xy(z), μm		reference
Digital volume correlation (cubic volumes)	0.45	(0.45)	0.054	(0.292)	[61]
3D defocused particle tracking method	20	(20)	0.2	(0.4)	[62]
Digital volume correlation ("thin" parallelepipeds volumes)	0.7	(0.7)	0.14	(0.15)	[63]
	1.4	(0.7)	0.09	(0.08)	
	2.7	(0.7)	0.07	(0.06)	
	5.6	(0.7)	0.07	(0.05)	

To build 3D matrices *in vitro*, different ECM proteins can be used. Collagen is a widely used protein as it is the main structural protein in the extracellular space : it is present at sites where lymphocyte migration needs to halt, including lymphoid tissues and inflammation sites, and also tumors. Fibrin gels are also commonly used substrates for fibroblast and tumor cell migration studies. The cleavage of fibrinogen by Thrombin will generate fibrin, which self-assembles to form a tight mesh-work of fibers. Another point that has to be considered is the following : removing the cells from a 3D substrate (to obtain a "stress-free" force field) is impossible without damaging the matrix. Therefore, cells are treated by chemicals, which are able to "switch-off" cellular forces.

Legant *et al.* [68] studied the traction force field of bovine pulmonary artery smooth muscle cells, human mesenchymal stem cells and Lewis lung carcinoma cells in a 3D hydrogel (this differs from typical experiments where the 3D matrix is built from ECM proteins). Enhanced GFP (EGFP)-expressing fibroblasts were encapsulated in polyethylene glycol (PEG) hydrogels. The incorporation of adhesive and degradable domains permitted the cells to invade, spread and adopt physiologically relevant morphologies. The elastic properties of the gel was measured with an oscillating rheometer (a rough estimation of the Young's modulus was in between 600 and 1000 Pa). Images were taken with a standard 3D confocal microscope (3 minutes per sample scan). To obtain a relaxed (reference) state of the gel, cells were treated with 0.5% SDS. This detergent was chosen to completely denature all cellular proteins (which might not be the case with milder detergents or specific inhibitors of the cytoskeletal contractility). In order to precisely determine the matrix deformation around a single cell, 60 000 to 80 000 fluorescent beads were measured.

Tracking a large number of beads require special algorithms : in a first step, bead centroids are found with a three-dimensional fracshift scheme (as proposed in [69]) ; in a second step, beads images in the "stressed" state were matched to beads in the relaxed state using a vector-based algorithm that relates the relative position of each bead to its local neighbors. For each target bead to be matched in the stressed dataset, vectors were generated (fig 2.7, left, a). Candidates matches for the target bead in the relaxed dataset were identified as those beads nearest to the spatial coordinates of the target bead in the stressed dataset (fig 2.7, left, b). For 0.5 μm diameter beads, the position accuracy of 0.5 μm diameter beads was found to be 0.08 μm (xy) and 0.2 μm (z), respectively ; the spatial resolution was found to be is 0.3 μm (xy) plane and 0.8 μm (z), respectively.

Lesman et al [70] also measured the displacement field induced by fibroblast dividing cells in 3D fibrous matrices (using confocal imaging and a DVC algorithm). They used a fibrin gel (stiffness of 100 Pa), which exhibits fibrillar morphologies and shear moduli
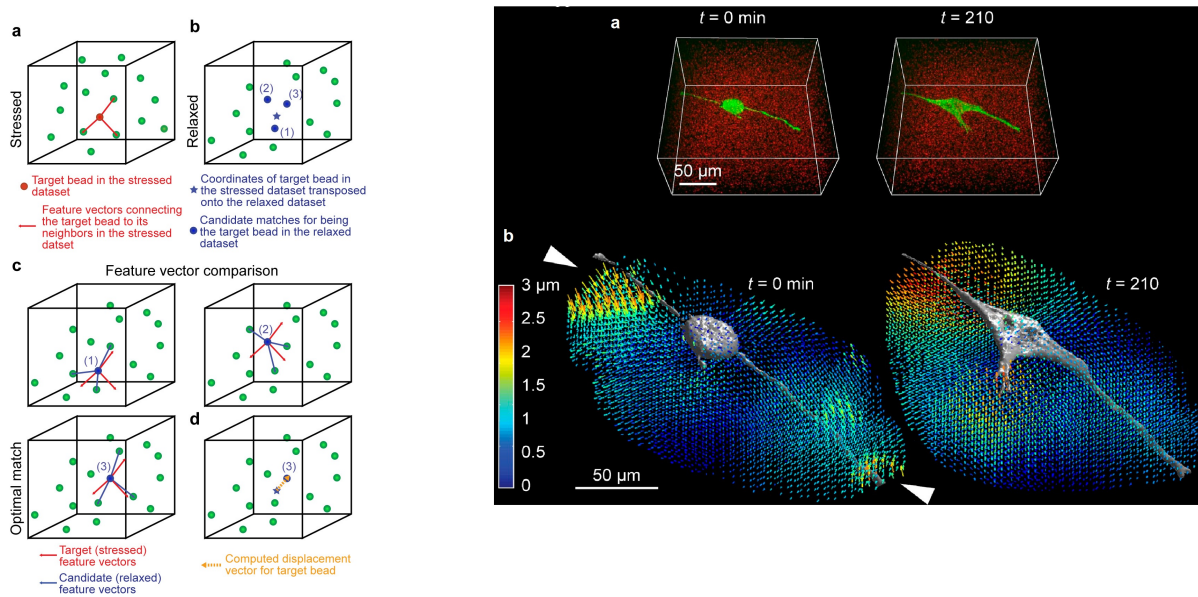
FIGURE 2.5: Left (a-d) : schematic illustration of the principle of the displacement field calculation (in the case of a large bead concentration, see text). Right (a) : 3D confocal images of a dividing cell and fluorescent beads taken before and after cell division (fibrin matrix). (b) The displacement field showed the largest gel deformation around thin cellular protrusions. Adapted from [70]

characteristic of compliant tissues such as the mammary gland and the brain. After cell division, the gel was treated with blebbistatin (which inhibits myosin II contractility but does not disrupts the initiation of mitosis). Images were taken with a confocal microscope (fig 2.7, right). The accuracy in the displacement field was 0.3 μm in all directions. This study demonstrates that, during division, cells release adhesive contacts near the cell body (while applying tensile forces at the tips of the protrusions after cytokinesis) and that daughter cells migrate into matrix voids (while maintaining traction forces at the tips of newly formed protrusions).

2.3 Computation of the stress field

In the previous sections, we have shown how to calculate the displacements of bead reporters. The next step consists in the calculation of the force field. For small displacements, linear elasticity models can be used. In such models, the relation between the

stress $\vec{F}(\vec{r})$ and the displacement $\vec{u}(\vec{r})$ fields reads :

$$u_i(\vec{r}) = \int G_{ij}(\vec{r} - \vec{r'}) F_j(\vec{r'}) dr' \tag{2.3}$$

(2.3) is a Fredholm integral of the first kind. Here $i, j = 1, 2, 3$ are indexes that reefer to the x, y, z positions, the vector coordinates and the the Green function ($r_1 = x, r_2 = y, r_3 = z, u_1 = u_x, G_{12} = G_{xy}, ...$), respectively.

Because both the displacement and force field are measured at discrete positions (the location of the beads and the focal adhesions), the integral in (2.3) can be rewritten as a set of linear equations : $\vec{u} = G\vec{F}$, where $\vec{u} = (u_1(r^{\vec{(1)}}), u_2(r^{\vec{(1)}}), u_3(r^{\vec{(1)}}), u_1(r^{\vec{(2)}}), u_2(r^{\vec{(2)}}), ...)$ and $\vec{F} = (F_1(r'^{\vec{(1)}}), F_2(r'^{\vec{(1)}}), F_3(r'^{\vec{(1)}}), F_1(r'^{\vec{(2)}}), F_2(r'^{\vec{(2)}}), ...)$ are vectors, and G is a matrix. Measurement locations are written as subscripts, *i.e.* the locations at which the displacement field u (e.g. beads, which are tracked) and the force vectors ("force points") are computed. For N displacements and M force points, the size of the displacement vector (at 3 dimensions) is $3N$, the size of the force vector is $3M$ and the Green matrix has a size of $3N$x$3M$, respectively.

Both $\vec{u}$ and $\vec{F}$ do not contain any information on the localization of points. In the case of a semi-infinite medium (a force applied to one side of the substrate has a negligible effect on the opposite side, e.g. for a thick or stiff substrate), the Green function can be computed [71]. Note that the estimation of the Green function also requires to determine both the Poisson ratio (ν) and Young's modulus (E) of the substrate. Hydrogels (often used in TFM) are almost incompressible (Poisson ratio $\sim \nu = 0.5$). In that case, the expression of the Green matrix can be simplified (the matrix elements are symmetric with respect to the x, y, z components) :

$$G_{ij}(\vec{r}) = \frac{3}{4\pi E r^3}(\delta_{ij} r^2 + r_i r_j) \tag{2.4}$$

Here, the Green matrix correlates each point of the displacement field ($\{r^{\vec{(1)}}, r^{\vec{(2)}}, ...\}$) with each point of the force field ($\{r'^{\vec{(1)}}, r'^{\vec{(2)}}, ...\}$) (for an elastic material). Note that the force points can be chosen on the cell or at the locations of focal adhesions (assuming they lie on the surface of the gel, *i.e.* the surface on which the cells are seeded).

G is the following $3N$x$3M$ matrix :

$$
\begin{bmatrix}
G_{11}(r^{\vec{(1)}} - r'^{\vec{(1)}}) & G_{12}(r^{\vec{(1)}} - r'^{\vec{(1)}}) & G_{13}(r^{\vec{(1)}} - r'^{\vec{(1)}}) & G_{11}(r^{\vec{(1)}} - r'^{\vec{(2)}}) & G_{12}(r^{\vec{(1)}} - r'^{\vec{(2)}}) & \dots \\
G_{21}(r^{\vec{(1)}} - r'^{\vec{(1)}}) & G_{22}(r^{\vec{(1)}} - r'^{\vec{(1)}}) & G_{23}(r^{\vec{(1)}} - r'^{\vec{(1)}}) & G_{21}(r^{\vec{(1)}} - r'^{\vec{(2)}}) & G_{22}(r^{\vec{(1)}} - r'^{\vec{(2)}}) & \dots \\
G_{31}(r^{\vec{(1)}} - r'^{\vec{(1)}}) & G_{32}(r^{\vec{(1)}} - r'^{\vec{(1)}}) & G_{33}(r^{\vec{(1)}} - r'^{\vec{(1)}}) & G_{31}(r^{\vec{(1)}} - r'^{\vec{(2)}}) & G_{32}(r^{\vec{(1)}} - r'^{\vec{(2)}}) & \dots \\
G_{11}(r^{\vec{(2)}} - r'^{\vec{(1)}}) & G_{12}(r^{\vec{(2)}} - r'^{\vec{(1)}}) & G_{13}(r^{\vec{(2)}} - r'^{\vec{(1)}}) & G_{11}(r^{\vec{(2)}} - r'^{\vec{(2)}}) & G_{12}(r^{\vec{(2)}} - r'^{\vec{(2)}}) & \dots \\
\vdots & \vdots & \vdots & \vdots & \vdots & \ddots
\end{bmatrix}
$$

$$(2.5)$$

From equation 2.4, it follows that $G_{ij}(\vec{r}) = G_{ji}(\vec{r})$ for materials with $\nu = 0.5$ [3].

Solving the set of linear equations

$$\vec{u}(\vec{r}) = G(\vec{r} - \vec{r'})\vec{F}(\vec{r'}) \tag{2.6}$$

is a direct problem (given the cause, we have to calculate the corresponding effect) : if the force field $\vec{F}$ is known, then the strain field $\vec{u}$ can be computed. In the case of TFM, the problem is inverse : the CTF field has to be derived from the measured displacement field. This can be done by inverting the Green matrix G. Note, however, that the problem be well-posed or ill-posed. The problem is said to be well-posed when the following conditions are fulfilled : uniqueness of the solution, existence of a solution and stability of the solution.

To discuss the stability of the solution, we have to introduce a parameter known as the condition number . Let us assume we have to solve an inverse problem : $A\vec{x} = \vec{b}$, where A is a matrix and $\vec{x}$ ($\vec{b}$) is unknown (input) vector. For small perturbations, we have :

$$A(\vec{x} + \delta\vec{x}) = \vec{b} + \delta\vec{b} \tag{2.7}$$

$$A\delta\vec{x} = \delta\vec{b} \tag{2.8}$$

$$\delta\vec{x} = A^{-1}\delta\vec{b} \tag{2.9}$$

Taking the norm on both sides and using the inequality $\|Ab\| \leq \|A\|\|b\|$, we obtain :

$$\|\delta\vec{x}\| \leq \|A^{-1}\|\|\delta\vec{b}\| \tag{2.10}$$

$$\frac{\|\delta\vec{x}\|}{\|\vec{x}\|} : \frac{\|\delta\vec{b}\|}{\|\vec{b}\|} \leq \frac{\|A^{-1}\|}{\|\vec{x}\|}\|\vec{b}\| \tag{2.11}$$

---

3. This does not mean that the matrix G is symmetric (eq. 2.5).

Using the initial equation, we can replace $\vec{b}$ with $A\vec{x}$ and use the inequality $\|Ab\| \leq \|A\|\|b\|$. This gives :

$$\frac{\|\delta\vec{x}\|}{\|\vec{x}\|} : \frac{\|\vec{\delta b}\|}{\|\vec{b}\|} \leq \frac{\|A^{-1}\|}{\|\vec{x}\|}\|A\vec{x}\| \leq \frac{\|A^{-1}\|}{\|\vec{x}\|}\|A\|\|\vec{x}\| = \|A^{-1}\|\|A\| \tag{2.12}$$

The condition number of the matrix A is defined as the maximum possible ratio between the relative error of the solution and the relative error of the input data. From equation 2.12, we obtain the final expression for the condition number : $k(A) = \|A^{-1}\|\|A\|$. The condition number of a matrix (or a function) shows how much the output value can change for a small change in the input argument. Therefore, a small condition number ($k(A) \approx 1$) reffers a to stable solution. In contrast, for condition numbers larger than 10, the solution is non stable (or, in other words, a small error in $\vec{b}$ will introduce large inaccuracy in $\vec{x}$). In TFM the condition number of the Green matrix usually is larger than 1000 (large errors in the force field can be caused by a small fluctuation of the displacement field). In summary, Equation 2.6 in TFM is an ill-posed problem and a regularization has to be applied (see below).

2.3.1 Regularization in real space

There are different regularization methods, which consist of introducing an additional information to solve an ill-posed problem. Tikhonov regularization [72] consists in introducing the value $\vec{F}_0$. The force field is determined by minimizing both the quantity $\chi^2 = |G\vec{F} - \vec{u}|^2$ and the term :

$$\vec{F}_{reg} = min_{\vec{F}}\Big(|G\vec{F} - \vec{u}|^2 + \lambda^2|\vec{F} - \vec{F}_0|^2\Big) \tag{2.13}$$

where λ is a *regularization parameter*, which determines the strength of the regularization. If $\lambda = 0$, there is a direct solution ; large λ values will reduce the importance of the first term in (2.14). An optimal value for the regularization parameter can be found using the *L-curve criterion* [73]. The L-curve is a log-log plot of the norm $|G\vec{F} - \vec{u}|^2$ versus the regularized term $|\vec{F} - \vec{F}_0|^2$ for different λ. The L-curve criterion determines the value of the regularization parameter λ : this is the point at which the residual norm starts to increase significantly as a function of the regularized term. The name of this criterion comes from the fact that for discrete ill-posed problems, a plot of $|G\vec{F} - \vec{u}|^2$ versus $|\vec{F} - \vec{F}_0|^2$ has usually a L-shape. Reginska in [74] proved that the log-log L-curve is always
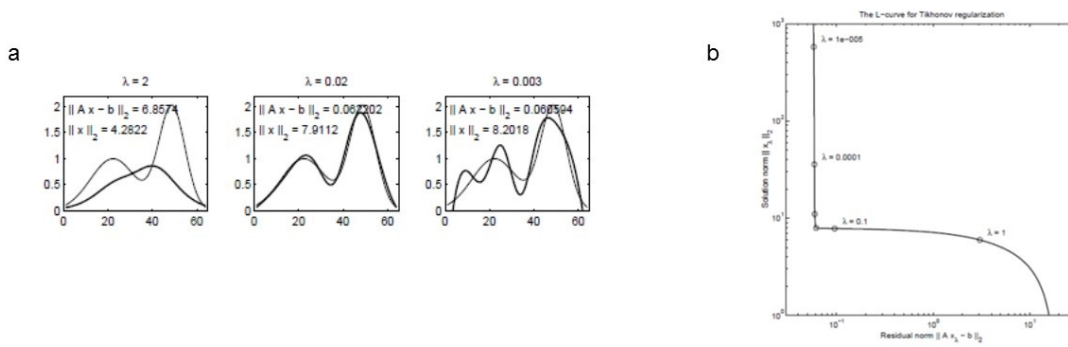
FIGURE 2.6: Figure (a) : the exact solution (thin lines) and Tikhonov regularized solutions x (thick lines) for an inverse problem $Ax = b$ (for three values of the regularization parameter). An over- or under-estimation of λ yields an over- or under-smoothing of the regularized solution. Figure (b) : the L-curve for a zero-order Tikhonov regularization of the same problem as in figure (a). Adapted from [73]

strictly concave for values of λ that are (i) smaller than the smallest singular value of the matrix and (ii) larger than the largest singular value. So, the L-curve is always concave and it "ends" near the axes (see figure 2.6b). The "corner" of the L-curve corresponds to the optimal balance between data agreement and regularization process, and this corner determines the value of λ.

Cells on flat substrates may exert forces on any directions, and it is therefore difficult to predict some types of force fields. Because the algorithm tends to reflect small values in the displacement field with large forces, an inversion without a regularization can lead to very large forces. Therefore, a reasonable assumption is that traction forces should not become very large. In this case, a zero-order Tikhonov regularization is used :

$$\vec{F}_{reg} = min_{\vec{F}}\Big(|G\vec{F} - \vec{u}|^2 + \lambda^2|\vec{F}|^2\Big) \tag{2.14}$$

2.3.2   Improvements of the regularization process in real space

The procedure presented above describes a classical computational method. Nevertheless, this procedure is often modified depending on the TFM experiment. Barentin *et al.* [75] have used an iterative biconjugate gradient inversion method. Here, the residual norm $\vec{r} = G\vec{F} - \vec{u}$ is set to zero and the following function has to be minimized :

$$f(\vec{F}) = \frac{1}{2}\vec{F}^T G\vec{F} - \vec{F}^T\vec{u} \tag{2.15}$$

This function is minimized in an iterative process : from the force field, $(\vec{F}(k))$ obtained

at a step k, the displacement field is calculated : $\vec{u}(k+1) = G\vec{F}(k)$ (the residual norm $r(k+1)$ is always smaller than $r(k)$). Two parameters (see below) are used to determine the convergence :

– The mean relative error on the calculated displacements :
$E(k) = \frac{1}{N}\sum_{l=1}^{N}\sqrt{(u_1^{(l)}(0) - u_1^{(l)}(k))^2 + (u_2^{(l)}(0) - u_2^{(l)}(k))^2}$ (for 2D case), which characterizes the difference between the measured displacements $\vec{u}(0)$ and the calculated displacements $\vec{u}(k) = G\vec{F}(k)$ at step k for all points.

– The ratio between the mean value of forces outside and inside the cell area : $\Phi = \frac{<|\vec{F_{out}}|>}{<|\vec{F_{in}}|>}$

To check the applicability of the method, simulations were performed with known force fields. At the k-th step, the difference in force between the original force field $F(0)$ and calculated one $F(k)$ reads :

$$\Delta F(k) = \frac{\sum_{l=1}^{N}\sqrt{(F_1^{(l)}(0) - F_1^{(l)}(k))^2 + (F_2^{(l)}(0) - F_2^{(l)}(k))^2}}{\sum_{l=1}^{N}|\vec{F}^{(l)}(0)|} \tag{2.16}$$

The authors show that the minima of both ΔF and Φ coincide. This means that Φ is a good criterion to choose the optimal number of iterations and to evaluate the error in the force. In addition, the authors propose that a more general criterion is given by the displacement error $E(k)$: the optimal k is chosen when $E(k)$ reaches the experimental error.

Using a simulated force field, Barentin *et al.* demonstrate that this iterative method allows a detailed reconstruction of the 2D stress field when the noise of the displacement field is not too high (less than 6%). However, this accuracy is difficult to achieve experimentally and so this method is rarely used [4].

Dembo *et al.* [79] propose to use a boundary element method (BEM) for the regularization. This consists in using the given boundary conditions to fit boundary values in the integral equation. In a first step, a boundary for the computational mesh is established as the cell boundary. Then, a set of nodes is created above each measured displacement (*i.e.* located inside the computational boundary). Finally, a triangular grid is created using a Delaunay triangulation. In some cases, the density of nodes could be increased manually

---

4. For low noise levels, the iterative biconjugate gradient inversion method gives more robust results that the explicit regularization method.

Ch. 2. Traction Force Microscopy

at locations where the force is localized. For the BEM method, Equation (2.6) reads :

$$\vec{u_i}(\vec{r}) = \sum_j \sum_{r'} M_{ij}(\vec{r}, \vec{r'}) \vec{F_j}(\vec{r'}) \tag{2.17}$$

Here, the matrix $M(\vec{r}, \vec{r'}_i)$ contains an information about all the triangles surrounding the node $\vec{r'i}$:

$$M_{ij}(\vec{r}, r'^{\vec{(i)}}) = \sum_{triangles} \int_{triangles} G_{ij}(\vec{r}, r^{(\vec{tri})}) P(r'^{\vec{(i)}}, \vec{r}^{(tri)}) d\vec{r}_{tri} \tag{2.18}$$

where $\vec{r}_{tri}$ are the continuous coordinates within the triangle and $P(\vec{r'}_i, \vec{r}_{tri})$ is a shape function, which interpolates the solutions between the discrete values obtained at the mesh nodes. To make the whole process more efficient and faster, the expression of the Green function was approximated differently for the near, intermediate and far fields (this improvement was proposed in [78]).

In the near filed($|\vec{r} - \vec{r'}| \to 0$), the Green function, which scales as $1/|\vec{r} - \vec{r'}|$, diverges. This problem is solved by using polar coordinates and nodes located on top of each displacement points. The distance-dependence of the Green function can be removed using a functional determinant. In the intermediate field, the integral in (2.18) is re-written in barycentric coordinates, so that shape functions are used (this facilitates the integral calculation). In the far field $(1/|\vec{r} - \vec{r'}| \to 0)$, the Green function is expanded in series around the center of mass of each triangle. Thus, the function that has to be minimized reads (for a zero-order Tikhonov regularization) :

$$\left|\left| \vec{u_i}(\vec{r}) - \sum_{j,\vec{r'}} M_{ij}(\vec{r}, \vec{r'}) \vec{F_j}(\vec{r'}) \right|\right|^2 + \lambda^2 \left|\left| \sum_{j,\vec{r'}} \vec{F_j}(\vec{r'}) \right|\right|^2 \tag{2.19}$$

The BEM method works best at high bead concentration or when the noise level in the displacement field is low.

In a first step, the regularization is not constrained. Nevertheless, the traction stress must satisfy a set of biomechanical constraints. A framework, which formulates the inverse problem as a constrained minimization, has been proposed [76]. In this model, the three biomechanical conditions are : the localization constraint (all forces outside the cell boundary should be equal to zero), the zero force constraint (the sum of all force vectors, produced by the cell, has to be zero) and the zero moment constraint (the sum of all moments of the cell has to be zero).

The authors have proposed a mathematical model (based on Tikhonov regularization)

in which a localization and a zero force constraints were added to the projection operator.

A force reconstruction inside a 3D collagen substrate was developed in [77]. As collagen has a non-linear force-displacement response, the methods described above could not be used. The displacement field was measured experimentally and simulated using the following minimization function :

$$L(\vec{u}) = ||\vec{u} - \vec{u}_{measured}||_P^2 + ||f(\vec{u})||_A^2 \tag{2.20}$$

where $||\vec{x}||_Q^2$ denotes $\vec{x}^T Q \vec{x}$ and $f(\vec{u})$ are cellular forces, which are assumed to exist everywhere inside the considered volume. The diagonal matrix P has a value of 1 if the displacement of the corresponding point is known and a value of 0 if the information about the local displacement is missing (or the corresponding node is outside the region of interest). The matrix A is a diagonal matrix containing the local penalty weights for a force vector. The Matrix $A = I$ is identical to that found in the Tikhonov regularization method. Larger nodal forces have smaller penalty coefficients. In addition, a zero-penalty weight was added in the matrix A (for force points with a distance to the cell surface of less than half the mesh size) and $L(\vec{u})$ was minimized using the conjugate gradient method [79].

The force reconstruction method consists in finding the simulated force field, which matches best the experimental one. This can be done by shifting the location of the force application in the simulation and/or by adjusting the magnitude and direction of the force. The typical accuracy of this method is 5 nN, and its spatial resolution around 30 μm.

2.3.3 Fourier transform traction cytometry (FTTC)

Butler first propose to perform the regularization process in Fourier space [80]. One can indeed solve the inverse problem in Fourier space (using Fourier transforms on both sides of the equations 2.6). This greatly reduce computation time as the Fourier transform of a convolution is the pointwise product of Fourier transforms :

$$\tilde{\vec{u}}(\vec{k}) = \tilde{G}(\vec{k})\tilde{\vec{F}}(\vec{k}) \tag{2.21}$$

where $\vec{k}$ is a wave vector, and the tilde symbol denotes a Fourier transform. The force vector can be calculated using the inverse Fourier transform :

$$\tilde{\vec{F}}(\vec{k}) = \tilde{G}^{-1}(\vec{k})\tilde{\vec{u}}(\vec{k}) \tag{2.22}$$

Recently, the FTTC has been used to calculate 2D force fields. Assuming that the displacement and force fields are discrete quantities, $\tilde{G}(\vec{k})$ reads :

$$\tilde{G}(\vec{k}) = \frac{2(1+\nu)}{Ek^3} \begin{pmatrix} (1-\nu)k^2 + \nu k_y{}^2 & \nu k_x k_y \\ \nu k_x k_y & (1-\nu)k^2 + \nu k_x{}^2 \end{pmatrix} \tag{2.23}$$

Using Tikhonov regularization [5], we have (Eq. 2.22) [81] :

$$\tilde{\vec{F}} = (\tilde{G}^T \tilde{G} + \lambda^2)^{-1} \tilde{G}^T \tilde{\vec{u}} \tag{2.24}$$

Note that this FTTC requires (i) to interpolate the experimentally measured points on a given grid (which introduces additional errors) and (ii) to set the traction filed to zero outside the cell boundaries (therefore, the location of the cell has to be precisely known) [82].

2.3.4   Improvements of FTTC

Michel *et al.* have applied the FTTC technique on a real case (using a regularization technique and setting the stress filed to zero outside the cell) [80]. Their procedure, which uses an iterative approach [6], works as follows :

1. Calculate the force field as in classical FTTC without constraints

2. Define a new force field by adding zero forces outside the cell boundary

3. Calculate the displacement field, introduced by this force field (direct problem)

4. Define a new displacement field by replacing the experimentally observed displacements (within the cell boundary) by the displacements of the calculated displacement field within the cell boundary.

5. Repeat steps 1-4 until the solution converges (within some level of tolerance).

Del Alamo *et al.* [63] have proposed an approach, which allows to calculate the 3D stress field in Fourier space. The 3D displacement field is computing by solving the elasticity equation of equilibrium for a linear homogeneous body :

$$(1 - 2\sigma) \, \bigtriangledown^2 \vec{u} + \bigtriangledown(\bigtriangledown\vec{u}) = 0 \tag{2.25}$$

---

5. Instead of using a regularization scheme, one can filter noise by removing high frequencies in Fourier space.

6. An iterative computation requires a large CPU time. Still, this approach was found to be faster than using a regularization in real space. Also note that FTTC allows to easily implement different smoothing procedures or filters in the Fourier space (Wiener or Gaussian filters [78]).
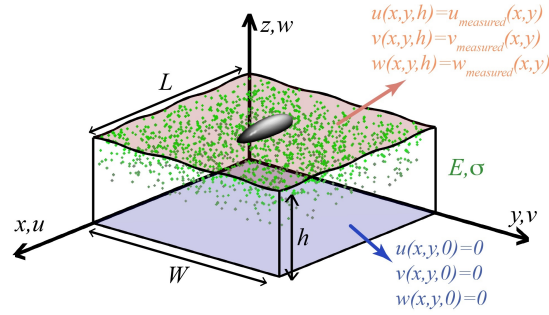
FIGURE 2.7: The output data of an experiment are the input data in equation 2.25. Adapted from [63]

where σ is the Poissson ratio of the body. The solution of Eq. 2.25 is considered to be periodic in both directions and so is expressed in terms of a Fourier series. Del Alamo *et al.* propose to input the measured the 3D displacement fields into an exact analytical solution of the elastic equilibrium equation :

$$\vec{u}(x, y, h) = \vec{u}_{measured}(x, y) \qquad (2.26)$$

$$\vec{u}(x, y, 0) = 0 \qquad (2.27)$$

where h denotes the substrate height. The last equation (Eq. 2.27) states that the deformation field is zero at the bottom surface (which is the normally the case as the substrate is in contact with a glass slide (Fig 2.7)). Note finally that the stress vectors could be obtained by applying Hooke's law in Fourier space. An important point is that this approach does not assume infinitely thick substrates (in contrast to model with semi-infinite medium), so thin substrates could be also used.

Chapter 3

The setup

3.1 Building the setup

3.1.1 Introduction

When cells adhere on a thin substrate, Del Alamo *et al.* have shown that "their out-of-plane traction stresses can reach four times deeper into the substratum than their in-plane traction stresses" [63]. Measuring the displacement field along the z direction is therefore of importance. Previous studies (using fluorescent bead reporters) have failed to precisely estimate the displacements along z (the accuracy in the x and y was several times better). Moreover, the use of fluorescent reporters has two disadvantages : such beads can be toxic for the cells and a significant bleaching could be observed in long-term experiments (lasting ten hours or more).

To circumvent these problems (low accuracy along z, toxicity, bleaching), we propose to use non-fluorescent beads and apply algorithms, which can detect sub-nm displacements of micron-sized beads (see below).

The x, y and z positions of the beads could be estimated from the interference pattern between the forward-scattered and the unscattered (non-fluorescent) lights (Fig. 3.1a) [1]. This method (Digital Holographic Microscopy, DHM) has been first used by Croquette and Gosse [83, 84] in magnetic tweezers. Both the x and y positions of a centrosymmetric object (bead) can be determined using a cross-correlation algorithm and the z position can be estimated from the averaged radial intensity profile of the bead image. This intensity profile is then compared to previously acquired radial profiles at different z positions (e.g. by moving the objective lens in 100 nanometer steps) (Fig. 3.1b,c). These profiles are

---

1. The diffraction rings are observed on distances of a few microns only (the light coherence, $\lambda^2/\Delta\lambda$). In our case, the value is about 5 to 6 microns.

stored in a Look Up Table (LUT), which can be interpolated to reach sub-step (nm) accuracy [2]

In principle, the hologram patterns could be fitted by Lorenz - Mie theory [86]. A hologram H contains both intensity and phase information :

$$H =\mid E_0 + E_{sc} \mid^2 = \mid E_0 \mid^2 + E_0^* E_{sc} + E_0 E_{sc}^* + \mid E_{sc} \mid^2 \tag{3.1}$$

where (E_0) and E_{sc} denotes the unscattered (initial) and scattered fields, respectively. The background intensity should be also taken into account. Therefore, the normalized histogram reads :

$$h = \frac{H}{\mid E_{sc} \mid^2} = 1 + \frac{E_{sc}}{E_0} + \frac{E_{sc}^*}{E_0^*} + \left| \frac{E_{sc}}{E_0} \right|^2 \tag{3.2}$$

where $\mid E_0 \mid^2$ denotes the initial wave intensity.

Here, h is determined from the Lorenz-Mie scattering function and depends on (i) the position and radius of the particle and (ii) the particle and medium indexes.

Knowing the shape and the refractive index of beads, once could compute a theoretical LUT without having to acquire experimental images [3]. Because a small error in the estimation of the parameters (e.g. radius, refractive index) would greatly change H, this approach is not used experimentally.

3.1.2   The setup construction

The setup (Fig.3.3) has two functions :
– Measuring the displacement field of single beads in bright field
– Obtaining the cell position using fluorescent microscopy

To regulate the setup at 37°, we use a *PECON TempController 2000-2* and have placed the custom-build microscope in a enclosure system (a plastic box, 1 in Fig. 3.3). CO_2 is delivered inside a small container (placed on top of the flow chamber, 3) and its level (5%) is controlled with a *PECON CO_2 controller 2000* device. To minimize temperature gradients (the optical table acts as a thermal reservoir), the plate (stainless steel) that holds the flow-cell rests on four ceramic legs. To precisely correct movements (thermal drift, vibrations), we use beads (acting as fiducial markers) that are melted on the glass

---

2. Using the same technique and fast CMOS camera (which allow to average a large number of images), Huhle *et al.* [109] have successfully resolved 0.3 nm-sized steps (at 10 Hz) on fixed micron-sized beads.

3. Even so the calculation of (3.2) is CPU demanding (for bead clusters, this is even worth [87]), the calculations need to be performed only once.
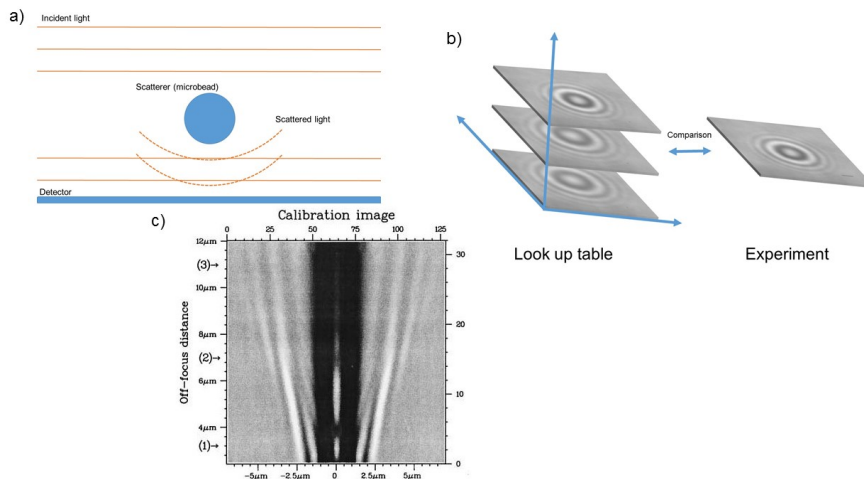

FIGURE 3.1: Figure (a) : schematic illustration of in-line digital holographic microscopy. An incident plane wave illuminates an object and a detector records the interference pattern formed by the scattered and incident lights. Figure (b) : principle of the z-position measurement. At each frame, the current bead image is compared to the set of calibration images (LUT, see text). Figure (c) : a set of calibration images measured for a 1 μm diameter bead melted on a glass surface. Each line is obtained by measuring the radial profile of the object at a given z position of the microscope objective. Adapted from [83]

coverslip (3.2).

The light source, a bandpass filter, an iris and lenses are mounted in a lens tube system (2). The light source is a broadband Light Emitting Diode (470 - 850 nm, *THORLABS MBB1D1*). An additional band pass filter (*SEMROCK FF01-697/75-25-D*, Fig. 3.4, left) allows to set the coherence length to a value of about 5 μm [4].

An oil-immersion objective lens (*ZEISS N-Archoplan*, 100X, NA 1.25) is used to image the specimen, *i.e.* the gel deposited on a 35 mm Glass Bottomed Cell Culture Dish (POR-VAIR) (see figure 3.4, right). The objective is mounted on a P-721 PIFOC piezo flexure objective scanner (closed-loop travel of 100 μm) that has a closed-loop resolution of 0.7 nm.

Holograms are imaged onto a CCD camera (*BASLER acA1540-25gm*, 8). In addition, a dichroic mirror (*SEMROCK FF655-DI01-25X36*, 1) is used for fluorescence imaging. Here, a second dichroic mirror (*SEMROCK FF497-DI01-25X36* , 2) separates the fluorescence excitation (488 nm) and emission. The characteristics of both mirrors is shown in Fig.

---

4. A modulated LASER diode (to reduce speckles) or a Super-luminiscent Laser Diode (SLD) perform best in terms of image quality (diffraction patterns) and allow to reach high acquisition bandwidths (la few kHz) (DULIN PLOS ONE 2014). Due to their high coherence (a typical SLD has a coherence length of about 40 μm, there is a limit in the density of beads (otherwise diffraction patterns would superimpose).
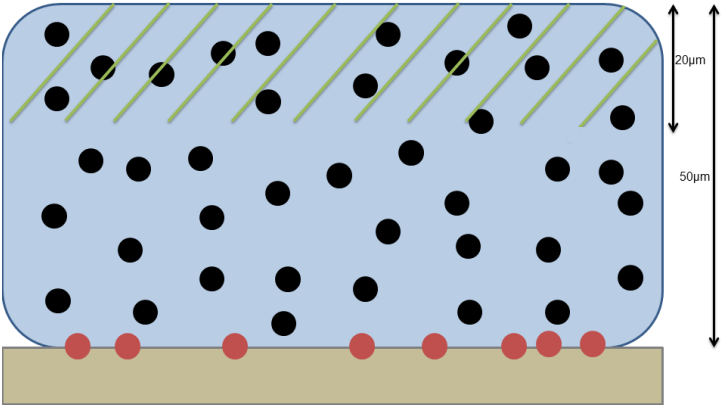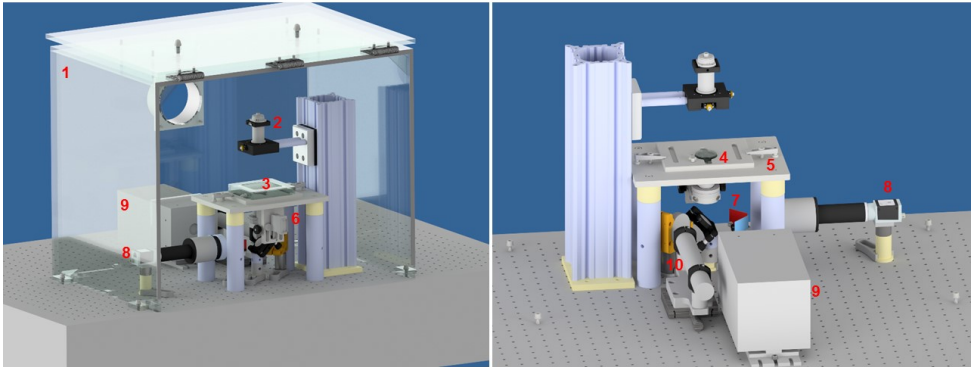
FIGURE 3.2: Schematic picture of the gel with embedded beads. The typical height of the gel is 50 to 70 μm, the region used for tracking is about 20 μm^2 (green overlay), reference beads are melted on the glass slide of the petri dish (red circles).

a)   b)
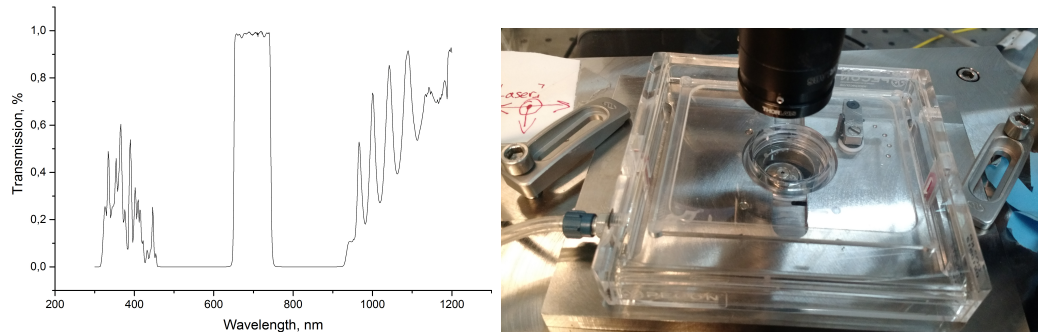
FIGURE 3.3: The setup from different perspectives (a,b).

FIGURE 3.4: Left : light transmission coefficient as a function of the wavelength of the *SEMROCK FF01-697/75-25-D* bandpass filter. Adapted from https ://www.semrock.com. Right : Petri dish mounted on its plate holder. Also shown is a small enclosure system, which is used to maintain a proper level of CO_2.
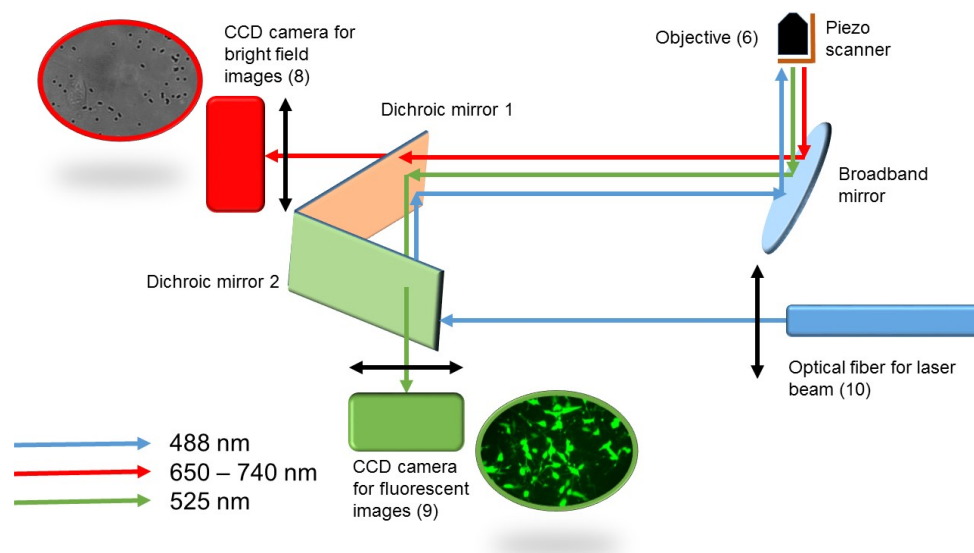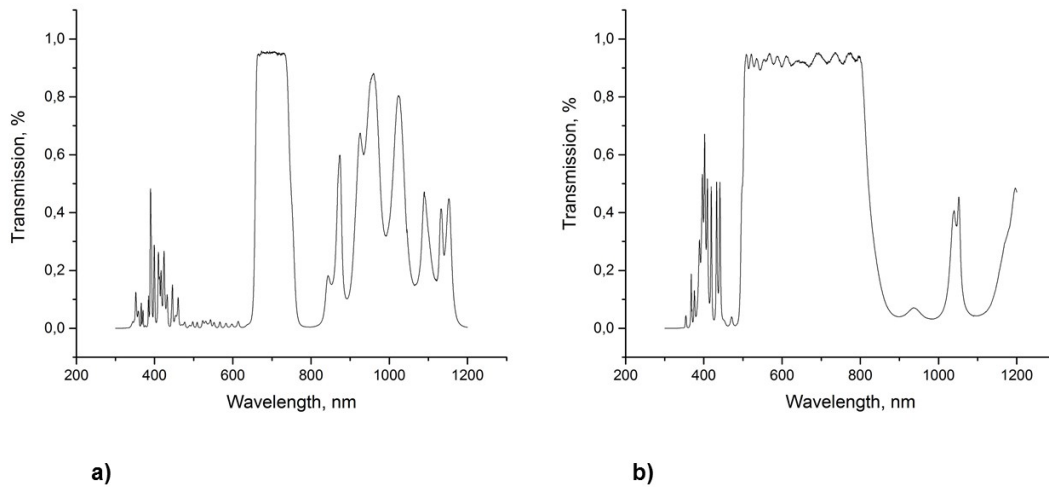

FIGURE 3.5: Setup : imaging

FIGURE 3.6: Light transmission coefficient as a function of the wavelength of both dichroic mirrors Adapted from https ://www.semrock.com.

3.6a ; the fluorescence is imaged on a PhotonMax intensified camera. Notice that the LASER beam is focused on the back aperture of the microscope to illuminate a large area $(200~\mu m^2)$.

In summary, the device produces two different images :

– The non-fluorescent image of the beads. Diffraction patterns allow to determine the x, y, z positions of the beads. Note that filopodia are not properly resolved on this image (obtained in transmission).

– The fluorescent image of the cell (transfected with $p^{CAG} - LifeAct - TagGFP2$). This allows to precisely determine the position and the shape of the cell. Note that a phase-contrast (non-fluorescent) image is not able to determine precisely borders of thin filopodia. In the future, fluorescent excitation (two colors) could be used to image specific parts of the cell (e.g. actin filaments).

3.2   Finding position with sub-pixel accuracy

Part of my thesis has consisted in writing a Labview software. The software allows to acquire images, building a Look Up Table (measuring radial profiles at different z positions of the bead, e.g. by moving the objective lens) and determining the x, y and z
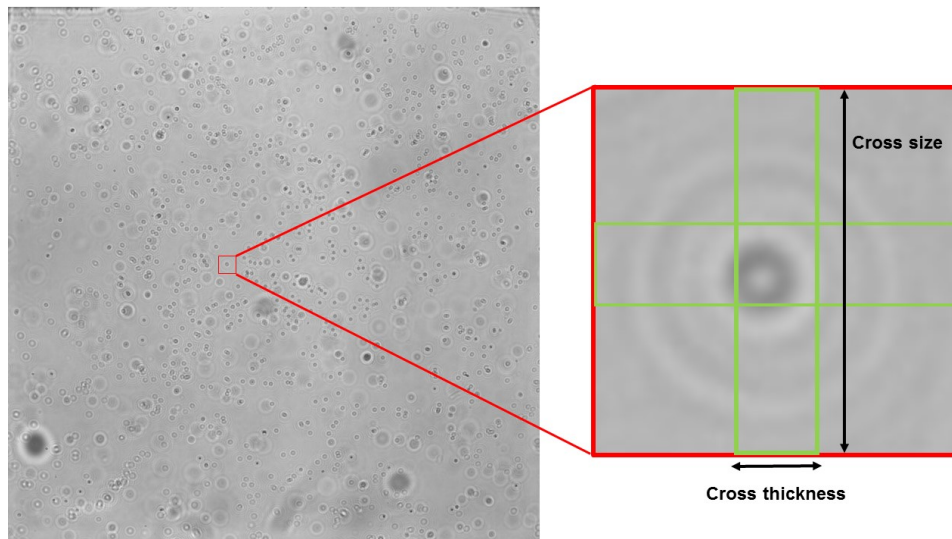
FIGURE 3.7: Shown here is a field of view (approximately 200x200 μm^2) where we manually choose the x_0, y_0 positions of the beads.
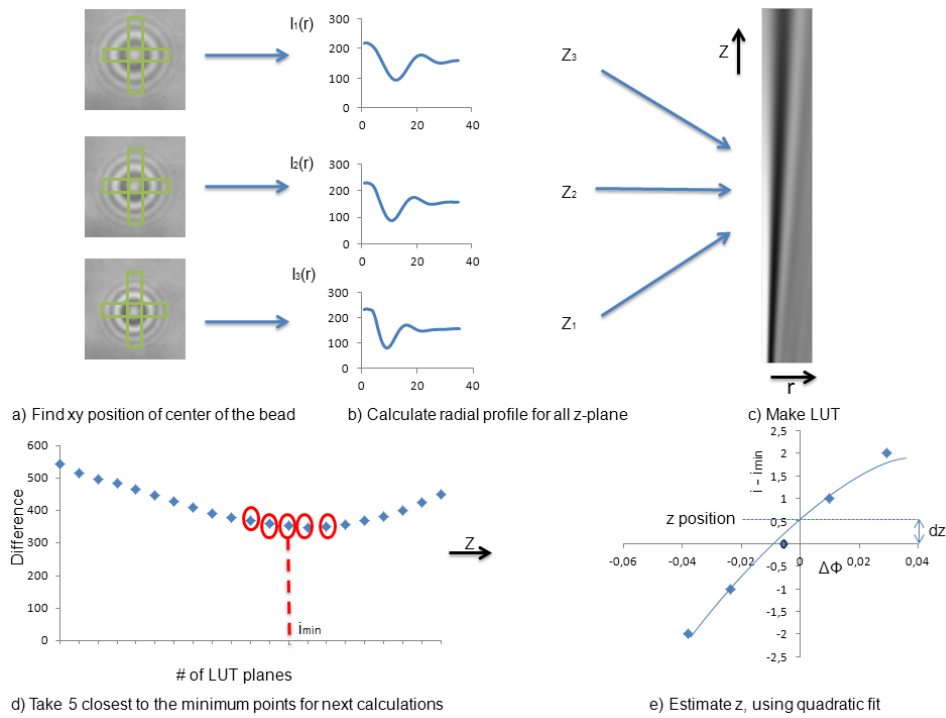
positions of the beads at each time step $\vec{r}(i_b, t)$, $i_b = \overline{1 : n_b}$[5]. Tracking the beads is done offline using an approach developed by V. Croquette (ENS, Paris) [83, 84].

3.2.1   x and y positions

Let us consider an experimental image (Fig. 3.7). The x and y positions of the bead are determined as follows :

– Estimating the center position of the bead : x_0, y_0.
– Finding all pixels $P(i, j)$ located inside two perpendicular rectangles (for both the x and y directions). These two rectangles have an equal length (cross-size) and an equal width (cross-thickness). In our case (pixel size of 110 nm), typical values are 70 px and 6 px for the cross-size and cross-thickness, respectively.
– Averaging pixels along the rectangle's width : $p(i) = \frac{1}{crossthicknes} \sum_{j=1}^{crossthickness} P(i, j)$.
– Mirroring the previously obtained 1D profiles ($p'(i) = p(crosssize - i)$) and calculating the normalized cross-correlation $C_{pp'}$.
– Finding the maximum of $C_{pp'}$ using a 5-points polynomial fit. From this maximum, one can determine the center positions of a centro-symmetric object with sub-pixel accuracy.

---

5. As previously written, we also determine the positions of reference beads melted on the glass surface.

a) Find xy position of center of the bead   b) Calculate radial profile for all z-plane   c) Make LUT

d) Take 5 closest to the minimum points for next calculations   e) Estimate z, using quadratic fit

FIGURE 3.8: Finding the z position of the bead (see text).

3.2.2   z position

The z position of the bead is determined as follows :

1. Calculating the radial profiles using the x and y center positions of the beads (Fig. 3.8a). The radial profile is a projected vector that represents the average intensity of all pixels in a constant distance to the center. Zhang and Menq [85] have proposed a straightforward determination of this quantity.

2. Finding the z position using a library of radial profiles (LUT). As written previously, a LUT is built (for each bead) at the beginning of the experiment (Fig. 3.8c). For all experiments shown in this work, the LUT step-size is 50 nm (the difference in bead position). To determine the z position of the bead in the LUT, we first compute the squared difference :

$$d_i^2 = \sum_{r=1}^{l}(I_i(r) - I_{tr}(r))^2 \tag{3.3}$$

and determine its minimum (Fig. 3.8d), from which we store five radial profiles : $I_{i-2}(r), I_{i-1}(r), I_i(r), I_{i+1}(r), I_{i+2}(r)$.

3. Calculating the phase difference

In principle, a polynomial fit would be sufficient to determine the local minimum. Because the LUT has been obtained for specific (discrete) values, significant discretization errors could arise when the position has to be determined with a high accuracy. To circumvent this problem, Croquette introduces a parameter (the phase), which has a known (polynomial) dependence with respect to the position [84]. The phase can be obtained by applying a Hilbert transform to the radial profile and its derivative reads :

$$\Delta\Phi_k = \Phi_k - \Phi_{tr} = \frac{\sum_{j=1}^{l} \rho_j \rho_{tr}(\phi_j - \phi_{tr})}{\sum_{j=1}^{l} \rho_j \rho_{tr}}, \tag{3.4}$$

where $k = i - 2, i - 1, i, i + 1, i + 2$ and where the radial profiles are expressed in polar coordinates ($\{z_j = \rho_j e^{i\phi_j}\}$, $j = \overline{1 : l}$)

4. Estimating the z position

   Finally, the exact z position is obtained by fitting the previously measured phases with a quadratic function (Fig 3.8e).

3.2.3 Criteria

When the noise is large, we sometimes obtain outliers. We therefore have implemented two additional criteria. The first criterion consists of determining the following quantity : $\xi^2 = \sum_{i=1}^{5}(n_{calc}(i) - i)^2$, which represents a goodness of a fit. We empirically have found that this value should not be more than 1. The second criterion (z criterion) states that the determined z position cannot be too far from the local minimum (e.g. more than one δz) (Fig. 3.8e).

To show the usefulness of criteria, we have made the following experiment : we have built a LUT using a step size of 25 nm (800 frames). From this LUT, we have built two LUT : the first contains radial profiles obtained at positions $2(i + 1)$, the second contains radial profiles obtained at $2i + 1$ ($i = 0 : 399$). The first LUT is used as a library to determine the "unkwown" locations of the radial profiles measured at $2i + 1$. If the found position is located no further than half the step size from the true position (that we know), we mark it as "T" ; if not, we mark it as "F". If the position satisfies both criteria ($\mid dz \mid < 1$ and $\xi^2 < 1$), we mark it as "t" ; if not (at least one criterion is not satisfied), we mark it with "f". For instance, one position can be correct (so actually be quite close to its real position) but will not satisfy one of the two criteria. Then, this position will be marked as "Tf". We have performed measurements on 20 beads. Results are shown in table 3.1.

T	t	0.835394737
T	f	0.063684211
F	t	0.012894737
F	f	0.088026316

TABLE 3.1: Percentage of the positions, which (i) are correct and satisfy both criteria (Tt) (ii) are correct but do not satisfy both criteria (Tf) (iii) are not correct but satisfy both criteria (Ft) and (iv) re not correct and do not satisfy both criteria (Ft)

As we can see (table 3.1) the percentage of correct data without applying the criteria is $83.5\% + 6.3\% = 89.8\%$. After applying filters, based on criteria, we will have $83.5\% + 1.2\% = 85\%$ of the total number of positions. But percentage of correct data in this case will be : $83.5/84.7 * 100\% \approx 98.6\%$. So, using χ and z criteria, one can decrease percentage of wrong data about 10%.

3.3 Characterization of the setup

In this section, we characterize the setup and determine relevant parameters such as the precision in the x, y, z positions , the influence and the amplitude of the thermal drift and the optimal bead concentration.

3.3.1 Accuracy of typical experiments

We present here a test experiment (same conditions as a TFM experiment with the difference that we do not seed cells on the gel surface) in which we acquire one image every 1 minute at the frequency 20 Hz. Fig. 3.9 shows the measurement for one bead (embedded in the gel) during the course of the experiment (10 hours). The drift is hundreds of nm in the xy plane and a few microns in the z direction.

As written previously, we can compensate for the drift by monitoring the positions of fiducial markers (reference beads, melted on the glass surface). Fig. 3.10 shows the result of this measurement. Standard deviation (of differences) are : 12 nm for x, 9 nm for y and 32 nm for z, respectively. experiment.

3.3.2 Quantifying tracking errors

The Allan variance ($\sigma_y^2(\tau)$, or Allan deviation $\sigma_y(\tau)$) is a measure of frequency stability in clocks, oscillators and amplifiers [89]. As shown in [96], [97], the Allan variance is a
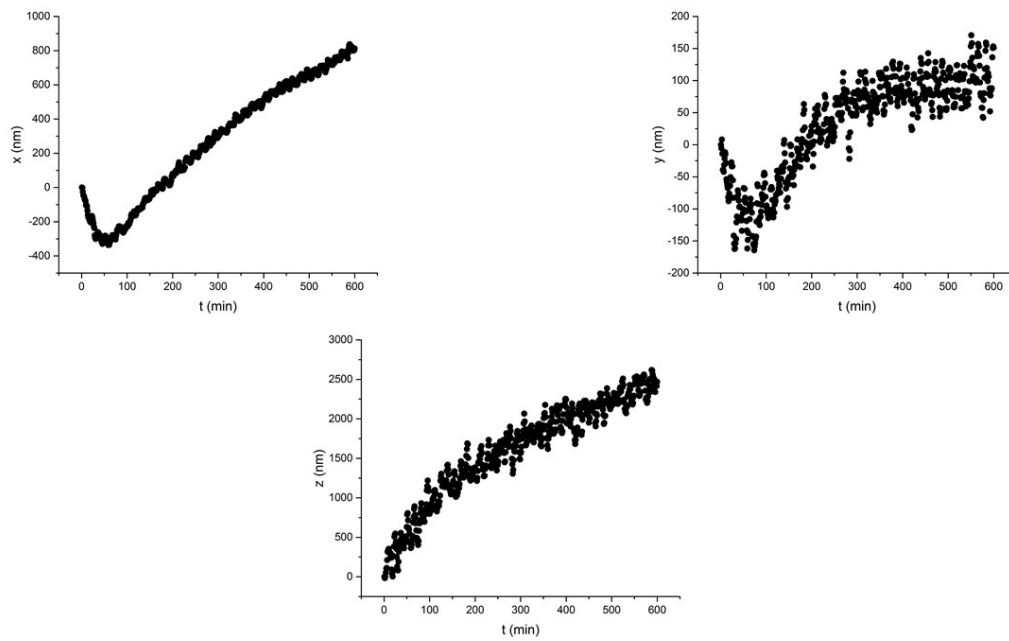
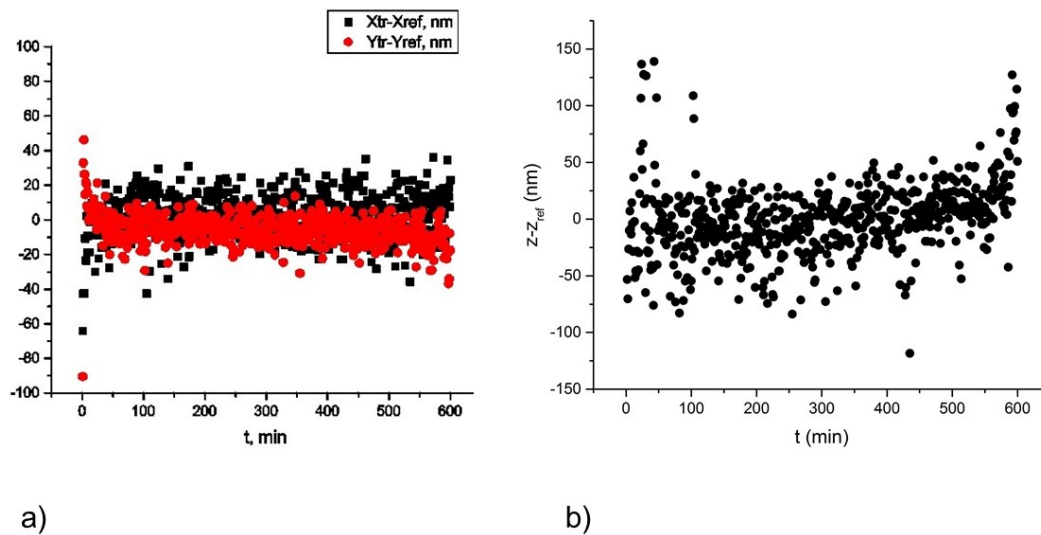FIGURE 3.9: Motion of the bead during 10 hours for the x, y and z directions.

FIGURE 3.10: The difference in motion between the beads (5 beads, 600 positions per bead) attached at the bottom of the petri dish (reference beads) and beads located near the surface of the gel surface. Figure (a) and (b) shows the (x,y) and z component, respectively.

reliable quantity that can characterize the noise of sensitive instruments (e.g. magnetic or optical tweezers) [89].

$$\sigma_y^2(\tau) = \frac{\sum_{i=1}^{N-2n}(\overline{y}_{i+n}(n,\tau) - \overline{y}_i(n,\tau))^2}{2(N-2n)} = \frac{\sum_{i=1}^{N-2n}(y_{i+2n} - 2y_{i+n} + y_i)^2}{2(N-2n)\tau^2} \qquad (3.5)$$

where $\tau = n\tau_0$ ($n < (N-1)/2$, $1/\tau_0$ is the sampling frequency) and N is the number of samples. The Allan variance thus measures the noise level when averaging over a given bandwidth. A log-log plot of the Allan deviation as a function of τ allows different noise types to be distinguished. For instance, a white noise (uncorrelated noise) has slope of -1/2 (*i.e.* averaging uncorrelated noise reduces noise), drift a slope of +1 and a "bump" is the signature of acoustic or vibration (uncorrelated noise) .

In Fig. 3.11, we present the result of such a noise analysis on melted beads (5000 images were measured at 20 Hz). As expected, the Allan deviation (log-log plot) has a $\tau^{-1/2}$ at low τ. At higher τ, the noise increases due to drift, which can be suppressed by subtracting the position of a reference bead. It is interesting to mention some typical features : for instance, we observe an increase in the noise for a value of τ of about 0.1 (we recently have found that this originates from an air conditioning unit located next room).

As shown in Fig. 3.11, the Allan deviance shows a minimum, which we have used to characterize the noise of the instrument. For instance, we can easily deduce the optimal z tracking plane (Fig. 3.12) [6].

Here, we have calculated and averaged the position for each image. For 20 images (acquired at 20 Hz), this yields a noise level of 2 nm in the xy plane and 2.5 nm along the z direction ($d = 2 - 6$ μm), respectively. Averaging a larger number of images (acquiring at an higher frequency f_h and averaging over the same bandwidth) would improve the noise level by a factor $\sqrt{f_h/20}$. At the moment, the procedure we use is different for every bead : we acquire 20 images and then calculate the position on the averaged image. We repeat this procedure at four different planes (see below).

We apply the procedure of the frames averaging in order to remove noise, that comes from light intensity oscilations and problems with data transmission from CCD to computer. Number of images for averaging was chosen empirically and it has no connection to the optimal number of images, that should be saved every time step (subsection 3.3.2). In order to obtain relevant for our experiments conditions we plot Allan deviation for bead

---

6. In agreement with previous studies, we have found that the accuracy in x and y does not depend on the tracking plane [90]. Due to drift, the z position varies and so one could feedback to maintain an optimal and constant tracking plane.
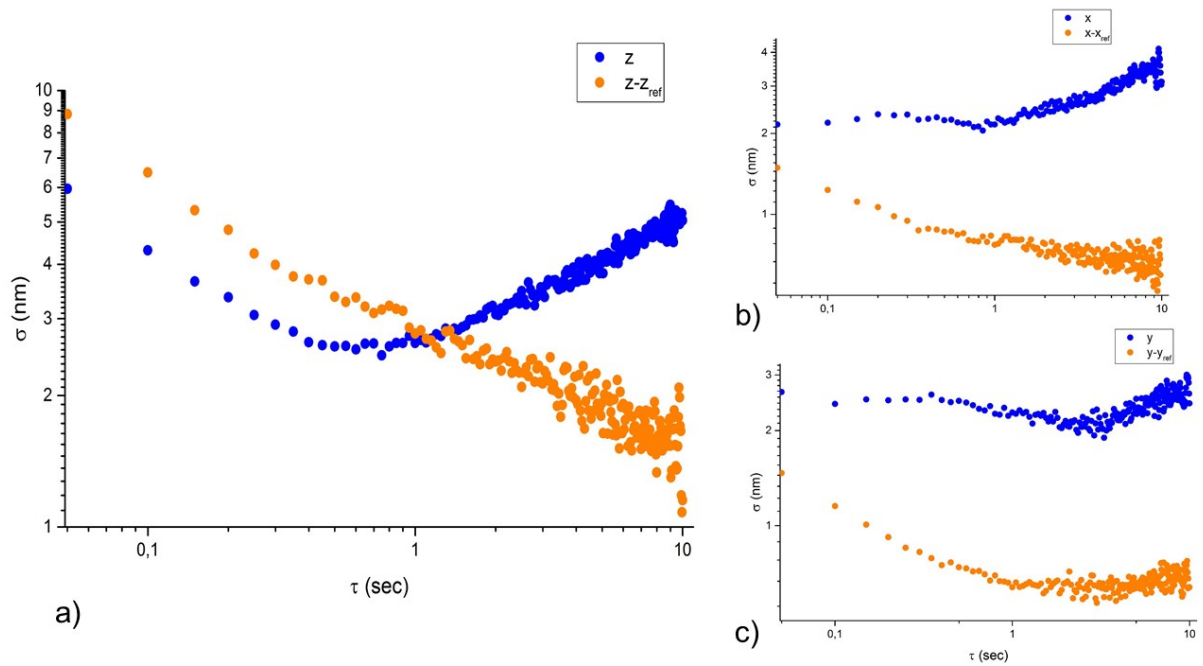

FIGURE 3.11: The Allan deviation versus τ (log-log plot) measured for a bead melted on the surface with 0.9 μm dimater (blue curve). Shown are the results for the x (b), y (c) and z (a) directions, respectively. When subtracting the position of a reference bead, drift is virtually eliminated.
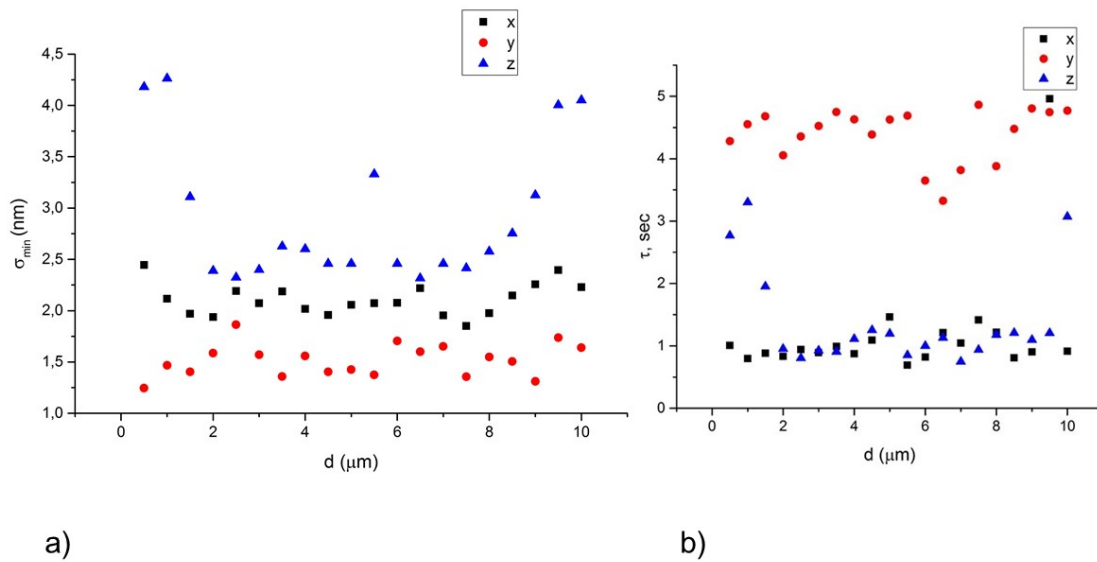

FIGURE 3.12: a. Position accuracy measured at different focal planes (d denotes the distance between the bead focus and the tracking plane). b. The τ value at which we obtain the best measurement accuracy.

positions, calculated from images averaged over some number of images (M). We used three values for M : 10, 20, 30 averaged frames. Results are shown on figure 3.13.

Images were acquired at the same frame rate - 20 Hz, so values of τ_0 are different : $\tau_0 = 0.5$ sec for $M = 10$, $\tau_0 = 1$ sec for $M = 20$, $\tau_0 = 1.5$ sec for $M = 30$. Values for observation time will be also different depending of number of the averaged images, but we vary τ up to 30 seconds for all three values of M.

Lets consider plot of Allan deviation for z component of the bead positions (figure 3.13a). σ_z decrease with τ except part of curve for $M = 10$ at high τ. It means that we could achieve higher precision by averaging big number of positons. σ_z could reach value 2 nm, but price for it is loss of the temporal resolution : $\tau = 30$ sec. With recent procedure of images acquiring we get value of Allan deviation about 13 nm (first point for data with $M = 20$).

Plots 3.13b and 3.13c represents x and y components respectively. Allan deviation for x and y directions has the same behavior but with smaller values. Accuracy, that we reach in our experiment is 3 nm in x and y directions. Here we could also increase precision simply by increase number of averaged positions. σ_{xy} can reach value 1 nm for $\tau = 30$ sec. The main difference between Allan deviation for xy plane and z direction is slope, that is much higher for z component. It means that efficiency of bead positions averaging procedure is bigger for z component than for x and y.

One can notice, that efficiency of averaging bead position is higher than averaging images itself. Allan deviation value for z component for averaging 20 bead positions is about 2.5 nm (figure 3.12a) for $d = 5$ μm. σ_z for averaging 20 images is 13 nm (figure 3.13a) for the same d. For x and y components difference is not so crucial : 2 nm in case of averaging bead positions versus 3 nm for image averaging.

We performed one more test experiment in order to check bead position stability. We acquired 200 images with beads for case of averaging 20 frames before one image record. Total time of experiment is 200 seconds - 20 averaged frames x 200 times at frequency 20 Hz. At this timescale drift will play role in bead position (timescale for drift is more than 5 seconds - figure 3.11). In order to remove drift part, we define accuracy of the bead position measurements as standart deviation of relative bead positions with respect to reference bead : $x - x_{ref}, y - y_{ref}, z - z_{ref}$.

We made measurements for 200 positions of 10 beads and we get next results : $\sigma_x = 4.32$ nm, $\sigma_y = 5.03$ nm, $\sigma_z = 12.28$ nm. These values are close to the values of Allan deviation ($\sigma_{xy} = 3$ nm, $\sigma_z = 13$ nm).
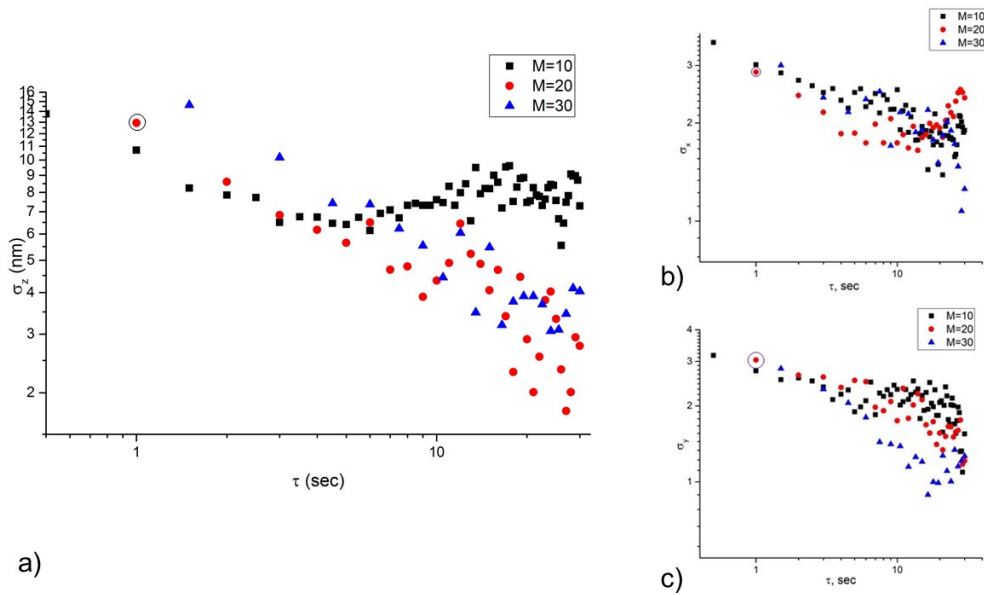
FIGURE 3.13: Allan deviation for z component of the bead position (figure a), x component (figure b) and y (figure c). Each image for the bead tracking procedure was averaged over M images. Black squares correspond to $M = 10$ frames, red circles to $M = 20$ and blue triangles to $M = 30$. Circled points represent values of Allan deviation for our experimental conditions. Distance between focal plane and bead position : $d = 5$ μm.

Tracking noise (using the above-mentioned routines) depends on shot noise [98] [7]. However, we have found that averaging images does not significantly improve the noise level, which means that there is not a simple linear relation between tracking noise and shot noise. Because we perform on offline analysis, it seems difficult to store a large amount of images (which would be necessary if ones would acquire at high frequencies, e.g. few hundred Hz). In contrast, analyzing the images in real time would require special parallel architecture (e.g. CUDA), which is not yet implemented in the software.

3.3.3 The bead concentration

For getting displacement field precisely as much as possible, we should have large number of tracking beads. But the total number of beads is limited by a size of the bead itself and size of the tracking cone. So, for example, we could not track two beads at the same xy position (or close positions) but different z positions, if difference in z position is less than height of the tracking cone (figure 3.14) .

We measured the approximate size of "trackable" and "non-trackable" cones (figure

---

7. Shot noise is gain dependent (higher gains result in lower Signal to Noise ratio) and dominates quantization noise for 8 bits camera having a large well depth.
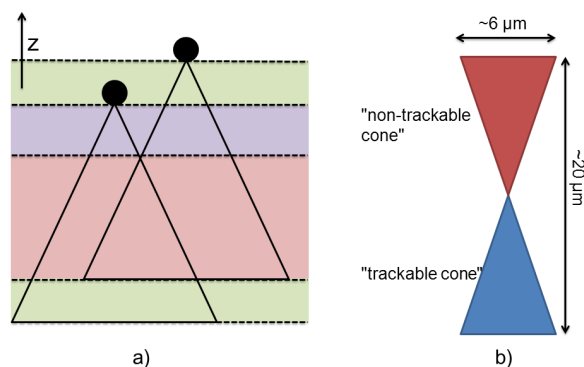
FIGURE 3.14: Figure (a) : schematic representation of tracking cones of two beads. Green regions correspond to z positions where we can track one bead, violet region - is zone, where we can track both beads, in red region we could not track any beads, because the cones overlap. Figure (b) : schematic representation of "tracking cone" - interference rings, which one can see below the real bead position of the bead and it possible to use them for tracking process, and "non-tracking cone" - some pattern, that does not have any certain shape, so it is not possible track bead with this pattern.

3.14b) for rough estimation of maximum bead concentration in the gel. Per each bead we have two cones with heights 10 μm and radius 6 μm. It means that maximum volume concentration, that we can have without cone intersection for bead with 1 μm diameter will be : $c_{max} = \frac{1/6\pi 1^3 \mu m^3}{2/3\pi 6^2 \mu m^2 10 \mu m} \approx 0.0007 = 0.07\%$. But it is, of course, for ideal case, if any cones do not intersect. In real experiment it is impossile completely avoid this phenomena.

The same bead we can track successfully in one plane, but have difficulties with tracking on another plane (figure 3.14a). It's mean, that during tracking we should take few different planes in order to increase the probability find successfully z position of the bead.

Due to this fact, the next topic for discussion will be an optimal concentration of the beads with certain size. For this task we perform the same type of experiment as in section 3.1, so we know exactly the position of all beads for each track image. For a given concentration of beads we have set of tracking planes, whose number we will change (from 4 to 400). We assume, that the bead is "trackable" if exist at least one position (one plane), where the difference between calculated and real z position of the bead will be less than one Δz step in LUT. The number of successfully tracked beads in the field of view of 175x175x20 μm, as a function of number of track planes and concentration of the beads, embedded in a gel shown on figure (figure 3.15).

Of course, during experiment it is not possible to take each time 400 planes for tracking, because it takes time and memory on the disc. So, from the plot we see, that if we take 8
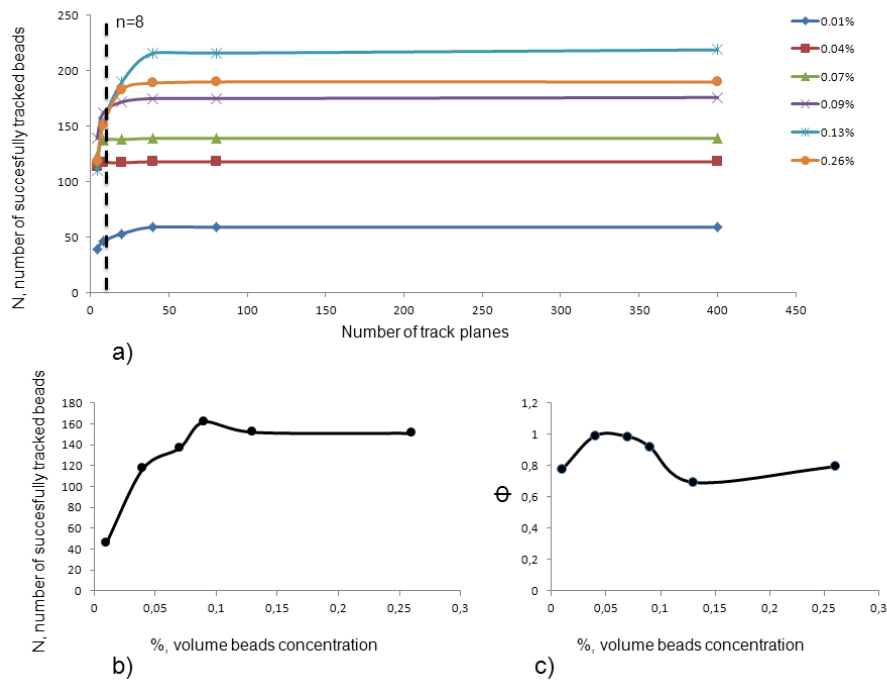
FIGURE 3.15: Figure (a) : number of successfully tracked beads as a function of number of track planes for gels with different bead concentrations. Figure (b) : number of successfully tracked beads as a function of the bead concentrations inside the gel. Figure (c) : fraction of the succesfully tracked beads : $\Phi = \frac{N_{suc}}{N_{tot}}$ from the total number of tracked beads as a function of the bead concentration. Number of tracked planes for plots (b) and (c) is 8.

planes (that is reasonable value in terms of our experimental conditions), we lose about 1-20 % of the total number of successfully tracked beads (firgure 3.15c). The maximal value of those planes number is 162, that correspond to the gel with volume beads concentrations 0.13%. For gels with larger beads concentration we track less number of beads due to often overlaping of tracking cones of the beads and due to loosing contrast of image (as a result, the number of pattern rings is decreasing).

Finally, we can determine optimal volume beads concentration : it is around 0.1% , that is a bit larger than the value, calculated before : (0.07%).

Chapter 4

The software for the experimental data analysis

We have described the typical experimental procedure to use our setup. The beads positions are calculated by a method adapted from Croquette [84]. At this stage, we know the beads positions at all time steps during the experiment. In this chapter, we develop how the traction force field is obtained from the markers positions. The theoretical description of the force field derivation has been described in section 2.3. Here, we detail the our implementation and, by making simple simulations, will determine the precision of the computed stress field. All routines for the analysis of experimental data are written in *MatLab*.

4.1 The field of deformations

4.1.1 Beads positions relative to a reference frame

From the experiment we have xyz bead positions and values of ξ^2 and δz of each bead at each time step for a different planes. The information is stored in ASCII file formats with the *XYZCrPl* type of data. The lines correspond to the timesteps, the first three columns are x, y, z position of a given bead, the 4$^{\text{th}}$ column gives ξ^2 and the 5$^{\text{th}}$ column the δz value. The information relative to the next bead is stored in the following 5 columns and so on. If only one focal plane is tracked, the number of columns will be : $5 * n_b$, where n_b is the number of the beads. When several tracked planes are observed, the information about the successive tracking planes are stored in a series of columns. The total number of columns in this case will be : $5 * n_b * n_{pl}$, where n_{pl} is the total number of tracked planes
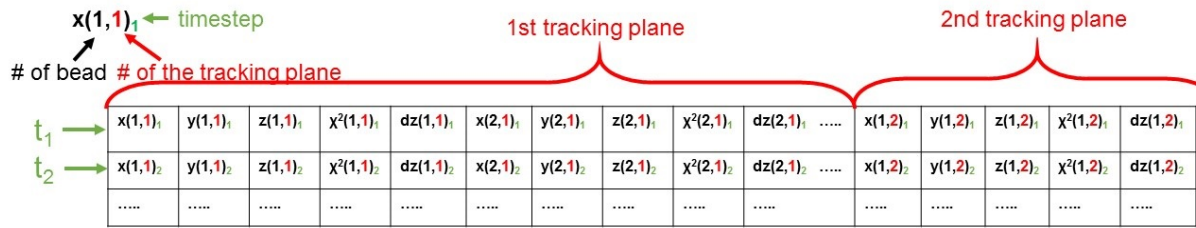
FIGURE 4.1: Scheme of data positioning in file type *XYZCrPl*

(figure 4.1).

This information we have for the track and the reference beads. First, we choose all reference beads, that have similar motion behaviour with few pixels precision : $<\vec{r}_{ref1}(t) - \vec{r}_{ref2}(t)> < \delta = 3\ px$. All reference beads, that pass this test, averaged in order to get resulting information about the drift. Averaging goes over all positions, which are passed criteria test ($|dz| < 1, \xi^2 < 1$). Finally we obtain a Tx3 vector, that represents the sample drift : $\vec{r}_{ref}(t)$, for t in range $1 : T$.

Then we work with the track beads. Usually, images are acquired at several positions of the focal plane in order to avoid loosing information when the position of a given bead at a given time step is not correctly measured, and in order to be able to average over redundent position information. First, the positions of beads over different focal planes are averaged. On the contrary, it may occur that, at time step t, the positions of the given bead from all planes could fail the criteria test. In this case, the position information of this bead at the timestep t is lost.

Then the drift motion is substracted from the total bead motion for every tracked bead : $\vec{r}_i^{res}(t) = \vec{r}_i(t) - \vec{r}_{ref}(t)$. At this stage, the positions of the beads for all experimental timesteps are obtained.

4.1.2 Computation of the deformation field

The best tip lies in the computation of the deformation field of the medium (equation 2.3). We thus need to determine the rest position of the tracked beads, when no mechanical forces are applied to the substrate. These positions are obtained at the beginning of the experiment, after loading the cells into the chamber but before they begin to deposit onto the substrate. Usually, during the first 25 minutes, cells do not deposit to the substrate, and we define the beads reference positions as the average of their positions over the first

FIGURE 4.2: Scheme of data positioning in file type *xyzt*. It is used to store displacement field data and position of points, where displacement field was measured.

10 time steps. The displacement field is then computed as :

$$\vec{u}_i(t) = \vec{r}_i(t) - \frac{1}{10}\sum_{j=1}^{10}\vec{r}_i(t_j) = \vec{r}_i(t) - \vec{r}_i(0) \tag{4.1}$$

where t is the time, i the number of the bead, $i = 1 : n_b(t)$, n_b being the total number of tracked beads at time step t.

The output of our software at this stage is the field of deformations $\vec{u}(t)$, where deformation field was measured $xyz(t)$. These data are stored in *xyzt* type (each column correspond to new t). As some beads are not successfully tracked at some time steps t, the number of tracked beads will differ from one time step to the other (but it will be never larger than n_b). As a consequence, the size of this matrix is $(3n_b; T)$, but some elements in the end of each column will be zero, indicating the absence of successfully tracked beads in this plane.

4.2   The force field

In order to find the force field we should solve Fredholm integral equation of the first kind at each time step (see part 2) :

$$\vec{u}(\vec{r}) = \int_{gel\,surf} d\vec{r}' G(r - r')\vec{F}(\vec{r}') \tag{4.2}$$

$\vec{u}(\vec{r})$ is a vector corresponding to the three-dimensional displacements of the beads : $(u_x(\vec{r_1}), u_y(\vec{r_1}), u_z(\vec{r_1}), u_x(\vec{r_2}), u_y(\vec{r_2}), u_z(\vec{r_2}), ...)$ whose size is $3n_b$, n_b being the number of tracked beads at time t. $\vec{F}$ is a vector field, computed at n_f chosen positions onto the gel surface. Its length is $3n_f$. In our experiment we assume that the upper surface of the gel is an infinite plane, and we further assume that the gel described as a semi-infinite medium [71], so that the Green function is given by the solution of the Boussinesq problem. The components of matrix G (whose size is $3n_b*3n_f$) are defined by the equation 2.4.

Finally, the equation 4.2 wan be rewritten as a set of linear equations :

$$\vec{u} = G\vec{F} \tag{4.3}$$

Generally it can be solved by the singular value decomposition, but this procedure, in our case, will not give reasonable results, due to the big value of the conditional number of G matrix. In our experiments, the conditional number is usually of the order of 1000. This means that problem is ill-posed and regularization procedure is needed (see section 2.3). Several strategies can be developed to solve this kind of problems, all of them require to add some information to the inout of the problem. We have developed an approcah based on *Tikhonov regularization* , where the following functional needs to be minimized :

$$f = (\mid G\vec{F} - \vec{u} \mid^2 + \lambda^2 \mid \vec{F} - \vec{F_0} \mid) \tag{4.4}$$

where $\vec{F_0}$ is the expected value of $\vec{F}$ and λ is regularization parameter. We will make the assumption that the force field is regular enough so that the expected value can be taken as $\vec{F_0} = 0$ [81].

The determination of the regularization parameter requires some information. In the absence of *a priori* knowledge about the force field, a balance must be chosen between too large λ values, leading to solutions strongly regularized, and biased towards the chosen $\vec{F_0}$ field, and too small λ values, where data noise is not regularized enough. When $\log \mid \vec{F} \mid^2$ is plotted as a function of $\log \mid G\vec{F} - \vec{u} \mid^2$, λ, being a parameter for the curve, in log-log representation, the curve exhibits a L-shape : it increases rapidly at low λ values and is essentially constant at large λ values. It may thus be considered that chosing λ value in between these two regimes is a good compromise between a strong regularization and an over-interpretation of the noise. We thus need to be able to find the λ value corresponding to the corner of this L-shape curve [73]. We will use the package developed and written by P.C.Hansen in Matlab (*Regularization Tools* , http ://www.netlib.org/).
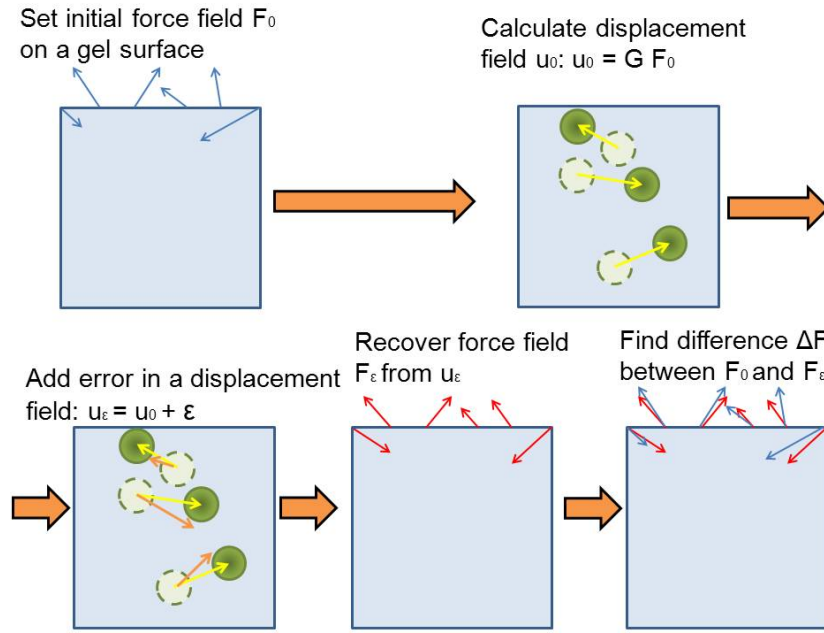
Ch. 4. The software for the experimental data analysis

FIGURE 4.3: Schematic illustrations of main steps of simulations.

4.3 Uncertainty of the force field

4.3.1 Introduction

In order to determine the minimal values of measured forces and its optimal spatial resolution, we simulated arbitrary forces applied at the surface of the substrate, applied our overall procedures and compared the computed force field to the original one.

The simulation proceeds according to the following steps (figure 4.3) :

1. chose an initial random force field at the surface of the gel : force vector $\vec{F}_0$.

2. compute the displacement field induced by this force field : the displacement vector $\vec{u}_0 = G\vec{F}_0$. The points at which the displacement field is computed are randomly distributed inside the substrate, simulating the random positions of the tracked beads.

3. add relative error to the displacement vector : $\vec{u}_\epsilon = \vec{u}_0 + \vec{\epsilon}$.

4. recover the force field, by by minimizing functional 4.4. The Tikhonov regularization process is applied and the L-curve criterion is used in order to determine the regularization parameter. At this stage we obtain the force vector $\vec{F}_\epsilon$.

5. compute the difference between the initial and the recovered force fields : $\Delta\vec{F} = \vec{F}_\epsilon - \vec{F}_0$.

The simulation are performed under the following conditions :

- the size of the elastic medium is 30x30x20 μm (correspond to the approximate area occupied by a single cell adhering to the substrate).
- the Young modulus of the elastic medium is 0.45 kPa and its Poisson ratio is 0.5.
- the initial positions of the beads (positions where the displacement field is defined) inside the medium are uniformly randomly chosen.
- the initial force field is random with normal distribution from -10 nN to +10 nN for each xyz component of the force vector. The average amplitude of one force vector is 10 nN.
- $\Delta \vec{F}$ is averaged over 100 similar experiments with different random positions of tracked beads and initial force fields.
- the difference between the initial force field and the recovered one is defined as :

$$< \Delta \vec{F}^2 > = \frac{1}{n_f} \sum_{i=1}^{n_f} \sum_{\alpha=x,y,z} (F_\alpha(r_i') - F_\alpha^{in}(r_i'))^2$$

$$\Delta \vec{F} = \sqrt{< \Delta \vec{F}^2 >}$$

$$(4.5)$$

4.3.2 Spatial resolution of the force field

The first question that we must answer is the number of points n_f where the force field should be calculated ("force points") for a given volume and number of tracked beads. This number will define the spatial resolution of the force field. All force points are situated at the surface of the gel ($z = 0$) and are arranged in a square mesh. We studied dependence of $\Delta \vec{F}$ as a function of the number of n_f and of the number of the beads n_b. In this simulation we didn't add any noise, so $\epsilon = 0$.

Figure 4.4 shows $\Delta \vec{F}$ exhibits a minimum as a function of n_f, whatever the chosen value for n_b. This corresponds to the optimal value of n_f. This minimum moves to higher values of n_f when n_b increase. It means that the spatial resolution of the force fied increases with beads concentration. Using the optimal bead concentration in the gel (see section 3.3.3), we are able to track $n_b \approx 30$ beads inside the region, and this value is chosen for the subsequent simulations. The minimum of $\Delta \vec{F}$ is obtained for $n_f \approx 25$, corresponding to a grid mesh with size equal to 6 μm.

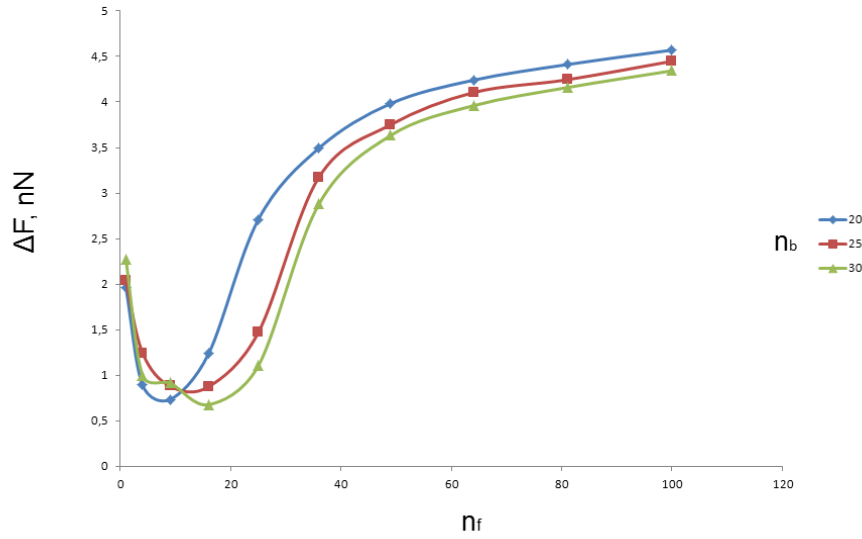These values will be used in all subsequent simulations : $n_b = 30$, $n_f = 25$.

FIGURE 4.4: Difference between the initial force field and the computed force field as a function of the number of force points n_f for different number of beads n_b, $n_b = 20$ (blue curve), $n_b = 25$ (red curve), and $n_b = 30$ (green curve).

4.3.3   Error in the force field calculation induced by the noise of the displacement field

Let us now compute the error of the force field as a function of the noise of the displacement field (figure 4.5, black points). The root mean square values of the noise is chosen in order to match the experimental noise. We have measured that it is ≈ 3 nm in x and y directions whereas it is ≈ 13 nm in the direction of the optical axis (see section 3.3). Thus, the simulations will be performed in the following conditions : $\varepsilon_x \approx \varepsilon_y = \varepsilon_{xy} \approx \frac{1}{4}\varepsilon_z$ and the noise root mean square values in the xy plane is varied from 0.5 to 10 nm. So that the noise in the z direction is ranges from 4 to 40 nm.

As can be observed in Fig. 4.5, the error induced by the resolution of the Boussinesq problem is $| \Delta\vec{F} | \approx 4$ nN when the noise in the force field deformation is $\varepsilon_x = \varepsilon_y = 3$ nm and $\varepsilon_z = 12$ nm. We can conclude that we are able to compute force fields with an error of 4 nN when the average value of the overall force field is $\langle F \rangle = 10$ nN.

4.3.4   Iterative Tikhonov regularization method

Any regularization procedure requires to perform some hypothesis about the solution of the ill-posed problem. Up to now, we assumed that the only constraint is that the forces
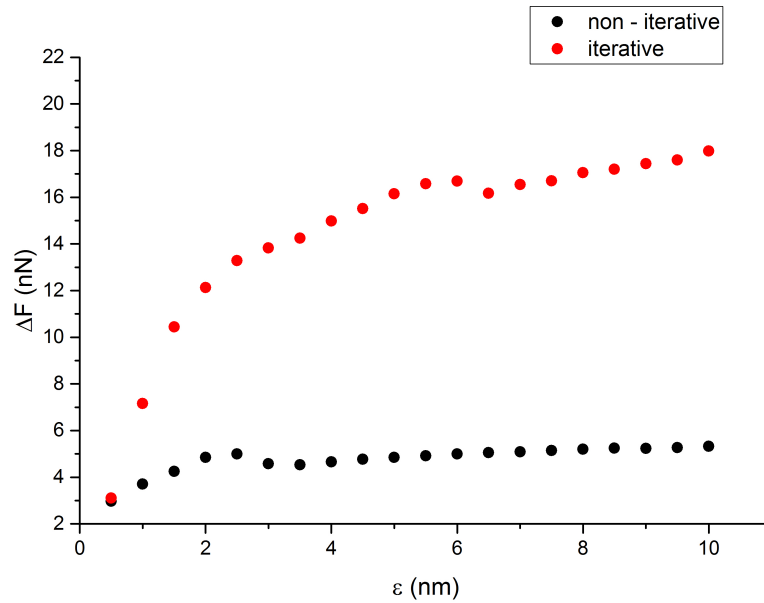
FIGURE 4.5: Difference between the initial force field and the computed force field, as a function of the noise in the displacement field. $\varepsilon_z = 4\varepsilon_{xy}$. Black circles correspond to usual Tikhonov regularization, whereas red circles correspond to iterative Tikhnov regularization.

should not become exceedingly large : $\vec{F}_0 = 0$. In this section, we explore an iterative technique in which the solution of the problem at iteration step $l-1$ is chosen as the regularization solution of the next iteration l.

$$\vec{F}_l = min_F(\mid G\vec{F} - \vec{u} \mid^2 + \lambda^2 \mid \vec{F} - \vec{F}_0 \mid) = (\mid G\vec{F} - \vec{u} \mid^2 + \lambda^2 \mid \vec{F} - \vec{F}_{l-1} \mid) \qquad (4.6)$$

In agreement with our previous resolution, the initial choice of the regularization field is the null force field : $\vec{F}_0 = 0$. Thus, as the result of the first iteration procedure, we recover the previously described solution. The iterative process lasts while differences between force fields vectors at two last steps is larger, than some critical value : $\delta = \frac{|\vec{F}_l - \vec{F}_{l-1}|}{\vec{F}_l} = 0.01$.

The same noise value of the displacement field as in the previous section is chosen, and the error in the calculated force field is plotted in Fig. 4.5. We observe that the iteration increases the overall error in the computed force field . Thus, if $\varepsilon_{xy} = 3$ nm,the error is $\Delta \vec{F} \approx 13$ nN, instead of 4 nN in the absence of iteration.

Let us now consider smaller noise of the deformation field : $\varepsilon_{xy} = 0.2 : 1$ nm (figure 4.6). One can observe, that for small values of the lateral noise ($\varepsilon < 0.3$ nm), the iterative regularization procedure leeds to more accurate values than the one obtained in the
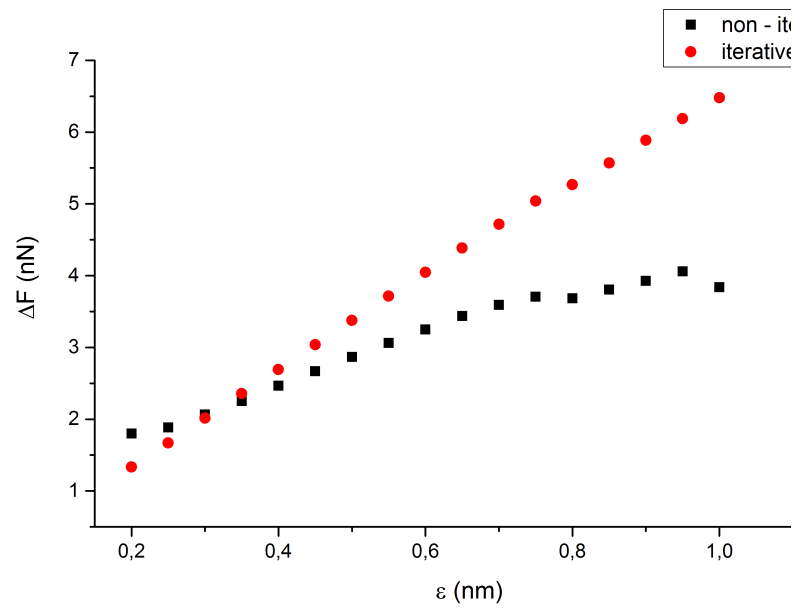

Ch. 4. The software for the experimental data analysis

FIGURE 4.6: Difference between the initial force field and the computed force field, as a function of the noise in the displacement field in the xy plane. $\varepsilon_z = 4\varepsilon_{xy}$. Black circles are obtained without the iterative procedure whereas the red circles correspond to the iterative regularization procedure.

absence of iteration.

We can conclude that, when the noise on the position data is not small enough, the iterations amplify the error induced by the regularization technique. As a consequence, we will not perform any iterative step in our study.

Finally, we can make next conclusions :

– the spatial resolution of the force field is 6 μm.

– the accuracy in calculation one force vector is about 4 nN.

– the iterative regularization method increases the error of the computed stress field and we will use normal zero-order Tikhonov regularization.

Chapter 5

Traction forces during cell adhesion

In this chapter we present the first results obtained with the setup described in the previous chapters. We observe the adhesion of a single cell onto a soft substrate. As a first step, we wish to describe the time evolution of the cellular force field during the adhesion of the cell. To this aim, we first choose a field of view and then inject cells inside the chamber. Then, the position of the probe beads at rest is measured and, once cells begin to deposit, we follow the induced deformation. As a consequence, the presence of a cell in the *a priori* chosen field of view is a matter of luck, but the cell concentration is chosen so that two to four cells on average adhere in the observed region. Most of the experimental parameters are kept identical for all experiments unless otherwise stated :

- cancer colorectal cell line SW 480 is studied.
- the Young modulus of the PAA gel $E = 450$ Pa.
- the probe bead diameter is 0.9 μm.
- each experiment lasts 10 hours.
- the images are acquired every minute.
- the spatial resolution of calculated force field is 6 μm.

Outline

This chapter is divided in five sections :

$\Rightarrow$ 5.1 : we estimate the timescale of cell adhesion and the typical values of traction forces ;

$\Rightarrow$ 5.2 : we describe the anisotropy of the force field, and show that a maximum is usually observed at the border of the cell ;

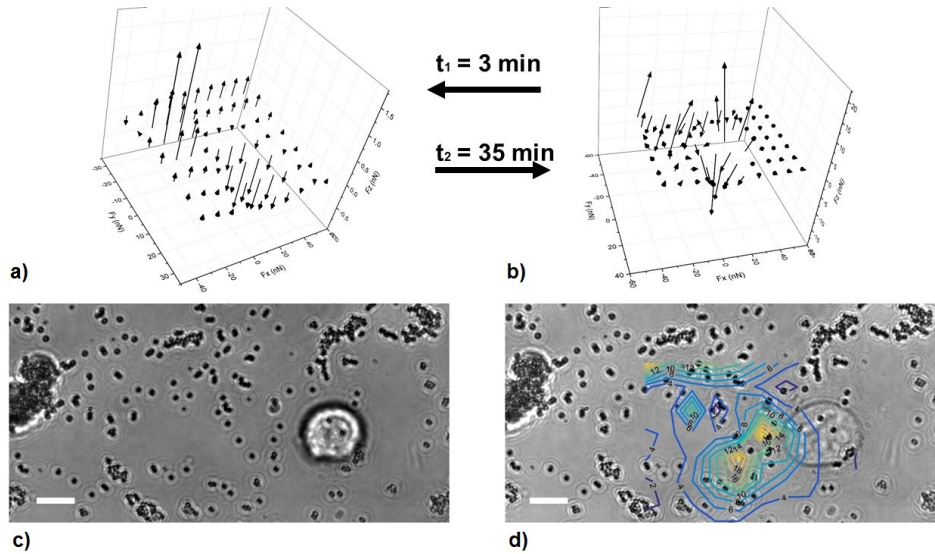$\Rightarrow$ 5.3 & 5.4 : we quantitatively correlate the measured force fields with the cell shape

FIGURE 5.1: Figures (a) and (b) : 3D vector force fields calculated at times $t_1 = 3$ min and $t_2 = 35$ min after the cell deposits onto the surface. Bright-field image, corresponding to the force field in (a) is given in (c).(d) : contour plot of the force vector amplitudes superimposed with the bright-field image of the cell. Values are in nN. Image is acquired at $t_2 = 35$ min, so the force field is the one given in (b). Scale bars : 10 μm.

and cell displacement ;

⇒ 5.5 : we study the influence of and anti-cancer drug NAMI-A on the cellular forces

5.1   Beginning of the adhesion

The experiment starts by the injection of cells inside the medium, that surrounds the gel. In order to reach the surface of the gel and then to adhere, cells need some time. Let us first describe the first steps of the adhesion. Cells usually need a few minutes to sediment onto the gel surface. Then during the first 5 to 10 minutes after their deposition onto the gel surface, no force is measured (the positions of the probe beads remains the same). This situation is shown in Figure 5.1. At time $t = 3$ min after the beginning of the experiment, we measure force vectors with amplitude around 1 nN. After, at $t = 35$ min we measure force peaks, which have amplitudes 16 and 18 nN.

To determine the characteristic adhesion kinetics, we plot the mean value of the force vector as a function of time in Fig. 5.2. One can notice from the left plot, that $\langle F \rangle$ is around zero (except few force fields) for times $t < 20$ min. Then, a sharp rise of the average force is observed, up to ≈ 4 nN. This time coincides with the growing of cells protrusions. We determine the time at which the average force starts to increase by averaging over 10
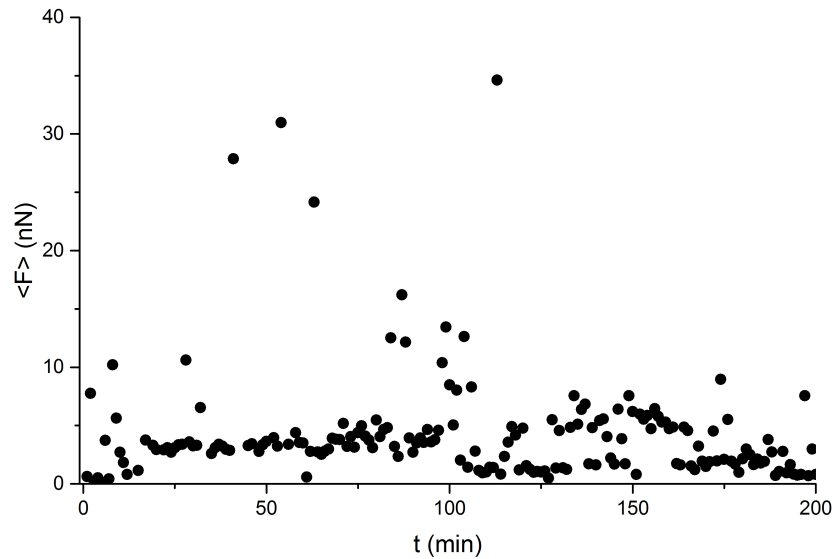
FIGURE 5.2: Average value of the force vector as a function of time for first 200 minutes of experiment.

different experiments. It is equal to $t_0 = 16.2 \pm 5.6$ min. As a consequence, we will assume in the rest of this study that, during the first 10 minutes, no external force is applied, and we choose the first 10 images to determine the average probe beads positions in the absence of applied force.

Another interesting information, that can be obtained from the $\langle F \rangle(t)$ plot is the occurence of "events" in the adhesion process, corresponding to large values of the applied force. Indeed, Fig. 5.2 shows that the mean force amplitude exhibits peaks, corresponding to these "events". We compute the average value of the force vector amplitude from 10 experiments (6000 images). It varies in a wide range : $\langle F \rangle = 27.1 \pm 25.6$ nN. So, values of force vector amplitudes are in the range $2 - 50$ nN. We could transfer these value into stress, taking into account the mesh size of the force field :

$$P = \frac{F}{S} = \frac{2 - 50}{36} \frac{nN}{\mu m^2} \approx 60 - 1400 Pa. \tag{5.1}$$

This range of the traction amplitudes is close to the forces values reported in the literature. For instance, stress field, produced by dictyostelium discoideum cells, have typical stress values around 80 - 150 Pa [92], [63]. And 3T3 fibroblasts induce tractions of the order of 100 - 10 000 kPa [107].

Ch. 5. Traction forces during cell adhesion

5.2   Position of the force peaks

For adherent cells, 3D traction force field usually exhibits one or a few peaks close to the cell boundary. They are usually situated near the cell edge, but not directly under the cell (figure 5.1b). The position of the peaks usually determine the lamellipodia's (filopodia) location, with which cell discover environment and use it in order to move. As lamellipodias are very thin - few hundreds of nm [91], it is difficult to observe them in bright-field microscopy.

Some cells could take "dipole-like" form during their adhesion or motion. In this case cell elongates in some certain direction with usually two filipodias at the edges. An example of this conformation can be observed in Figure 5.3. The position of the force peaks is then shifted with respect to the cell center. They are located under the developing cell protursion. The force field peak shifts to one of the cell edge, where the cell explores the substrate (figures 5.3a and 5.3c). Often at certain times, the cell applies forces in a given direction. On figures 5.3b and 5.3d we detect the rapid creation of new filopodia, that disappear in a few minutes. By this mechanism, the cell seems to try to explore the surface in order to find better place for adhesion. As this behavior does not lead to a net large cell displacement, we will call it "pasive phase" of cellular adhesion, and we analyze it in section 5.4.

Sometimes we can observe the appearance of two peaks at the extremities of the cell. These peaks have opposite z directions : one is pointing towards the substrate although the other one is directed out of it. This behaviour has already been described in [94] and defines the "push-and-pull" motion of the cell. On the leading edge of the cell, it creates a new filopodia, which, in order to adhere to the substrate, pushes it. On the tail side, the cell needs to deadhere filopodia in order to move. During the detachment process, the cell pulls the substrate. Figure 5.4 shows several examples of this motion.

We will call this behavior, characterized by the overall displacement of the cell in the direction of its protrusion, the "active phase" of cellular adhesion. We will discuss quantitatively this type of behavior in section 5.4.

5.3   Cellular force dipole

Cells with elongated (or "dipole-like") shape define preferred direction, along which forces are larger than along other directions. This direction can be computed by conside-
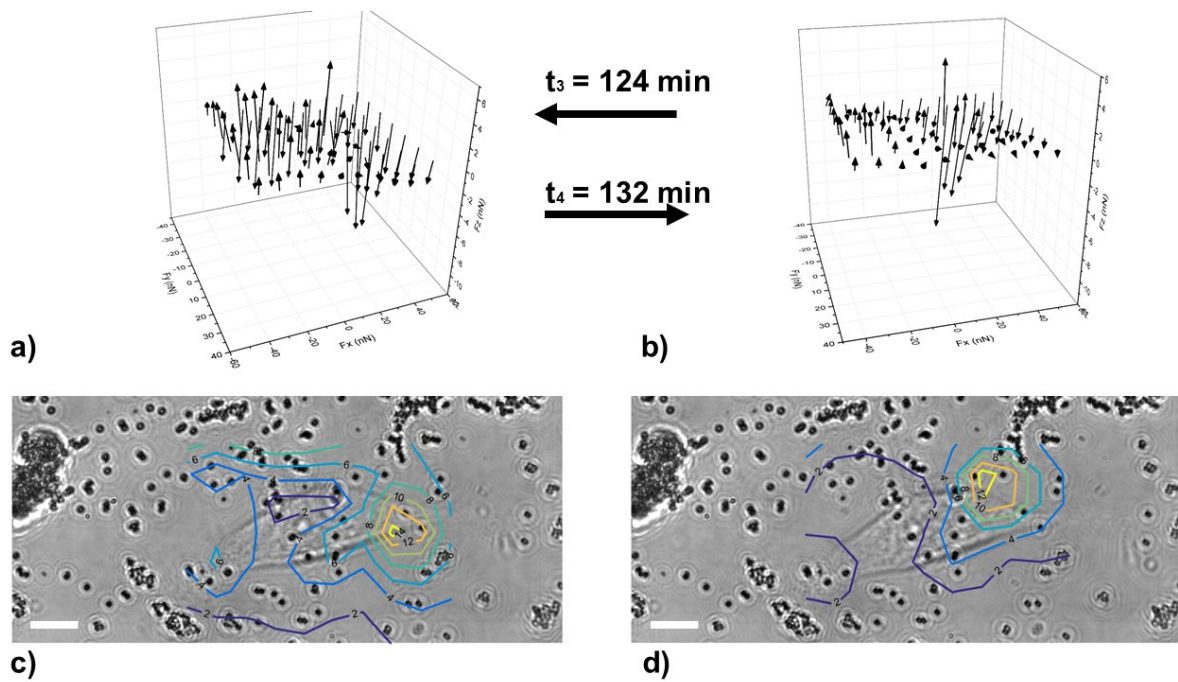
FIGURE 5.3: Three dimensional vector force field and bright field image of the cell super-imposed with contour plot at time $t_3 = 124$ min (a) and (c); at time $t_4 = 132$ min b and d . Values for contour plots are in nN. Scale bars are 10 μm.
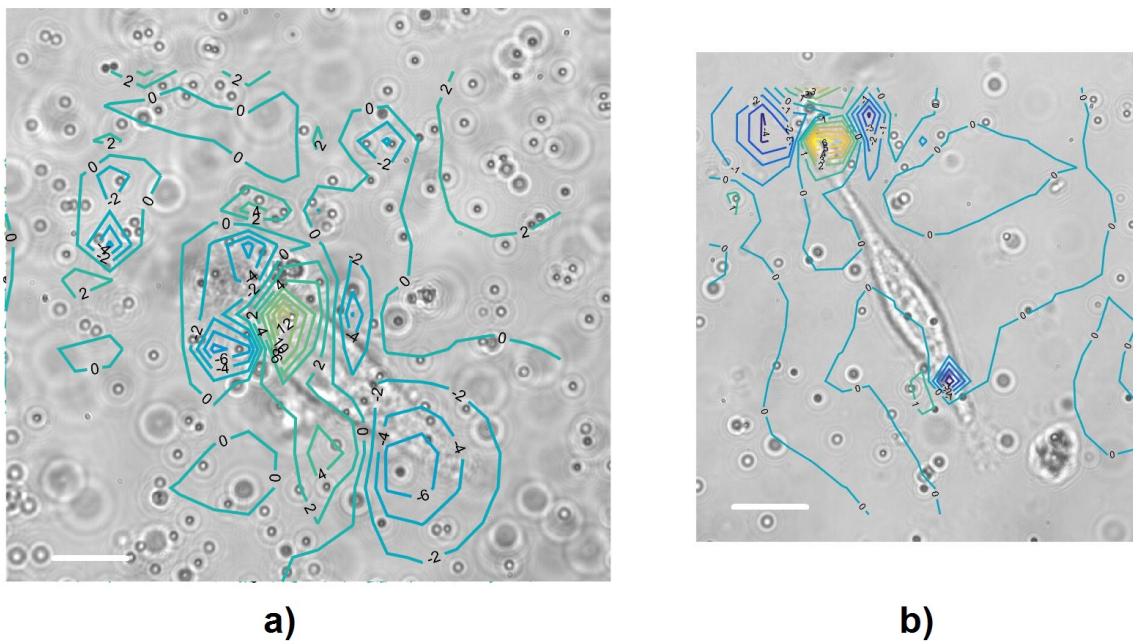

FIGURE 5.4: Figures (a) and (b) : contour plot of the z-components of the force vector field, superimposed with bright-field image of the cell. Scale bars are 10 μm
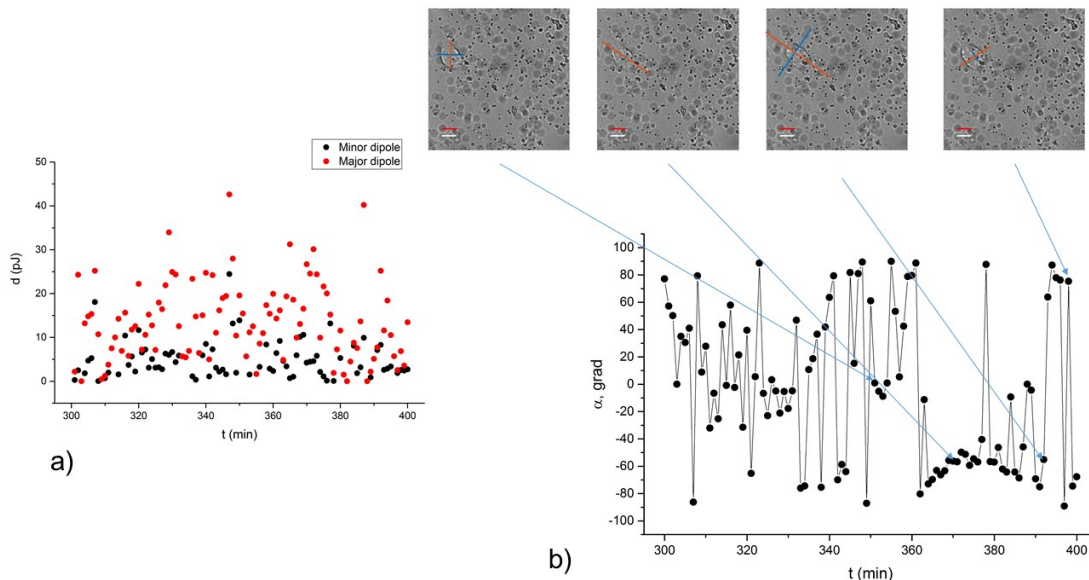
Ch. 5. Traction forces during cell adhesion

FIGURE 5.5: Figure (a) modulus of the major (red points) and minor (black points) dipoles as function of time. Figure b, main plot : angle α between the major dipole axis and vertical line as a function of time. Insets : bright field images of the cell, which corresponds to next timesteps (from left to right respectively) : $t = 351$ min, $t = 370$ min, $t = 392$ min, $t = 401$ min.

ring the following force dipole matrix :

$$M_{ij} = \int_S x_i F_j dS \tag{5.2}$$

where $i, j = x, y$; x_i is the i-component of the force vector position (with respect to the cell center); F_j is the j-component of the force vector, and S is area, where force field was measured, around the cell location. In the following, we follow the analysis of [92].

Let us consider a given experiment that spans over 10 h, with 580 time steps (images). At each time step, the two-dimensional matrix M is computed. Following the analysis of [93], we mainly consider its components calculated from the x and y components of the force field. Two eigenvalues and eigenvectors are thus obtained at each time step. We call the eigenvector with the larger (smaller) absolute eigenvalue the major (minor) dipole.

The absolute values of the major and the minor dipoles are presented on the fig. 5.5a. The values of dipoles d for our cell line SW 480 match dipole amplitudes for human airway smooth muscle cell as measured in [80] : they are of the order of a few pJ. d in our experiment was bothcan be negative or positive, corresponding to cell contraction and stretching, respectively.
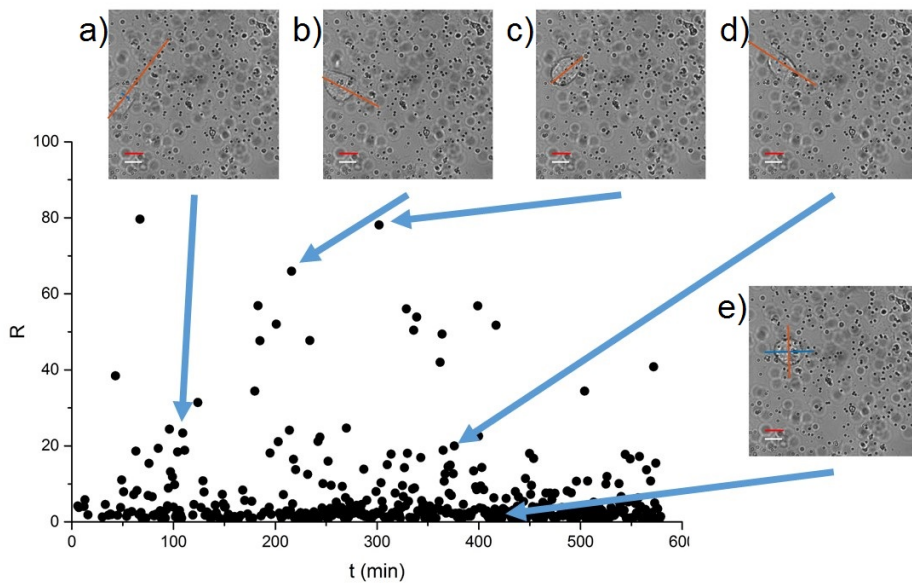
FIGURE 5.6: Ratio of amplitudes between two dipoles as a function of time. Insets : bright field images of the cell, superimposed with two main dipoles. The two eigenvectors of the dipole matrix are represented by orange (major dipole) and blue (minor dipole). Scale bars : 10 μm for length (white) and 2 pJ for dipole amplitude (red). Inset (a) corresponds to timestep $t = 111$ min, (b) corresponds to $t = 216$ min, (c) - to $t = 302$ min, (d) - to $t = 376$ min and (e) - to $t = 432$ min.

When the amplitude of the major dipole is much larger than the amplitude of the minor dipole, the force field is non-homogeneous. It means, that it exists a direction, along which most of the forces are applied. In such situations, it may be expected that the direction of the major dipole coincides with an axis of anisotropy of the cell. Let us first plot the ratio of dipoles amplitudes (figure 5.6) : $R(t) = \frac{|d_{major}(t)|}{|d_{minor}(t)|}$.

High value of the ratio shows the existence of non-homogeneous force field. Most forces are acting along one preferred axis. Looking at the insets of the figure 5.6 one can notice, that for high ratio values ($R > 10$) the cell usually has a dipole-like shape, and the direction of the major dipole almost always coincides with the axis of cell elongation.In some but rare instances, the major axis of the stress field is normal to the cell main direction. But this behavior appears quite rare, and mostly, while cell is elongated, it applies forces along its axis of elongation (figures 5.6a,b,c,d). For small values of the major dipole amplitude (figure 5.6e, $R = 1.06$) we observe round shape of the cell without strong anisotropy of the force field : the amplitudes of major and minor dipoles are similar.

For large anisotropy of the force field (high values of R), direction of the major dipole

Ch. 5. Traction forces during cell adhesion

axis can be conserved during some period of time. On the figure 5.5b we plot direction[1]
of the major dipole axis as a function of time (here we choose a time window between 300
and 400 min after the experiment begins). As can be seen, at times : $t = 360 - 390$ major
dipole orientation almost the same (with some fluctuations). During this time, the cell
exhibits a "dipole-like" shape without changing the direction of the axis along which it
is extended (see fig. 5.5b, insets). Often, the existence of a "plateau" of α corresponds to
a "dipole-like" shape of the cell, conserved (or slowly changed) during the corresponding
timesteps.

5.4   Relationship between forces and cell displacement

We have observed that adherent cells usually exhibit two kinds of behaviors : active and
passive phases. During active phases, the cell moves by using its filopodia/lamelipodia.
In this phase the position of the force peaks, created by cellular protrusions, determines
the direction of the cell motion.

Let us first determine the cell center, extracted from the analysis of the bright-field
images of the cell. The changes of position of the cell center between two time steps lead
to a measure of the cell velocity at this time scale. We superimpose bright - field images
of the cell with contour plot of the force vector amplitudes as well of their instantaneous
velocity over 1 min time scale (Figure 5.7). It can be observed that the direction of the
force peak often determines the direction of cell motion (vector of the cell motion for time
t_i was calculated as : $\delta \vec{r_i} = \vec{r}_{i+1} - \vec{r_i}$).

Nevertheless, the cell not always moves along the direction of the main force dipole. We
thus perform a statistical analysis of the cell displacement as a function of the dipole force.
We compute the angle between the velocity vector and the line that connects the center
of the cell and the position of the force peak (see figure 5.8a). To quantify the velocity
orientation around direction of the force peak position ($\delta\theta$), we compute the probability
distribution function (PDF) of the angle defined by the direction of peak position with
respect to center of the cell, and velocity axes (figure 5.8b).

As expected, the PDF exhibits a peak around $\delta\theta = 0$. Moreover, if we divide all set
of the force field into two sub-ensembles : in the first, the force peak has an amplitude
smaller than 5 nN, and in the second one, force peaks are larger than 5 nN. The PDF
of the second group also exhibits also sharp peak around $\delta\theta = 0$ (figure 5.8c) whereas

---

1. α is determined as the angle between the major dipole axis and the vertical direction.
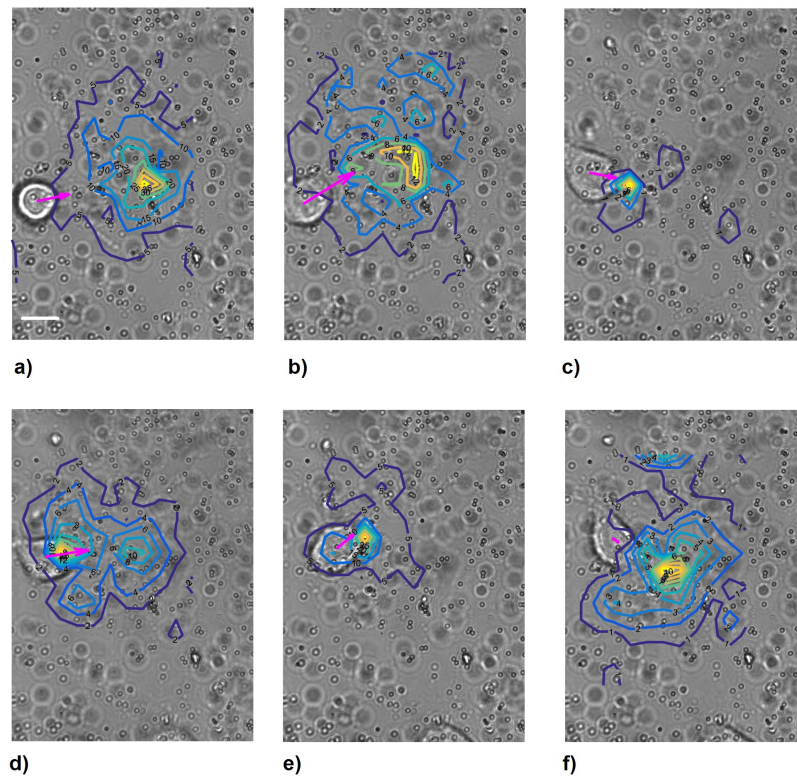
FIGURE 5.7: Bright-field images of the cell superimposed with contour plots for force vector amplitudes and vector of the cell motion (purple). Figure (a) correspond to timestep $t_1 = 17$ min, (b) to $t_2 = 53$ min, (c) to $t_3 = 220$ min, (d) to $t_4 = 251$ min, (e) to $t_5 = 299$ and (f) to $t_6 = 350$ min. Scale bar is 10 μm. The length of the cell motion vectors is increased in 10 times.
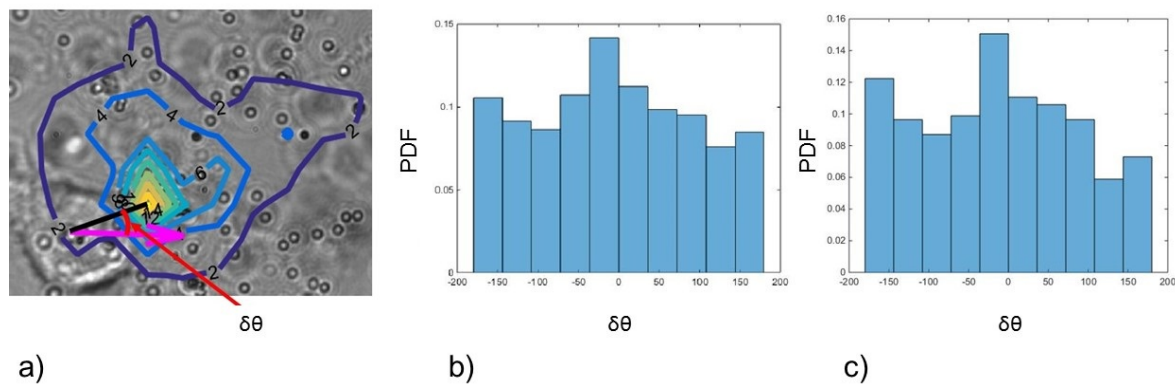
FIGURE 5.8: Figure a : graphical explanations of the angle $\delta\theta$. It is the angle between velocity vector (purple), and line which connects center of the cell and force peak position (black). Figure b : PDF of $\delta\theta$ for one experiment with 600 timesteps. Figure c : PDF of $\delta\theta$ for the same experiment, for the force peaks, that are larger than 5 nN.

the PDF for the fist group which was almost homogeneous (all $\delta\theta$ appears with the same probability), illustrating the fact that the cell motion is mostly induced by the larger forces.

During the passive phases, the cell "discovers" its environment with lamellipodia while remaining almost at the same place. In this phase processes of lamelipodia's protrusion and retraction are frequent. Such a situation is illustrated in Figure 5.9. The cell pulls the substrate in the left part of image at $t \approx 170 - 190$ min, that afterwards disappear. Despite the direction of applied force with respect to the cell center, the cell remains almost motionless. Usually cell in the passive phase creates lamellipodias in many different directions in order to explore its surrounding substrate.

To show the difference between the two phases, let us plot the x and y positions of the cell center for two experiments : in the first experiment, the cell is almost always in an active phase (previously described) whereas the cell remains in its passive phase during the second experiment (figure 5.10a). It can be observed that the displacement of the cell in the active phase is much higher than in its passive phase.

Similarly to our analysis of the active phase, let us consider the PDF of $\delta\theta$ for the data corresponding to the passive cell behavior (figure 5.10b). Here, the most frequently occurring values of $\delta\theta$ are $\delta\theta = 0°$ and $\delta\theta = 180°$ (this last value corresponds to a cell moves in the opposite direction to the force peak position). The existence of these peaks can be explained by the observation of the cell from which we propose the following mechanism of exploration of its environment :

First, the cell creates a lamellipodia and moves a bit in its direction ($\delta\theta = 0°$). After
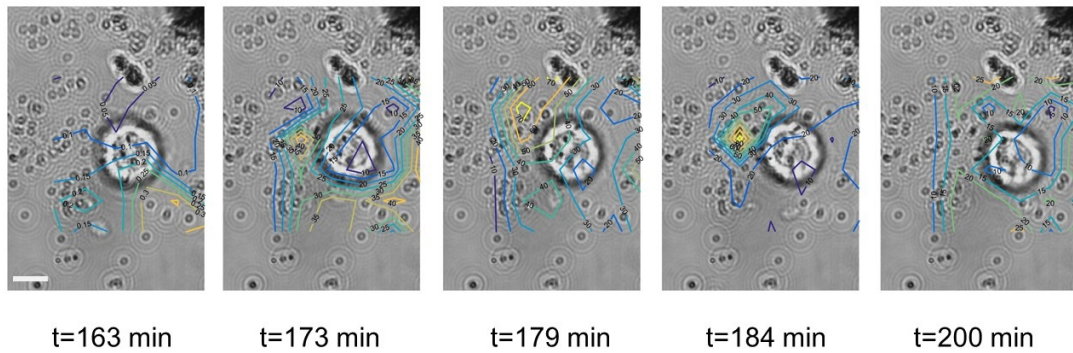
FIGURE 5.9: Contour plots, of the force vector amplitudes superimposed with bright-field images of the cell at different timesteps experiment. Values are in nN. Scale bar is 10 μm.
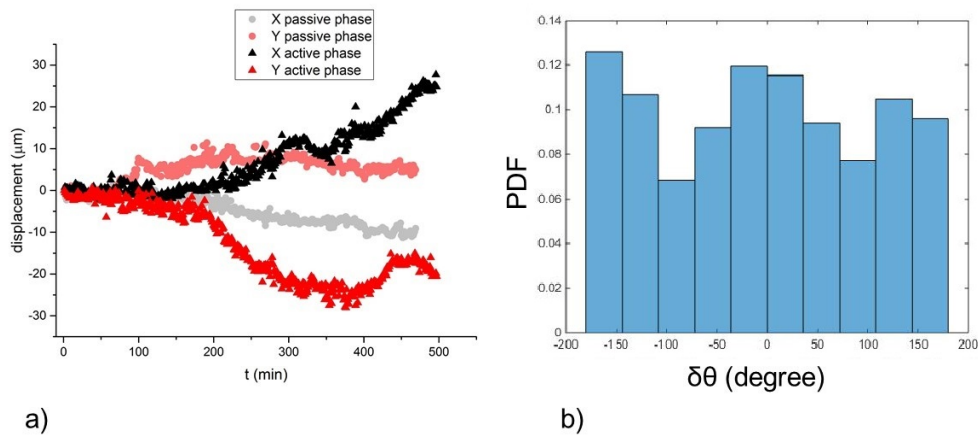

FIGURE 5.10: Figure (a) : x and y components fof cellular motions with respect to its initial position. Circles correspond to the passive phase of the cell whereas triangles correspond to the active phase. Figure (b) : PDF of $\delta\theta$ within passive cell behavior for 470 timesteps.

a while, the cell stops its motion in this direction, and moves back ($\delta\theta = 180^o$), while the lamellipodia retracts.

To quantify the cellular motility during the active and the passive phases, we plot mean squared displacement (MSD) for both situations (figure 5.11). One can notice directly that during the passive phase, the cell is much less motile than in the active phase.

We calculate the slopes [2] of the curves on the figure 5.11 for smal t : 1-20 min and big t : $t > 100$ min. At the beginning similar values for α : 0.42 in the active phase and 0.31 in the passive phase, corresponding to a subdiffusive motion of the cell on small timescales. For larger timescales, the slopes are equal to 1.29 for the active phase and 1.8 for passive phase, and the motion is superdiffusive. The crossover between the two

---

2. Slope is defined by α, where α is power of the time for MSD dependence : $< \Delta x^2 > \propto t^{\alpha}$
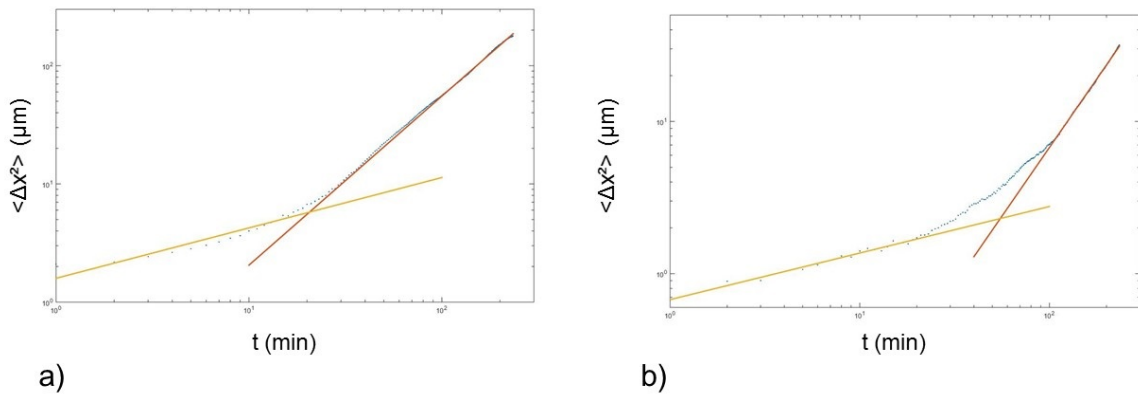
FIGURE 5.11: Mean squared displacement calculated for the cell center positions in active phase (figure (a) and passive phase (figure b). Points shows calculated MSD from the experiment and fitting lines have slopes : 0.42 and 1.29 on the figure (a) (yellow and red lines respectively) ; 0.42 and 1.29 on the figure b. Plots are in log-log scale.

regimes occurs at $t \approx 15$ min (for active phase) and $t \approx 55$ min for passive phase, that is much bigger than the typical timescale of filopodia's protursion, which is in order of minutes [91]. Nevertheless, further discussion of the slopes of mean squared displacements requires more statistics.

5.5 Influence of NAMI-A

We have begun to perform experiments in order to quantitatively assess the change in adhesion properties when the cells are treated with NAMI-A (see section 1.7). We treated carcinoma cell line SW 480 with different concentration of NAMI-A. For concentrations larger than 100 μM cells did not adhere to the collagen treated PAA gel. Cytoxicity test shows no influence to the SW 480 cell line proliferation at concentrations up to 200 μM. So, we studied cellular adhesion at NAMI-A concentrations equal to 1 μM and 5 μM.

We plot average force vector amplitude for each force field, as a function of time (figure 5.12). For small drug concentration (1 μM, figure 5.12a) $\langle F \rangle$ exhibits the same characteristics as non-treated cells : a sharp increase of the average force vector amplitude is observed at $t = 12$ min and the plateau value of the force is of the order of 40 nN. At higher NAMI-A concetration (5 μM, figure 5.12b), the long time plateau value is smaller (around 10 nN). The main difference with respect to adhesion of non-treated cells, it is time of beginning cell attachment. Treated with NAMI-A cancer cell begun to adhere in 70 minutes after adhesion (the typical time of adhesion start is 16 min after cell seeding - see section 5.1). Moreover, it deadhered after $t \approx 170$ min.
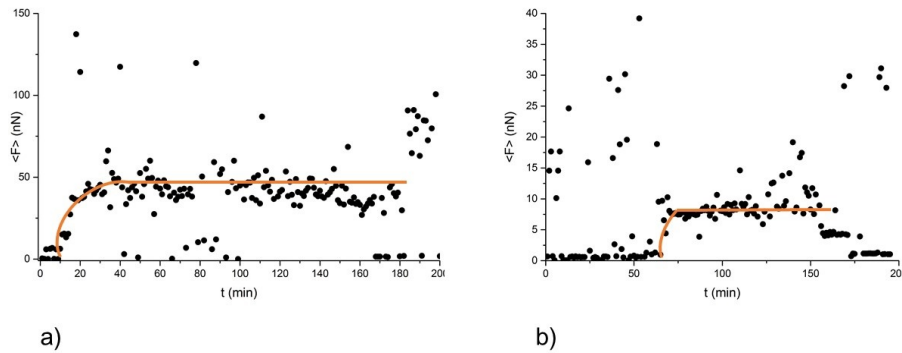
FIGURE 5.12: Average amplitude of the force vector as function of time for the cell treated with NAMI-A. Concentration of the drug is 1 μM (figure a) and 5 μM (figure b). Approximate values of the mean force shelf are marked by orange lines.

Apart from the mean applied force, we also notice that cells, treated with higher drug concentration do not exhibit shape polarity[3]. This behavior is opposite to the case of cells treated with 1 μM of NAMI-A, that, as usually, have an elongated shape. As we mentioned in section 5.4, we can link cell polarity with the ratio of two main dipole amplitudes of the force field R. The ratio R as a function of time, while cell is adhered, for cells treated with 1 μM and 5 μM of NAMI-A, is presented on figure 5.13. As one can see, ranges of R values are different, and, respectively, the mean values of the ratios are also different : $<R> = 10.06$ for smaller drug concentration and $<R> = 4.71$ for larger drug concentration. Small value of the ratio means that both major and minor dipoles has similar values of the amplitudes, and there is no strongly expressed preferable direction for the force vectors. In this situations we expect a round shape of the cell, that is indeed observed in the experiment at 5 μM NAMI-A concentration.

We also notice the extremely small cell mobility during its adhesion (for cell treated with 5 μM of the drug). Let us plot the MSD of the cell center (similar to the figure 5.11). It deviates around value of 6 μm that is much lower than for non-treated cells (even in passive phase), and no net displacement of the cell is observed.

A deeper and systematic study of the influence of NAMI-A onto cell adhesion is currently performed.

---

3. Cells remain almost round while its adhered

Ch. 5. Traction forces during cell adhesion

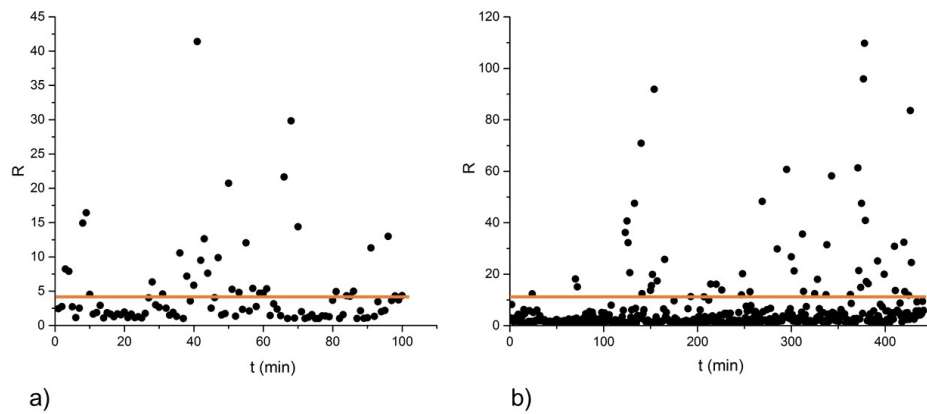FIGURE 5.13: Ratio of amplitudes between two dipoles as a function of time. Figure (a) represent the experiment with the cell treated with 1 μM of NAMI-A ; figure (b) - cell is treated with 5 μM of NAMI-A. Orange lines shows mean values of R.
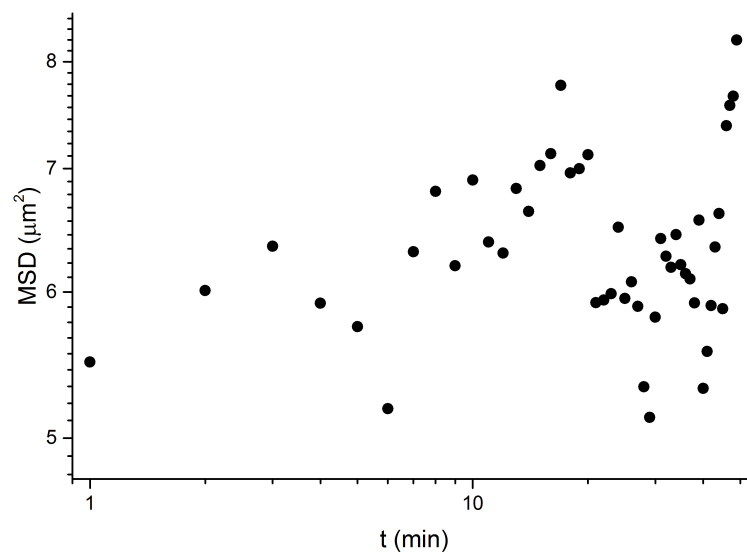

FIGURE 5.14: Mean squared displacement calculated for the cell center positions, that is treated with 5 μM of NAMI-A. Plots are in log-log scale.

Chapter 6

Perspectives and conclusions

In this chapter we will conclude everything that was done during the thesis and discuss some possible future modifications of the setup.

6.1 Conclusions

The main conclusions of my work :

1. We used digital holography microscopy (DHM) in order to measure the forces exerted by a cell onto a soft substrate,

2. We built the optical microscope for DHM measurements, taking to account the necessary conditions for cell culture proliferation.

3. We created a software to control experimental process. It allows us observe and save acquired images from the camera at different focal planes under the cell.

4. We create package of routines in order to analyze positions of the markers and then derive the traction force field, created by cell.

5. We perform first experiments with adhesion of the cancer cells on the hydrogel and calculate force fields. Our results allow us to relate the displacemnt of a cell with the forces it applies onto its substrate. We have moreover begun to study the evolution of the forces exerted by a cell when treated with NAMI-A.

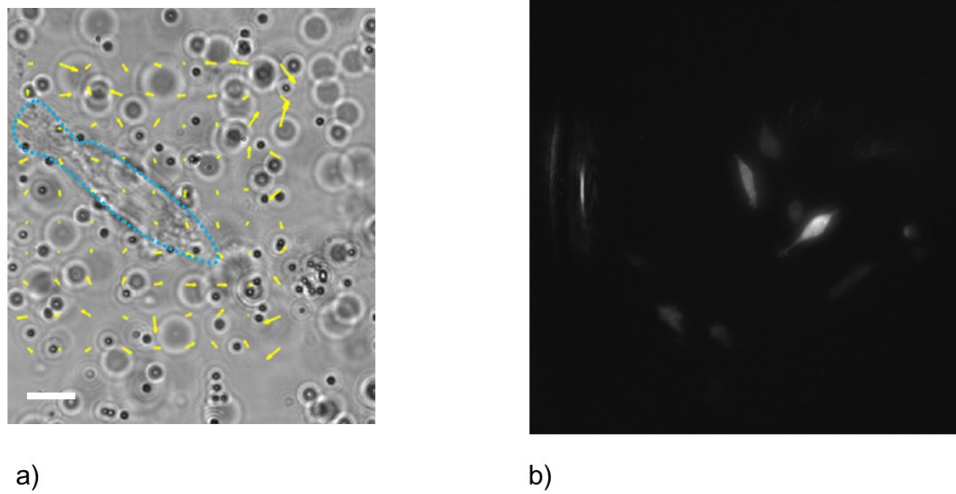a)   b)

FIGURE 6.1: Figure (a) : xy traction force field (yellow vectors) superimposed with a bright-field image of the cell. Blue dotted line shows approximate contour of the cell. Scale bar is 10 μm. Figure (b) : fluorescent image of the cells, obtained with our setup.

6.2   Perspectives

6.2.1   Precise determination of the set of points where forces are applied

We have calculated the force field over an ensemble of points that define a square mesh. They remain the same at any time step (usually during 600 s). The area for the force points mesh should thus be as small as possible at the same time being large enough to cover all positions of the cell during experiment. At a given time, some of the force points will be located outside the cell projection on the substrate. For instance, figure 6.1a is an example of a situations where most of the points at which the force field is computed lie outside of the cell area. As a consequence, the force vectors are computed at points, where force field is equal to zero. It means, that we introduce generally non-zero forces at points, where force obviously is not applied. This brings more uncertainty in our ill-posed problem (see section 2.3).

In order to prevent this, we have to know the exact position of the cell with all its filopodias and lamellipodias at every timestep t of the experiment. This can be done by using fluorescent imaging of the cell. We built part of the setup, that corresponds to fluorescent cell images. So, at the moment we are able to acquire images of the cell

transfected with $p^{CAG} - LifeAct - TagGFP2$ 6.1b.

When fluorescent images are obtained from the experiment, they have to be analyzed. As brigth-field and fluorescent images have different scales, one needs to precisely rescale one image on top of the other. For this, some reference points are usually used. In our case, these reference points should be imaged by both fluorescent and bright-field images. Then, knowing position of the cell in the same system as displacement field of the beads, one can measure the force field just underneath the cell and not around it.

6.2.2 2D bead placement

The experiments have been performed by dispersing probe particles randomly inside the substrate. This has two drawbacks : out-of focus beads blur the image of the beads we are interested in. As we are working with partially coherent light, this effect extends up to several micrometers far from the beads of interest. In figure 6.1a we see large circles, due to microspheres under the focal plane. Thus, it would be desirable to create a plane of beads at the surface of the gel or just underneath the surface. This would increase the number of tracked beads by unit of area and would thus enhance the overall spatial resolution of the technique. Thus, in [58], Marinkovic et al. used fluorescent nanobeads, chemically linked to PAA gel surface. I developed new protocol, which allows to bond the beads to the gel surface without chemicals.

In our protocol for the polymerization of the acrylamide solution is performed between two plates : the treated bottom surface of the petri dish and a non-treated glass slide (see figure A.2). Petri dish is held upside down, and acrylamide solution can be detached out of the non-terated glass surface after polymerization. We have developed a variant of this protocol in which a layer of beads is created onto the non-treated glass slide (that is the one onto which the cell will attach). To this aim, the beads are first deposited onto the glass slide before the solution of acrylamide is poured and they bond to the gel surface (figure 6.2). We have not studied the adhesion between the gel and the beads, but it may be expected that stronger Van der Waals attraction between the acrylamide gel and the beads rather than betwen the glass slide and the beads is responsible for the detachment of the beads from the glass surface.

Protocol for beads preparation at the surface of the gel :

1. Mix 50 μl of 10% aqueous suspension of the latex beads (MFCD00131492, *Sigma Aldrich*) with 950 μl of ethanol to obtain 1 ml of 0.5% aqueous suspension of the latex beads.

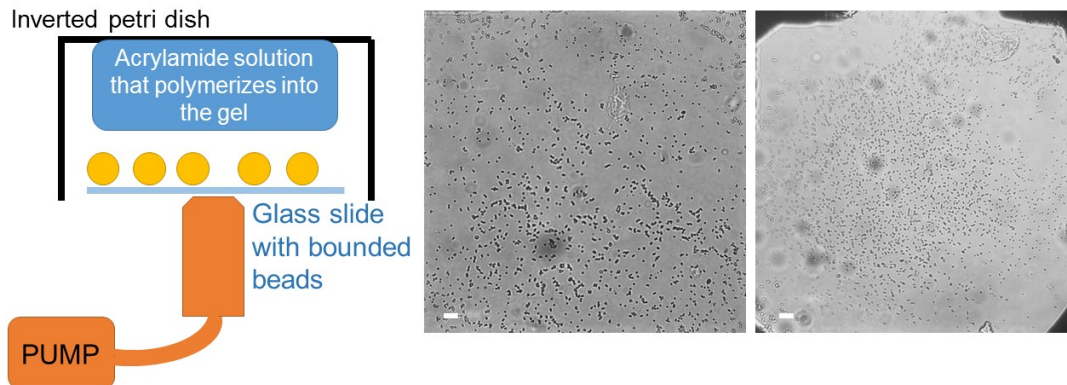2. Pour 30 μl of this suspension on the 14 mm diameter glass slide .

FIGURE 6.2: Figure (a) : Schematic representation of the 2D bead positioning method. Figure (b) : Images of the gel surface with the beads, which are placed in one plane. Scale bars are 10 μm.

3. Place the glass slide with suspension inside the centrifuge. Run centrifuge with angular velocity : $\omega = 2500$ 1/min for 3 minutes.

4. Melt the beads on the glass slide in the oven for 7-10 minutes at temperature T=150°C.

5. Use this glass slide with the bounded beads in order to squeeze acrylamide solution during the gel polymerization (figure 6.2a).

For one single layer of the beads on the gel surface, we prepare acrylamide solution without beads.

We have encountered two main difficulties during the preparation of glass slides with adherent beads : aggregation of the beads and control of the adhesion strength between the glass slide and the latex beads. We want to have maximum possible markers concentration (because it will determine spatial resolution of the displacement field and as a result the spatial resolution of the force field). But large bead concentration will cause aggregation of the microspheres during the spin coating step. In order to limit aggregation we use first disperse the particles in ethanol (due to its high speed of evaporation in the air and small coefficient of surface tension).

The force with which the particles are held on the glass slide depends on the melting process. The time and the temperature for the melting, described in the protocol was

obtained empirically. Low adhesion strength between the beads and the glass slide induces direct mixing of the beads with the acrylamide solution. On the opposite, high adhesion strength (that can appear in case of long melting process) will prevent the beads from detaching from the glass surface when the gel is separated from the preparation mould.

Images of our gels, prepared with the new protocol, are given on the figure 6.2b. One can notice the main difference between these images and images of the gel with random bead position distribution : the bead concentration is higher and the background noise is lower. Nevertheless, we can observe that some beads are embedded inside the gel (of the order of 10 to 20 %).

We still need to find the optimal beads concentration under this protocol, following our reasoning in section 3.3.3.

Appendix A

Typical experiment procedure

A typical experiment consists in :

– the preparation of the polyacrylamide (PAA) gel,

– the cell culture and

– performing TFM measurements.

A.1 Protocol for PAA gel fabrication in the petri dish [88]

The gel is prepared inside a petri dish. The bottom surface of the gel is covalently attached to the previously silanized glass slide (Fig. A.1a) using glutaraldehyde. As cells do not adhere to polyacrylamide, the gel surface is coated with collagen (using Sulfo-Sanpah as a cross-linker).

Treatment of the glass bottom of the petri dish

1. Deposit 1 ml of NaOH, 0.1 mol/l for 15 minutes.

2. Rinse the petri dish with distilled water 3 times and dry with the air pistol.

3. Deposit 1000 μl of a 0.5% EtOH solution of APTES (3-Aminopropyltriethoxysilane) for 5 minutes.

4. Rinse with EtOH 3 times.

5. Rinse with distilled water 5-7 times, dry with the air pistol.

6. Deposit 1 ml of a 0.5% Glutaraldehyde solution for 30 minutes.

7. Rinse the petri dish with distilled water 3 times and dry with the air pistol.
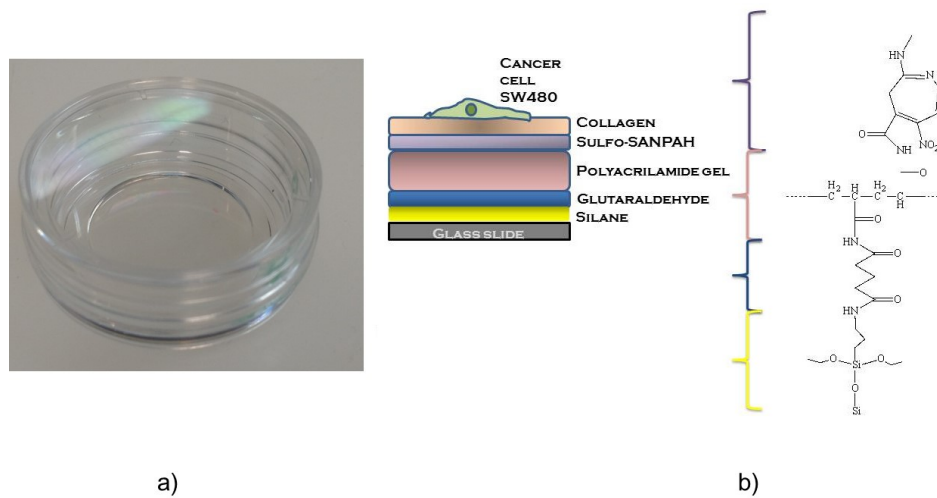
FIGURE A.1: Figure (a) : Picture of the petri dish. Figure (b) : Shown here are chemicals used for the preparation of the gel.

The Petri dish can be stored a maximum of 2 weeks at 4 degrees.

Gel fabrication inside the petri dish

We use polysterene beads (*POLYSCIENCES 07310*, 1.025 μm in diameter).

1. Dissolve 0.5 ml of a 10% solution of acrylamide with 0.5 ml a solution of 0.1% bis-acrylamide. This gives a solution of 5% acrylamide and 0.05% of bis-acrylamide, which has an elastic modulus equal to 0.43 kPa (see table A.1).

2. Add 30 μl of polystyrene beads (concentration 2.64%).

3. Add 6 μl of 1% APS (Ammonium persulfate) and 4 μl of TEMED (Tetramethyle-thylenediamine) to polymerize the gel.

4. Immediately deposit 5 μl of the solution on the petri dish glass slide, which is hold by a suction on a custom-made set-up (Fig. A.2). This device allows to squeeze the solution droplet between the activated glass side (silanized and activated with glutaraldehyde) and a second glass slide (non-activated, placed on top). The compression is stopped when the radius of the droplet reaches the boundaries of the bottom glass. This procedure should result in a gel thickness of 50 to 70 μm.

5. After 30 minutes, fill the petri dish with distilled water.

6. Carefully remove the non-treated glass slide from the gel with tweezers or needle.

The gel should be stored in MilliQ water to avoid drying at 4°C for a week.

Ch. A. Typical experiment procedure
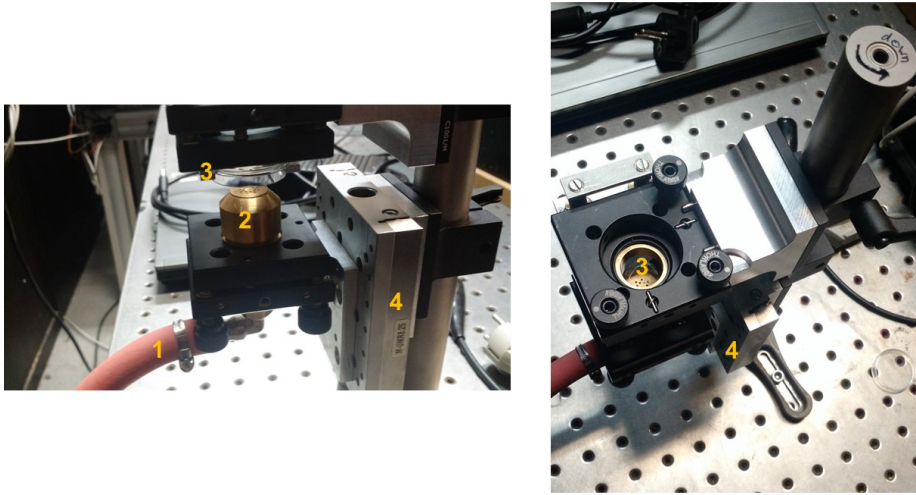
FIGURE A.2: The custom-made setup used for the fabrication of the polyacrylamide gel. See text.

TABLE A.1: Young's modulus of a PAA gel for different concentrations of acrylamide and bisacrylamide. Adapted from [88].

Acrylamide (%), 0.5 ml	Bis-acrylamide (%), 0.5ml	Young's modulus (kPa)
10	0.1	0.43
10	0.2	1.43
10	0.4	2.02
15	0.1	1.53
15	0.2	2.83
15	0.4	5.35
24	0.29	16.34
24	0.9	34.26
24	1.2	55.29

Treatment of the gel surface

1. Rinse the gel inside the petri dish with PBS (Phosphate buffered saline, pH 7.4), 3 times. Remove all PBS.

2. Immerse the gel in 1 ml solution (Sulfo-Sanpah 1 mM/l, HEPES 200 mM/l pH 7.5) and let it under UV irradiation for 5 minutes.

3. Repeat first and second step once again and rinse the gel again with PBS (3 times).

4. Immerse the gel in 1 ml collagen solution (0.2 mg/ml). Let overnight at 4^oC.

5. Rinse with PBS 3 times and let the gel (still immersed in PBS) under UV irradiation for 20 minutes.

6. Rinse the gel with PBS (3 times).

The gel can be stored in PBS for a maximum of two days at 4^oC.

A.2 Cell culture

The cell line we have used in the experiment is a human colorectal cancer line : SW480. The culture medium used is a Dulbecco's Modified Eagle Medium (DMEM) with 10% of growth factor, glucose and antibiotics. The cell line is spitted every week as follows :

1. Rinse the petri dish with the cells with 1 ml of Versene.

2. Leave 1 ml of Trypsine for 5 minutes in the petri dish (to detach cells from the bottom of the petri dish).

3. Pour 20 μl of this suspension in a new petri dish with 4 ml of the cell medium. This petri dish should be conserved at 37^oC and in 5% of CO_2 (till the next splitting).

4. For the experiment, 40 μl of the cell-trypsine suspension mixed with 2 ml of the cell medium should be poured in the petri dish with the gel.

Note that the medium should be changed twice a week.

A.3 Experiment

Before the experiment, some procedures should be done in order to minimize thermal drift, determine the initial bead positions, etc.

1. Heat the setup. This should be done at least 3 hours before the start of the experiment (to reach a proper temperature stabilization).
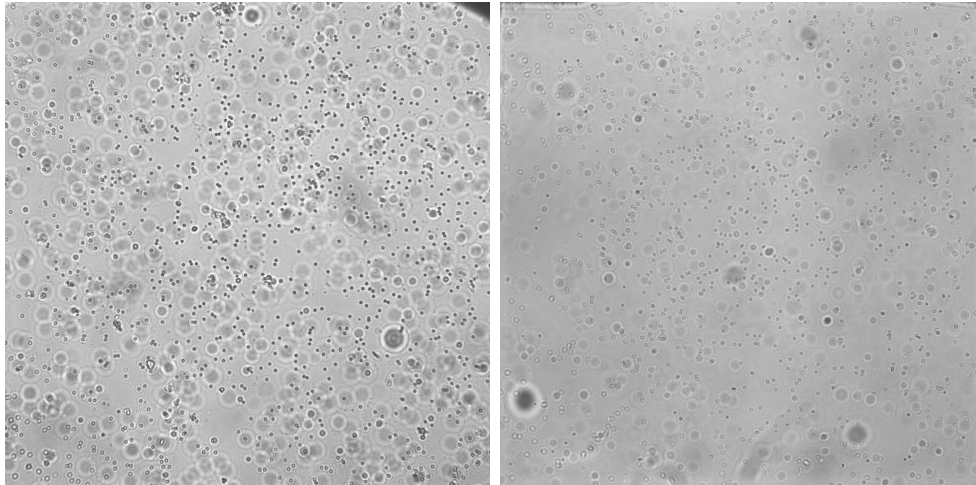
FIGURE A.3: Examples of the "good regions" used for bead tracking. In such regions, the concentration of the beads is high and there are only a few beads at a different height.

2. Place the petri dish (PORVAIR) in 1 ml cell solution in the setup. In addition, 1 ml medium solution (which will be mixed with the cell solution) should be placed at 37°C.

3. Make two holes in the petri dish and cover it with the CO_2 enclosure.

4. Choose a proper field of view (Fig. A.3).

5. Measure the LUT for the reference and track beads, using *LabView* software "TRACK". Two regions should be chosen : one at the bottom of the petri dish (for the reference beads) and one near the gel surface (for the tracking beads).

6. Detach cells from the bottom of the standard petri dish (see section "Cell culture").

7. Mix 1 ml of the warm medium solution with 40 μl of the cell-trypsine solution. The mix should be gently inserted in the petri dish.

8. Start the tracking procedure, by using the routine *LabView* "TRACK". Optimal tracking planes are situated a few microns below the focus.

Appendix B

Correction of the axial displacement

In order to create the set of reference images for the LUT piezo with the objective was moved by step Δz. But axial distance between two focal planes will be different from Δz, due to the mismatch in refractive index medium where is the focal plane situated and immersion oil [99], [100]. Visser et al. [99] derived the formula which relates the displacement of the objective Δ_s and the focal shift Δ_f :

$$\Delta_f = \frac{\tan(\sin^{-1}(NA/n_1))}{\tan(\sin^{-1}(NA/n_2))}\Delta_s = \alpha\Delta_s \tag{B.1}$$

where n_1 is the refractive index of the immersion oil, n_2 - the refractive index of the medium and NA - numerical aperture of the objective. In our case, medium is polyacrilamide gel with a refraction index close 1.33. Then, the calculated value of α for our setup is around 0.5.

We determined α experimentally. For this we made three samples with known thickness (size in z direction), and placed beads on the surfaces of the samples. Sample is fiiled with water in order to have the same refractive index as in polyacrilamide gel. Then, by moving stage with the specimen, we focus the objective on each plane. We measure distance covered by the stage and compare it with real know values of the sample thickness - figure B.1.

Assuming equation B.1 we fit data with the curve : $A = \alpha B$. We found value of the correction coefficient : $\alpha \approx 0.817$, so all displacements of the objects inside the gel, are almost 20% smaller than we measure. This coefficient we include in all our calculations of z component of the beads displacements.
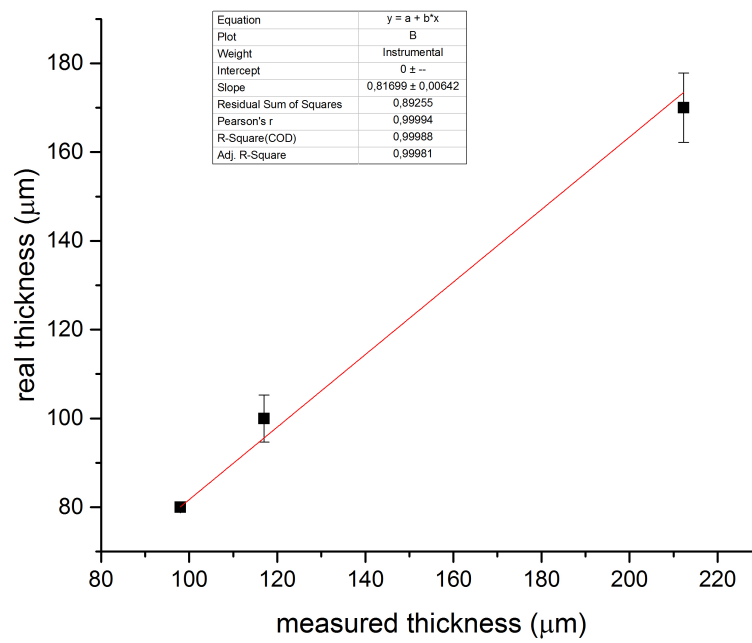
FIGURE B.1: Real thickness of the object, filled with water, as a function of measured experementally thickness.

Bibliography

[1] D. Affonce, and K.R. Lutche New Perspectives on the Mechanical Basis *J. Appl. Physiol.*, **101**, *6*, 1710-1719, 2006.

[2] M.J. Paszek et al. Tensional Homeostasis and the Malignant Phenotype *Cancer Cells*, **8**, *3*,241 - 254, 2005.

[3] J.C. Tan, F.B. Kalapesi, M.T. Coroneo Mechanosensitivity and the Eye : Cells Coping with the Pressure *Br. J. Ophthalmol.*, **90**, *3*, 383 - 388, 2006.

[4] G.A. Domez, R.W. Mclachan, A.S. Yap Productive Tension : Force-Sensing and Homeostasis of Cell - Cell Junctions *Trends Cell Biol.*, **21**, *9*, 499 - 505 , 2011.

[5] J. Neitzel, M. Rasband URL : http ://www.nature.com/scitable/topic/cell-communication-14122659 *Cell Communication* 27/07/2016 .

[6] S. Pellegrin, H. Mellor Actin Stress Fibres *J. Cell Sci.*, **120**, *20*, 3491 - 3499, 2007.

[7] B. Alberts et. al Molecular Biology of the Cell *Garland Science, New York*, 2002.

[8] C. Jacobs, H. Huang, R.Y. Kwon Introduction to Cell Mechanics and Mechanobiology *Garland Science : New York*, 2012.

[9] A.F. Huxley, R. Niedergerke Structural changes in muscle during contraction : interference microscopy of living muscle fibres. *Nature*, **173**, 971 - 973, 1954 .

[10] M.L Gardel et al. Mechanical Response of Cytoskeletal Networks *Methods Cell Biol.*, **89**, 487 - 519, 2008.

[11] D.N. Simon and K.L. Wilson The nucleoskeleton as a genome-associated dynamic network of networks *Nat. Rev. Mol. Cell Biol.*, **12**, 695 - 708, 2011.

[12] M.J. Bissell et al. Tissue structure, nuclear organization, and gene expression in normal and malignant breast *Cancer Res.*, **59**, 1757 - 1764, 1999.

[13] J. Lammerding Mechanics of the Nucleus *Compr Physiol.*, **1**, *2*, 783 - 807, 2011.

[14] D.H. Kim et al. Volume regulation and shape bifurcation in the cell nucleus *J. Cell Sci.*, **129**, *2*, 3375 - 3385, 2015.

[15] H. Karcher et al. A Three-Dimensional Viscoelastic Model for Cell Deformation with Experimental Verification *Biophys. J.*, **85**, 3336 - 3349, 2003.

[16] D.E. Ingber Tensegrity II. How structural networks influence cellular information processing networks *Biophys. J.*, **85**, 3336 - 3349, 2003.

[17] Y.L. Wang, D.E. Discher Methods in Cell Biology *Cell Mechanics, Elseiver*, **V.83**, 2007.

[18] W. Meng, M. Takeichi Adherens Junction : Molecular Architecture and Regulation *Cold Spring Harb. Perspect Biol.*, **1**, *6*, 2009.

[19] T.P. Lele et al. Tools to study cell mechanics and mechanotransduction *Methods Cell Biol.*, **83**, 443 - 472, 2007.

[20] G. Bell, M. Dembo and P. Bongrand Cell adhesion : competition between nonspecific repulsion and specific bonding *Biophys. J.*, **45**, 1051 - 1064, 1984 .

[21] K.J. Painter, N. Armstrong and J.A. Sherratt The impact of adhesion on cellular invasion processes in cancer and development *J. of Theor. Biol.*, **264**, *3*, 1057 - 1067, 2010.

[22] A. Engler et al. Substrate compliance versus ligand density in cell on gel responses *Biophys J.*, **86**, 617 - 628, 2004.

[23] S. Despax Complexation de lADN par des composés organoruthénés et étude de ladhésion cellulaire sur des substrats mous (Ph.D. manuscript) *Université de Strasbourg - Institut de Physique et Chimie des Matériaux de Strasbourg*, 2014.

[24] J.W. Breslin, K.M. Kurtz Lymphatic Endothelial Cells Adapt Their Barrier Function in Response to Changes in Shear Stress *Lympatic research and biology*, **7**, *4*, 229 - 237, 2009.

[25] R. Dardik et al. Flow conditions modulate homocysteine induced changes in the expression of endothelial cell genes associated with cell-cell interaction and cytoskeletal rearrangement *Thromb Haemost.*, **88**, *6*, 1047 - 1053, 2002 .

[26] N. Wang et al. Cell prestress. I. Stiffness and prestress are closely associated in adherent contractile cells *Am. J. Physiol. Cell Physiol.*, **282**, *3*, C606 - C616, 2002 .

[27] G.H. Altman et al. Cell differentiation by mechanical stress. *FASEB J.*, **16**, *2*, 270 - 272, 2002.

[28] N.D. Evans et al. Substrate stiffness affects early differentiation events in embryonic stem cells *Eur. Cell Mater*, **18**, 1 - 13, 2009.

[29] F. Chowdhury et al. Material properties of the cell dictate stress-induced spreading and differentiation in embryonic stem cells *Nature Materials*, **9**, 82 - 88, 2010.

[30] F. Zijl, G. Krupitza, W. Mikulits Initial steps of metastasis : Cell invasion and endothelial transmigration *Mutation Research*, **728**, 23 - 34, 2011.

[31] M.L. Gardel et al. Stress-Dependent Elasticity of Composite Actin Networks as a Model for Cell Behavior *Phys. Rev. Lett.*, **96**, 88 - 102, 2006.

[32] N. Mucke et al. Assessing the flexibility of intermediate filaments by atomic force microscopy *J. Mol. Biol.*, **335**, *5*, 1241 - 1250, 2004.

[33] C. Guzman et al. Exploring the mechanical properties of single vimentin intermediate filaments by atomic force microscopy *J. Mol. Biol.*, **360**, *3*, 623 - 630, 2006.

[34] S.J. Singer, G.L. Nicolson The fluid mosaic model of the structure of cell membranes *Science*, **175**, *4023*, 720 - 731, 1972.

[35] P.K. Matilla, P. Lappalainen Filopodia : molecular architecture and cellular functions *Nat. Rev. Mol. Cell Biol.*, **9**, *6*, 446 - 454, 2008.

[36] K.J. Painter et al. A nonlocal model for contact attraction and repulsion in heterogeneous cell populations *Bulletin of Math. Biol.*, **77**, 1132 - 1165, 2015.

[37] C.E. Morris Mechanosensitive ion channels *J. Membr. Biol.*, **113**, 93 - 107, 1990.

[38] P.D. Arora, C.A. McCulloch Dependence of collagen remodelling on alphasmooth muscle actin expression by fibroblasts *J. Cell Physiol.*, **159**, 161 - 175, 1994.

[39] S. Weinbaum, P. Guo, L. You A new view of mechanotransduction and strain amplification in cells with microvilli and cell processes *Biorheology*, **38**, 119 - 142, 2001.

[40] A. Yeung, E. Evans Cortical shellliquid core model for passive flow of liquid-like spherical cells into micropipets *Biophys. J.*, **56**, *1*, 139 -149, 1989.

[41] C.T. Lima, E.H. Zhoua, S.T. Quek Mechanical models for living cells - a review *J. of Biomech.*, **39**, 195 - 216, 2006.

[42] G.W. Schmid-Schonbein et al. Passive mechanical properties of human leukocytes *Biophys. J.*, **36**, *1*, 243 - 256, 1981.

[43] R. M. Hochmuth Micropipette Aspiration of Living Cells *J. Biomech.*, **33**, *1*, 15 - 22, 2000.

[44] T.K. Berdyyeva, C.D. Woodworth, and I. Sokolov Human epithelial cells increase their rigidity with ageing in vitro : direct measurements *Phys. Med. Biol.*, **50**, *81*, 81 - 92, 2005.

[45] I. Sokolov Atomic Force Microscopy in Cancer Cell Research *Cancer Nanotechnology*, 1 - 17, 2007.

[46] K.V. Christ, K.T. Turner Methods to Measure the Strength of Cell Adhesion to Substrates *Journal of Adhes. Sci. and Technol.*, **24**, 2027 - 2058, 2010.

[47] H. Lu et. al Microfluidic shear devices for quantitative analysis of cell adhesion *Anal. Chem.*, **76**, 5257 - 5264, 2004.

[48] D.B. Agus et al. A physical sciences network characterization of non-tumorigenic and metastatic cells *Sci. Rep.*, **3**, 1449, 2013.

[49] F. Chowdhury et al. Soft substrates promote homogeneous self-renewal of embryonic stem cells via downregulating cellmatrix tractions *PLoS One*, **5**, *12*, e15655, 2010.

[50] M.J. Dalby et al. The control of human mesenchymal cell differentiation using nanoscale symmetry and disorder *Nat. Mater.*, **6**, 997 - 1003, 2007.

[51] A.K. Harris, P. Wild and D. Stopak Silicone rubber substrata : a new wrinkle in the study of cell locomotion *Sci.*, **208**, *4440*, 177 - 179, 1980.

[52] M. Gupta et al. Micropillar substrates : A tool for studying cell mechanobiology *Meth. in Cell Biol.*, **125**, 289 - 308, 2015.

[53] M.L. Rodriguez, P.J. McGarry, N.J. Sniadecki Review on Cell Mechanics : Experimental and Modeling Approaches *Appl. Mech. Rev.*, **65**, *6*, 060801, 2013.

[54] S.-Y. Tee et al. Cell Shape and Substrate Rigidity Both Regulate Cell Stiffness *Bioph. J.*, **100**, 25 - 27, 2011.

[55] http ://mbi.nus.edu.sg/features/benoit-ladouxs-latest-findings-on-mechanosensing-and-cell-substrate-stiffness-in-pnas/ 20/04/2016.

[56] R.S. Fischer Stiffness-controlled three-dimensional extracellular matrices for high-resolution imaging of cell behavior *Nature Protocols*, **7**, 2056 - 2066, 2012.

[57] C.M., Wang et al. Cell movement is guided by the rigidity of the substrate *Biophys. J.*, **79**, 144 - 152, 2000.

[58] A. Marinkovic et al. Improved throughput traction microscopy reveals pivotal role for matrix stiffness in broblast contractility and TGF-β responsiveness *Am. J. Physiol. Lung Cell Mol. Physiol.*, **303**, L169 - L180, 2012.

[59] Y. Iwadate, S. Yumura Molecular dynamics and forces of a motile cell simultaneously visualized by TIRF and force microscopies *BioTechniques*, **44**, 739 - 750, 2008.

[60] S.V. Plotnikov High-Resolution Traction Force Microscopy, Methods in Cell Biology *Meth. in Cell Biol.*, **123**, 367 - 394, 2014.

[61] C. Franck et al. Three-dimensional Full-field Measurements of Large Deformations in Soft Materials Using Confocal Microscopy and Digital Volume Correlation *Exp. Mech.*, **47**, 427 - 438, 2007.

[62] M.S. Hall et al. Mapping Three-Dimensional Stress and Strain Fields within a Soft Hydrogel Using a Fluorescence Microscope *Biophys. J.*, **102**, 2241 - 2250, 2012.

[63] J.C. del Alamo et al. hree-Dimensional Quantification of Cellular Traction Forces and Mechanosensing of Thin Substrata by Fourier Traction Force Microscopy *PLOS ONE*, **8**, e69580, 2013.

[64] A. Engler et al. Substrate Compliance versus Ligand Density in Cell on Gel Responses *Biophys. J.*, **86**, 617 - 628, 2004.

[65] P. Ye et al. Compressive confocal microscopy : 3D reconstruction algorithms *Proc SPIE*, **7210**, 72100G, 2009.

[66] M.K. Cheezum, W.F. Walker, W.H. Guilford Quantitative comparison of algorithms for tracking single fluorescent particles *Biophys. J.*, **81**, *4*, 2378 - 2388, 2001.

[67] A.S. Piotrowski et al Three-Dimensional Traction Force Microscopy of Engineered Epithelial Tissues *Meth. and Prot., Meth. in Mol. Biol.*, **1189**, 191 - 206, 2015.

[68] W.R. Legant et al. Measurement of mechanical tractions exerted by cells in three-dimensional matrices *Nat. Meth.*, **7**, 969 - 973, 2010.

[69] Y.X. Gao, M.L. Kilfoil Accurate detection and complete tracking of large populations of features in three dimensions *Opt. Express*, **17**, 4685 - 4704, 2009.

[70] A. Lesman et al Contractile forces regulate cell division in three-dimensional environments *J. Cell Biol.*, **205**, *2*, 155 - 162, 2014.

[71] L.D. Landau, E.M. Lifshitz Theory of Elasticity *Pergamon Press*, **V.7**, 1970.

[72] A.N. Tikhonov, V.Y. Arsenin Solution of Ill-posed Problems *Washington : Winston and Sons*, 1977.

[73] P.C. Hansen The L-Curve and Its Use in the Numerical Treatment of Inverse Problems, Computational Inverse Problems in Electrocardiology *WIT Press*, 119 - 142, 2001.

[74] T. Reginska A regularization parameter in discrete ill-posed problems *SIAM J. Sci. Comput.*, **17**, 740 - 749, 1996.

[75] C. Barentin, Y. Sawada, J.-P. Rieu An iterative method to calculate forces exerted by single cells and multicellular assemblies from the detection of deformations of flexible substrates *Eur. Biophys. J.*, **35**, 328 - 339, 2006.

[76] R. Michel et al. Mathematical framework for traction force microscopy *ESAIM : PROCEEDINGS*, **7**, 1 - 10, 2013.

[77] J. Steinwachs et al. Three-dimensional force microscopy of cells in biopolymer networks *Nat. Meth.*, **13**, *2*, 171 - 176, 2016.

[78] B. Sabass et al. High Resolution Traction Force Microscopy Based on Experimental and Computational Advances *Biophys. J.*, **94**, 207 - 220, 2008.

[79] M. Dembo et al. Imaging the Traction Stresses Exerted by Locomoting Cells with the Elastic Substratum Method *Biophys. J.*, **70**, 2008 - 2022, 1996.

[80] J.P. Butler Traction fields, moments, and strain energy that cells exert on their surroundings *Am. J. Physiol. Cell Physiol.* , **282**, C595 - C605, 2002.

[81] U.S. Schwarz, J.R.D. Soine Traction force microscopy on soft elastic substrates : A guide to recent computational advances *Biochimica et Biophysica Acta*, **1853**, 3095 - 3104, 2015.

[82] R. Michel et al Inverse problems for the determination of traction forces by cells on a substrate : a comparison of two methods *Comput. Meth. Biomech. Biomed. Engin.*, **15**, *1*, 27 - 29, 2012.

[83] C. Gosse, V. Croquette Magnetic Tweezers : Micromanipulation and Force Measurement at the Molecular Level *Biophys. J.*, **82**, 3314 - 3329, 2002.

[84] T. Lionnet et al. Single-Molecule Studies Using Magnetic Traps *Cold Spring Harb. Protoc.*, **1**, 34 - 39, 2012.

[85] Z. Zhang, C.-H. Menq Three-dimensional particle tracking with subnanometer resolution using off-focus images *Appl. Opt.*, **47**, *13*, 2361 - 2370, 2008.

[86] S.-H. Lee et al. Characterizing and tracking single colloidal particles with video holographic microscopy *Opt. Express*, **15**, *26*, 18275 - 18282, 2007.

[87] J. Fung et al. Imaging Multiple Colloidal Particles by Fitting Electromagnetic Scattering Solutions to Digital Holograms *Journal of Quantitative Spectroscopy and Radiative Transfer*, **113**, 2482 - 2489, 2012.

[88] R.S. Fischer et al. Stiffness-controlled three-dimensional extracellular matrices for high-resolution imaging of cell behavior *Nat. Prot.*, **7**, 2056 - 2066, 2012.

[89] D.W. Allan Should the Classical Variance Be Used as a Basic Measure in Standards Metrology ? *IEEE Trans. on Instrumentation and Measurement*, **IM-36**, 646 - 654, 1987.

[90] J.P. Cnossen, D. Dulin, N.H. Dekker An optimized software framework for real-time, high-throughput tracking of spherical beads *Rev. Sci. Instrum.*, **85**, 103712, 2014.

[91] A. Mogilner, B. Rubinstein The Physics of Filopodial Protrusion *Biophys. J.*, **89**, *2*, 782 - 795, 2005.

[92] J.H.C. Wang, J.S. Lin Cell traction force and measurement methods *Biomech. Model Mechanobiol.*, **6**, 361 - 371, 2007.

[93] H. Tanimoto, M. Sano Simple Force-Motion Relation for Migrating Cells Revealed by Multipole Analysis of Traction Stress *Biophys. J.*, **106**, 16 - 25, 2014.

[94] R. Ananthakrishnan, A. Ehrlicher The Forces Behind Cell Movement *J. Biol. Sci.*, **3**, *5*, 303 - 317, 2007.

[95] U.S. Schwarz et al. Calculation of Forces at Focal Adhesions from Elastic Substrate Data : The Effect of Localized Force and the Need for Regularization *Biophys. J.*, **83**, *3*, 1380 - 1394, 2002.

[96] F. Czerwinski Quantifying Noise in Optical Tweezers by Allan Variance *Opt. Express*, **17**, *5*, 13255 - 13269, 2009.

[97] B.M. Lansdorp, O.A. Saleh Power spectrum and Allan variance methods for calibrating single-molecule video-tracking instruments *Rev. Sci. Instrum.*, **83**, 025115, 2012.

[98] E. Cavatore Microscopie optique appliquée à la micro-manipulation par pinces magnétiques à haute résolution et à la visualisation de nano-objets métalliques individuels (Ph.D. thesis) *Université Pierre et Marie Currie*, 2011.

[99] T.D. Visser, J.L. Oud, G.J. Brakenhoff Refractive index and axial distance mesurements in 3-D microscopy *Optik*, **90**, *1*, 17 - 19, 1992.

[100] S. Hell et al. Abberations in confocal microscopy induced by mismatches in refractive index *Journal of Microscopy*, **169**, 391 - 405, 1993.

[101] G. Sava et al. Dual Action of NAMI-A in Inhibition of Solid Tumor Metastasis : Selective Targeting of Metastatic Cells and Binding to Collagen *Clinical Cancer Research*, **9**, 1898 - 1905, 2003.

[102] A.D. Richardsa, A. Rodger Synthetic metallomolecules as agents for the control of DNA structure *Chem. Soc. Rev.*, **36**, 471 - 483, 2007.

[103] S. Leijen et al. Phase I/II study with ruthenium compound NAMI-A and gemcitabine in patients with non-small cell lung cancer after first line therapy *Invest New Drugs*, **33**, 201 - 214, 2015.

[104] C.S. Allardyce, P.J. Dyson Ruthenium in medicine : current clinical uses and future prospects *Platin. Met. Rev.*, **45**, 62 - 69, 2001.

[105] S. Page Ruthenium compounds as anticancer agents *Education in Chemistry*, 2012.

[106] M. Cocchietto et al. Primary tumor, lung and kidney retention and antimetastasis effect of NAMI-A following different routes of administration *Investigational New Drugs*, **21**, 55 - 62, 2003.

[107] S. Munevar, Y. Wang, M. Dembo Traction Force Microscopy of Migrating Normal and H-ras Transformed 3T3 Fibroblasts *Biophys. J.*, **80**, 1744 - 1757, 2001.

[108] L. Brescacin et al. Effects of the ruthenium-based drug NAMI-A on the roles played by TGF-1 in the metastatic process *J. Biol. Inorg. Chem.*, **20**, 1163, 2015.

[109] A. Huhle et al. Camera-based three-dimensional real-time particle tracking at kHz rates and Angstrom accuracy *Nat. Comm.*, **5585**, 2015.

Stanislaw MAKARCHUK

Résumé

Mots clés: forces cellulaires, microscopie holographique, microscopie de force de traction, champ de déplacement, champ de force, lignée cellulaire d'adénocarcinome SW 480

Les forces mécaniques, générées par la cellule jouent un rôle crucial dans l'adhésion cellulaire, qui est un processus commun à un grand nombre de lignées cellulaires. Afin de mesurer la champ des forces pendant l'adhérence cellulaire, nous utilisons la microscopie de force de traction, où la cellule adhère à la surface plane d'un substrat souple dans le plan. Les forces sont calculées à partir du champ de déplacement mesuré à l'intérieur du substrat sous la cellule. Nous avons construit le microscope, dans lequel nous utilisons des billes sphériques en polystyrène pour mesurer le champ de déplacement. Les positions des marqueurs sont obtenues en analysant l' image interférentielle des particules. Avec cette technique, nous atteignons une précision nanométrique sur le champ de déplacement des particules, ce quinous permet d'améliorer la résolution en force de ce type de microscope. Les premières mesures ont été effectuées avec la lignée de cellules cancéreuses SW 480.

Résumé en anglais

Keywords : cellular forces, holographic microscopy, traction force microscopy, displacement field, force field, adenocarcinoma cell line SW 480

Mechanical forces, generated by the cell plays crucial role in cell adhesion – common process for different cell lines. In order to measure the force map during cellular adhesion, we use Traction Force Microscopy (TFM), where cell adheres to the soft substrate in 2D plane, and the forces are calculated from measured displacement field inside the substrate underneath the cell. We built the microscope, where instead of using fluorescent markers, we use spherical polystyrene beads in order to measure the displacement field. Positions of the markers are obtained by analyzing the interference pattern caused by the beads in bright-field light. With this technique, we reach nanometer accuracy of the microsphere position determination, that, respectively, influence accuracy of the calculated force field. With the microscope first measurements were performed with cancer cell line SW 480.